A NUMERICAL INVESTIGATION OF
A TWO-LAYER FRONTAL GEOSTROPHIC MODEL OF THE
ANTARCTIC CIRCUMPOLAR CURRENT

by

Ryan Lukeman

SUBMITTED IN PARTIAL FULFILLMENT OF THE
REQUIREMENTS FOR THE DEGREE OF
MASTER OF SCIENCE

AT

DALHOUSIE UNIVERSITY
HALIFAX, NOVA SCOTIA
AUGUST 24, 2005

DALHOUSIE UNIVERSITY

DEPARTMENT OF MATHEMATICS AND STATISTICS

The undersigned hereby certify that they have read and recommend to the Faculty of Graduate Studies for acceptance a thesis entitled " **A Numerical Investigation of a Two-Layer Frontal Geostrophic Model of the Antarctic Circumpolar Current**" by **Ryan Lukeman** in partial fulfillment of the requirements for the degree of **Master of Science**.

Dated: August 24, 2005

Supervisors:

—————————————————————
Dr. Ray Spiteri

—————————————————————
Dr. Richard Karsten

Reader:

—————————————————————
Dr. Keith Thompson

DALHOUSIE UNIVERSITY

Date: **August 24, 2005**

Author: **Ryan Lukeman**

Title: **A Numerical Investigation of a Two-Layer Frontal Geostrophic Model of the Antarctic Circumpolar Current**

Department: **Mathematics and Statistics**

Degree: **M.Sc.** Convocation: **October** Year: **2005**

To my mother,

for investing her brilliance in her children,

in the hopes that some of it would rub off.

Table of Contents

List of Tables

List of Figures

Abstract

The numerical simulation of oceanic flow is a primary research tool for understanding the physical properties of the world ocean. These models range from complex, high-resolution models to simplified models in idealized domains. In the spirit of the latter, a two-layer frontal geostrophic model is discussed for a wind-driven circumpolar flow via an asymptotic reduction of the shallow-water equations. The model is implemented using the finite element method via the software package FEMLAB. The model is used to study the meridional balance, lower-layer outcropping, and parameter variation in the Antarctic Circumpolar Current, the dominant oceanic flow in the Southern Ocean. The effects of varying resolution and timestepping parameters is discussed. Experiments are performed in a number of domain and bottom topography regimes to examine the effects of the Drake Passage and a topographic ridge on the meridional balance and transport that prevails in the current. The results support a mechanism of balance by which momentum imparted by winds at the surface is transferred to the lower layer via eddies and dissipated by the ocean bottom.

Acknowledgements

I wish to thank my co-supervisors, Richard Karsten and Ray Spiteri, for their generous gift of their time and effort. Both brought their own expertise to this project to enable its completion, and offered invaluable guidance and suggestions. Also, I wish to thank Dr. Keith Thompson for offering his time and patience in serving as a reader for this thesis. I also would like to thank the professors and staff of the Department of Mathematics and Statistics at Dalhousie for their excellent teaching and assistance throughout my time here.

I wish to thank my parents for their constant support and generosity throughout my education, and my brothers for their humor, inspiration and influence. Finally, I would like to thank my wife, Sionnach, for her encouragement, love, and companionship that guides me through my studies, and my life.

Chapter 1

Introduction

The numerical simulation of oceanic flow is a primary research tool for understanding the physical properties of the world ocean. These simulations take place on many levels of complexity, ranging from high-resolution models of the entire world ocean, to simplified models of particular flows. Although the former provide the most realistic representation of oceanic flow, the computational requirements for these models are typically very large. Often, the information sought via a mathematical model need not contain high detail or complexity, and so simpler models are used. These simpler models are naturally much less computationally intensive. This allows detailed exploration of parameter spaces as well as long-time simulations, both of which are typically not feasible in complex ocean models. This thesis concerns a two-layer frontal geostrophic model, an example of a simpler model.

The construction of this simplified model involves a number of mathematical considerations. At the basis of the model physics is the shallow-water equations for fluid flow, a set of partial differential equations (PDEs) that are derived from basic physics principles. Asymptotic analysis is used to isolate the leading-order effects in these equations such that higher-order terms can be legitimately discarded. Numerical solution of the resultant PDEs strives for stability, efficiency, and flexibility, while imposing boundary conditions and initial conditions to create a well-posed problem. Finally, resultant data from the simulations must be analyzed and validated.

To address these mathematical concerns, this thesis maintains two threads throughout. On one hand, this thesis is concerned with the mathematics of the model derivation and its numerical simulation. On the other, this thesis attempts to place the model in a physical oceanographic context, especially in the motivating physics and the analysis of the simulation results.

In this thesis, a two-layer frontal geostrophic (FG) model for wind-driven fluid flow

is simulated with the finite element method, using the software package FEMLAB. The model is used to study the Antarctic Circumpolar Current (ACC), the dominant flow in the Southern Ocean. As we show in Chapter 2, the model used in this thesis is well-suited to the ACC. A detailed description of the contents of the thesis follows.

Chapter 2 contains a description of the two-layer frontal geostrophic model. Section 2.1 describes the motivating physics for the model in the context of the Antarctic Circumpolar Current. Section 2.2 contains a detailed derivation of the shallow-water equations from basic physical principles followed by the reduction of the shallow-water equations to the frontal geostrophic model equations. Sections 2.3 and 2.4 complete the model description by discussing the domain, boundary conditions, and initial conditions. These sections also give some sense of the temporal domain that is required for our analysis.

Chapter 3 outlines the steps taken to simulate the two-layer FG model in the finite element software package FEMLAB. Section 3.1 contains a short introduction to the software and the motivation for this choice of implementation. Section 3.2 describes the adaptation of our model equations into a form that is acceptable to FEMLAB. This process turns out to require considerable manipulation. Section 3.3 is a discussion of the model parameters used in our simulations, most of which are derived from [33], the work we use as a guide for our experimentation with the model. Sections 3.4 and 3.5 specify the implementation of domain and initial conditions discussed in Sections 2.3 and 2.4 in the context of FEMLAB. This section includes the introduction of bottom topography, and details its incorporation into the model.

Chapter 4 details the results from running a number of experiments with our finite element model implementation. Central to our experimentation is the varying Ekman pumping strength. This chapter is primarily oceanographic in nature. Section 4.1, 4.2, and 4.3 introduce the concepts that are needed to understand the simulation results. Section 4.4 describes the results of experiments in a simple channel corresponding to a rectangular domain. These results are conveyed primarily through time-average plots. Section 4.5 describes the results of experiments in a modified channel that mimics the Drake Passage in an idealized sense. Section 4.6 combines

the data from the experiments of Sections 4.4 and 4.5 into a discussion of the transport and the effects of wind strength, topography, and land barriers on the established transport. Section 4.7 contains a short analysis of the effects of varying resolution, and provides justification for the resolution used for the experiments performed in this work. Section 4.8 contains a description of the time-stepping scheme used and some results on the efficiency of our finite element implementation as compared to a number of other models for oceanic flow on a similar scale.

Chapter 5 contains some concluding remarks and possible future work.

Chapter 2

The Two-Layer Frontal Geostrophic Model

2.1 Introduction

The Antarctic Circumpolar Current is the major oceanic current of the southern hemisphere. It travels around Antarctica (see Figure 2.1), and acts as a conduit for the transport of quantities such as heat, salt, and carbon dioxide between the major ocean basins, thus having a significant impact on the Earth's climate. This strong and deep-reaching *zonal* (i.e., east-west or latitudinal) current also acts as a barrier to transport across the current, leaving the ocean to the south of the ACC relatively isolated from heat and substance sources from the rest of the world ocean [25]. The flow of the ACC is predominantly influenced by strong westerly winds that circle the southern hemisphere. These winds attain a maximum strength in the latitudinal region of $52^{\circ} - 57^{\circ}$ south (see Figure 2.2), precisely the latitudes in which the ACC flows around the earth, providing evidence of the importance of these winds on the flow. These winds impart an eastward momentum into the ACC.

The flow variability of the ACC has been imaged by sea surface height measurements via satellite. The data attest to the existence of *eddies* throughout the region of flow (see Figure 2.3). The turbulent, meandering flow characterized by eddies is hypothesized to play an important role in thermodynamical transport and balance in the southern hemisphere.

In any region of flow in the ocean, momentum forcing is primarily applied in two ways: by winds interacting at the surface of the ocean and by frictional forces occurring between flowing water and the ocean bottom (or land boundaries). Any boundary region that transmits these forces is known as an *Ekman layer*. Accordingly, there exists an Ekman layer both at the surface and bottom of the ocean. There is a third 'force', the *Coriolis force*, which is the effect of the spinning of the earth upon moving objects. The Coriolis force is actually a fictitious force; its effect is the

5
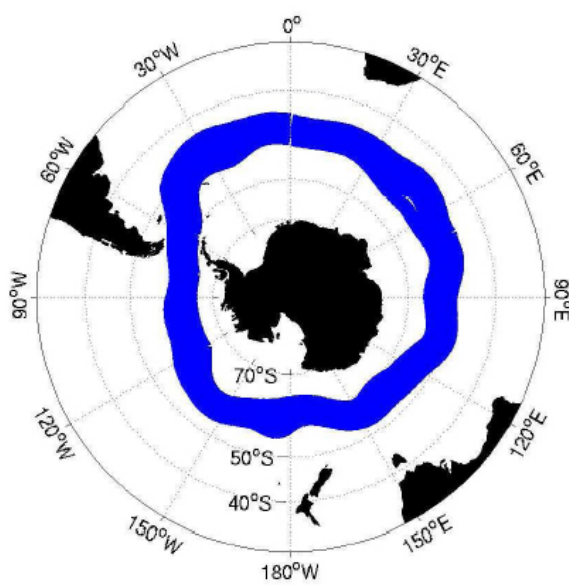
Figure 2.1: The path of flow of the Antarctic Circumpolar Current, as estimated by satellite altimetry data (adapted from [12]).
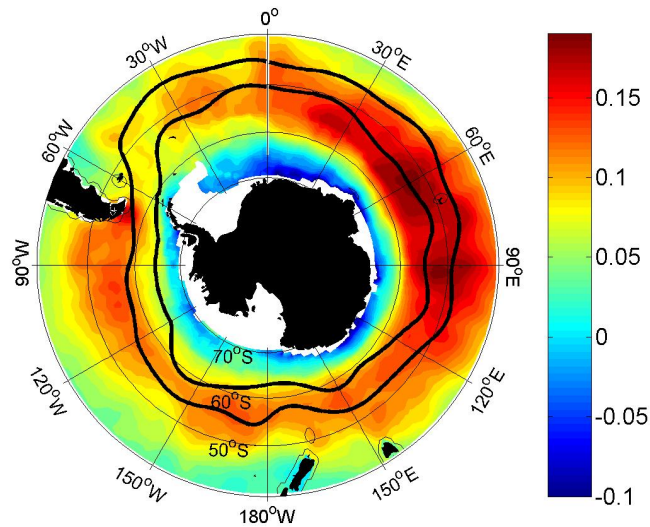
Figure 2.2: The zonal wind stress in the Southern Ocean, in Nm^{-2}, attaining a maximum in the region of flow of the ACC, from the Southampton Oceanographic Centre (SOC) data set.

result of measuring velocities in a rotating frame of reference and not due to any real physical consideration. In the northern hemisphere, the Coriolis force appears to deflect moving objects to the right, and in the southern hemisphere, to the left [17]. There are also buoyancy forces resulting from salinity and temperature fluxes, though these are not considered in this thesis.

At the immediate ocean surface, the impact of the wind force on the water imparts momentum on the surface water, which, due to the Coriolis deflection, is oriented to the left of the wind force. As the imparted momentum is successively transferred to the underlying layers of water, the frictional resistance decreases the velocity of the water, increasing the deflection by the Coriolis force. The result of this process is a spiraling flow with diminishing velocity with depth, called an *Ekman spiral* [24]. The Ekman spiral has a net flow in the Ekman layer, oriented perpendicular to the wind force and in the direction of the Coriolis deflection (see Figure 2.4 for an idealized model of this process).

The westerlies which prevail over the ACC decline in strength latitudinally as one moves away from the region of flow. Thus, south of the ACC, the positive wind-force curl creates an area of divergence, and thus, upwelling (Figure 2.5). Similarly, north
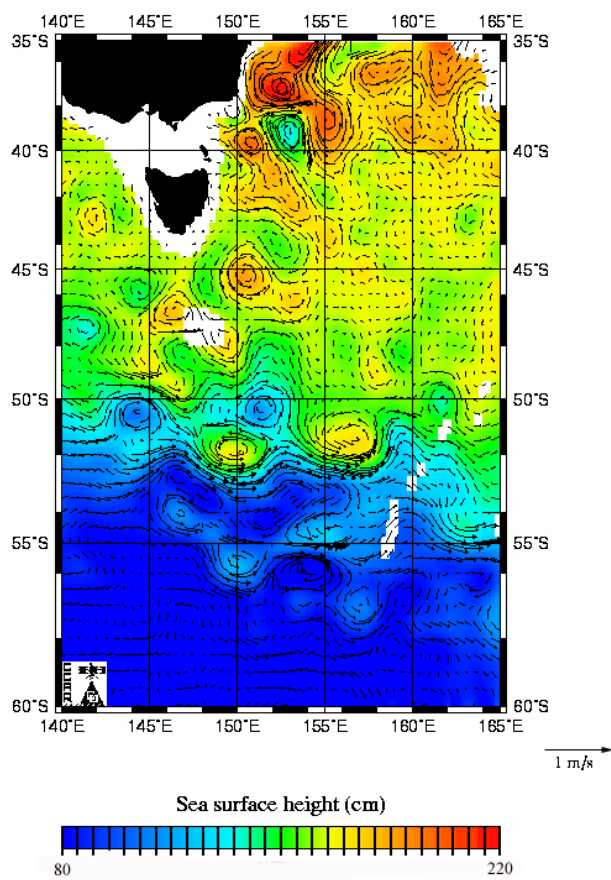
Figure 2.3: Sea surface altimetry data below Australia showing the eddy-dominated flow of the ACC, from the TOPEX/ERS2 data set.
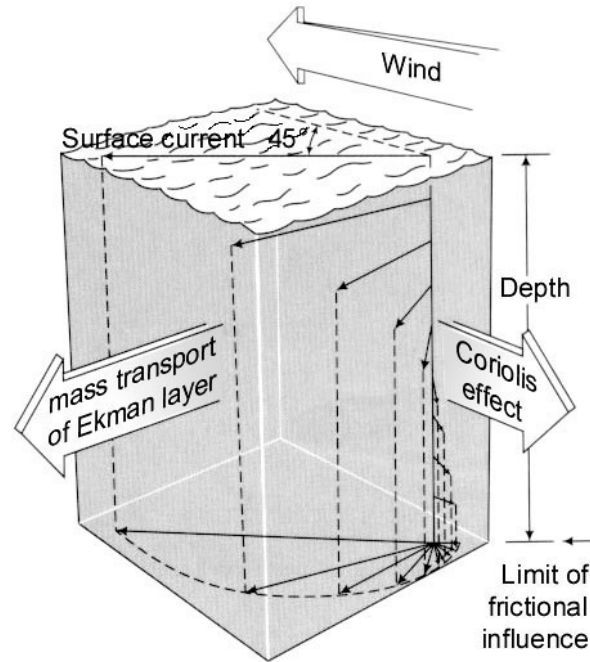
Figure 2.4: The Ekman spiral: In the southern hemisphere, wind forcing results in a net flow perpendicular and to the left of the wind direction (adapted from [22]).

of the ACC, there is a negative wind-force curl, which creates an area of convergence, and thus downwelling (Figure 2.5). The northward Ekman transport at the surface along with the downwelling and upwelling create an overturning circulation known as the *Deacon Cell* (see Figure 2.6). The Deacon cell tilts the *isopycnals* (lines of constant density), creating a density gradient in the fluid known as a front. The sloped isopycnals impart momentum into the fluid, though directed perpendicular and to the left of the positive density gradient due to the Coriolis force [19]. Thus, there is a relatively strong net eastward forcing resulting from the Deacon cell which drives the eastward flow of the ACC. The flow of the ACC is basically *geostrophic*, meaning that the zonal current velocity is determined by the *meridional* (i.e., north-south or longitudinal) balance that occurs between the hydrostatic pressure gradient associated with the sloped isopycnals, and the Coriolis force. Thus, the density profile of the water column in the region of the ACC plays the dominant role in driving the eastward current [25].

In layer models, the density profile is represented by discrete layers of fluid, with a
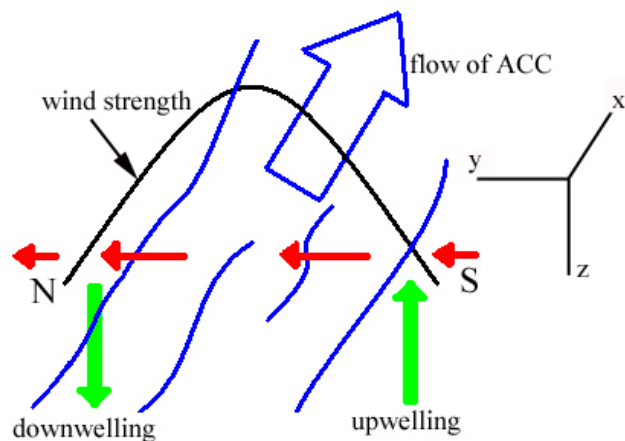
Figure 2.5: The wind forcing (black) attains a maximum in the central latitudes of the ACC. At the south of the ACC, the positive wind stress creates a net outflux in Ekman transport (i.e., divergence) (shown in red), drawing up water from below (i.e., upwelling) (shown in green). In the north, the negative wind stress creates a net influx of Ekman transport (i.e., convergence), which pushes water downward (i.e., downwelling).
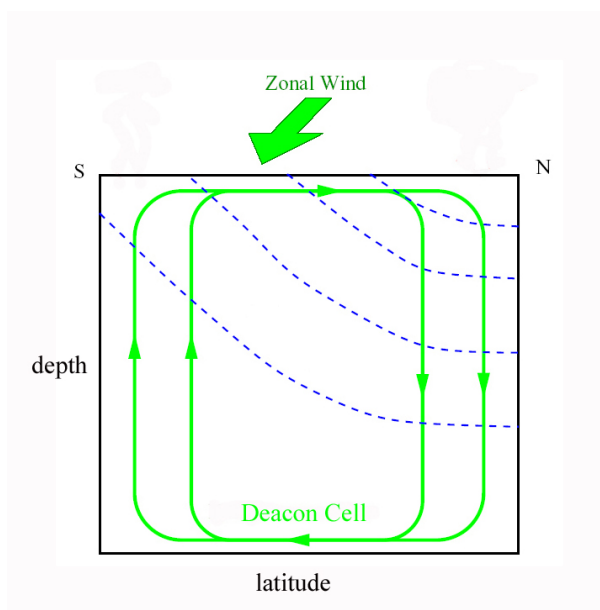
Figure 2.6: The Deacon Cell: the dotted lines represent isopycnals, which are sloped by the overturning circulation (adapted from [13]).
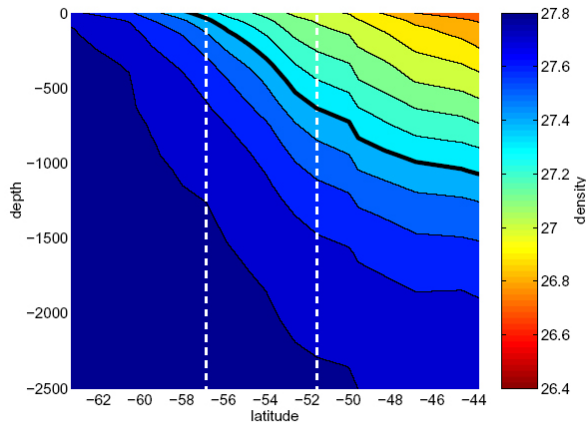
Figure 2.7: The zonally averaged density profile of the southern ocean over depth in m, and latitude, from hydrographic data. Density units are given by kg/m^3 above 1000 kg/m^3, the density of pure water. The sloped isopycnals resulting from the Deacon cell are apparent. The dotted lines represent the approximate region of flow of the ACC (adapted from [12]). The thick black line separates the density profile into two layers.

constant density in each layer. The dynamics of the flow can then be understood from the behavior of the density layer interfaces, which determine the pressure gradient. In the two-layer frontal geostrophic (FG) model, we treat the density gradient as two separate layers of constant density, with the resulting interface governing the flow of the current (see Figures 2.7 and 2.8). A density value is chosen to separate the density profile into two discrete layers.

The westerly winds which prevail over our region of flow constantly impart momentum into the water. In order to achieve a steady state of flow, there must be a balancing force to counteract the constant forcing of the wind. When treating the ocean as two layers, we seek a balance in forcing in each layer. In the lower layer, momentum is dissipated via *bottom formstress*, which transfers momentum out of the water and into the solid earth by flow interaction with bottom topography [25]. However, no such bottom formstress exists in the upper layer; here there must be another mechanism of momentum dissipation, or else the zonal flow would accelerate indefinitely with the continuous imparting of momentum via the wind forcing. It turns out that there is a vertical transfer of momentum from the upper layer to the
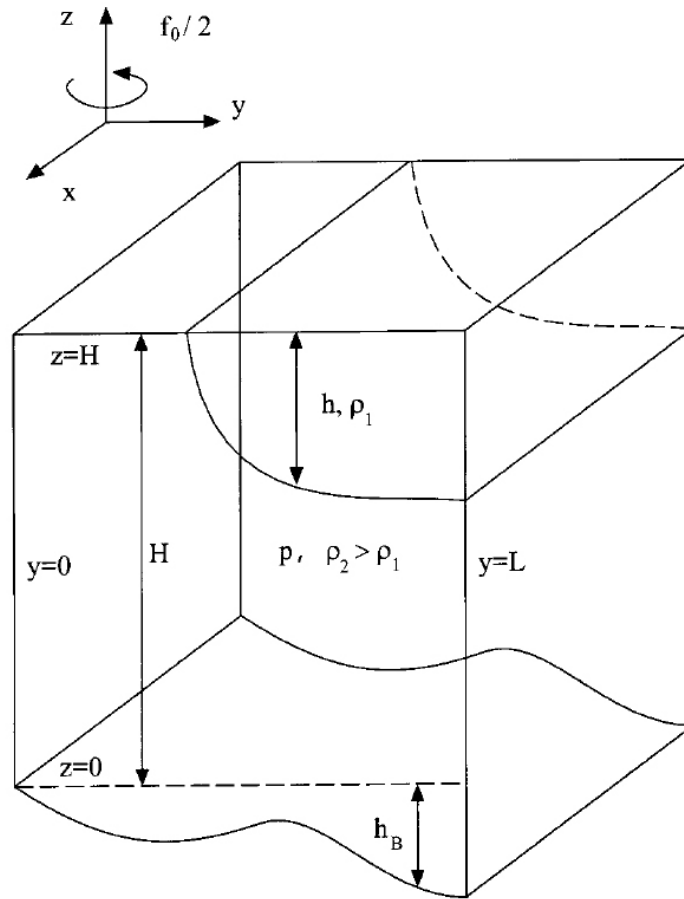
Figure 2.8: The two-layer FG model geometry. ρ_1 is the upper layer density, ρ_2 is the lower layer density, h is the upper layer depth, and p is the lower layer pressure (adapted from [18]).

lower layer via eddy *interfacial formstress*, caused by eddy-induced fluctuations in the zonal pressure gradient (see [25] for details). This transfer of momentum to the lower layer is then dissipated by bottom formstress, thus allowing a momentum balance in both layers.

In the presence of land masses, a frictional boundary layer around the land mass can also play an important role in balancing the wind forcing. This effect is most prominent at the Drake Passage, where the meridional spread of the ACC is constrained by the Antarctic Peninsula, and South America. The important effects of land masses motivate the inclusion of land barriers in the modelling domain.

The two-layer frontal geostrophic model is so named for three reasons. First, it

uses two layers to model the density profile. Second, the flow is *geostrophic*; that is, at leading order, flow is balanced by the pressure gradient and Coriolis force [17]. Finally we model the 'front' of tilted isopycnals to determine the flow pattern. The model we use to simulate the flow dynamics of the ACC was first developed by Cushman-Roisin et al. [6], and independently for flow over a sloping bottom by Swaters [31]. Karsten and Swaters [14] established conditions on the nonlinear stability of the model, and extended the applicability of the model to a much larger range of flow geometries. In two companion papers, Karsten and Swaters provided a comprehensive description of the nonlinear dynamics of the model from a strong-β [15] and weak-β [16] standpoint. Reszka and Swaters [28] applied the model to buoyancy-driven coastal currents, and found an agreement between the reduced FG model results and primitive-equation models. Reszka and Swaters [29] used the model in a study of the Gaspé Current, finding an agreement between observed data and model results, and also noting the destabilizing effect of bottom topography, and its importance in the consideration of such coastal flows. The model used in this thesis lacks both the refinement and complexity of other models (e.g., General Circulation Models (see, e.g., [36])) that similarly model the flow pattern in the ACC. However, the computational requirement for the solution of these other models is quite large. This requirement impedes experimentation with model variables and parameters. In this thesis, we seek to create a reasonable numerical model which gives solutions on a more manageable time scale, allowing oceanographers to more easily experiment with the model inputs to see the effects on the generated flow patterns. The two-layer FG model we use is essentially a simplification of the *shallow-water equations* [19]. The simplification is achieved mainly through making leading-order approximations for variables and ignoring higher-order terms. Thus, the two-layer FG model is unable to resolve high-order phenomena, such as internal gravity waves. However, these phenomena are only important in models of either very high resolution or very small domains, both of which do not immediately concern us.

The two layers of the FG model do not include the Ekman layer at the surface of the ocean. In the Ekman layer, there is a northward transport of water, but we are concerned only with the effect of this transport on the underlying water (i.e.,

the upper layer of the model). The primary effect is the downwelling and upwelling processes of the Deacon Cell that are represented by Ekman pumping terms in the model. However, a number of other processes occur which are not resolved in the model. Specifically, the northward transport in the Ekman layer implies coastal downwelling along the north boundary of the domain, and upwelling at the southern boundary, both of which are not included in the model. Also, by representing the wind forcing as a stress (i.e., the curl of the wind forcing), the model is unable to properly model a spatially uniform wind.

2.2   Governing Equations

Because we are modelling a region for which the length scale is much larger than the depth scale, we are justified in using a shallow-water approximation for our model. We now derive the shallow-water equations for two layers following [19]; we subsequently derive our model equations from this basis.

To derive the two-layer shallow-water equations, we begin with the conservation of momentum equation,

$$\frac{D\mathbf{u}}{Dt} + 2\mathbf{\Omega} \times \mathbf{u} = -\frac{1}{\bar{\rho}}\nabla p - \hat{\mathbf{g}} - R\mathbf{u} + \hat{\nu}\nabla^2\mathbf{u}, \tag{2.1}$$

and the continuity equation for an incompressible fluid,

$$\nabla \cdot \mathbf{u} = 0, \tag{2.2}$$

where $\mathbf{u} = (u, v, w)$ is the velocity of the fluid, with u directed eastward, v northward, and w upward, p is the fluid pressure, $\bar{\rho}$ is the constant average fluid density, $\hat{\mathbf{g}} = (0,\ 0,\ g)$ is the force of gravity on the fluid, applied in the vertical direction,

$$\hat{\nu} = \begin{bmatrix} \nu & 0 & 0 \\ 0 & \nu & 0 \\ 0 & 0 & 0 \end{bmatrix},$$

where ν is the coefficient of horizontal turbulent viscosity representing unresolved scales, and $\mathbf{\Omega} = (\Omega_x, \Omega_y, \Omega_z)$ is the angular velocity vector of the earth [19]. The term

$-R\mathbf{u}$ represents the effect of the Ekman layer at the ocean bottom, where

$$
R = \begin{bmatrix} r & 0 & 0 \\ 0 & r & 0 \\ 0 & 0 & 0 \end{bmatrix},
$$

where r is the coefficient of Ekman friction.

The $\frac{D\mathbf{u}}{Dt}$ term in (2.1) is the material derivative of $\mathbf{u}$, defined as

$$
\frac{D\mathbf{u}}{Dt} := \frac{\partial \mathbf{u}}{\partial t} + \mathbf{u} \cdot \nabla \mathbf{u}.
$$

This term is the *Lagrangian acceleration* of the fluid, representing the sum of the local acceleration (the flow changing with respect to time) and advective acceleration (the flow changing with respect to space). It is thus the total acceleration experienced by a parcel of fluid [17].

Large-scale geophysical flow problems are often most conveniently solved in spherical co-ordinates. However, when width scales (north-south) are relatively small in comparison to the radius of the earth, we can ignore the curvature of the earth, and instead adopt a local Cartesian system on a tangent plane [19]. For the ACC, a typical width scale is 2000 km, while the mean radius of the Earth is 6371 km, giving a ratio of approximately 0.30. This value is sufficiently small to allow the adoption a Cartesian system, although our scalings lie in the limits of applicability for this simplification [12]. If we were to extend the longitudinal scale of our model, the adoption of a spherical co-ordinate system would likely be necessary.

Using the local Cartesian system, we rewrite the components of the angular velocity, $\boldsymbol{\Omega}$, as

$$
\begin{aligned}
\Omega_x &= 0, \\
\Omega_y &= |\boldsymbol{\Omega}| \cos \theta, \\
\Omega_z &= |\boldsymbol{\Omega}| \sin \theta,
\end{aligned}
$$

where θ is the latitude. The Coriolis force is thus

$$
\begin{aligned}
2\boldsymbol{\Omega} \times \mathbf{u} &= \begin{vmatrix} \hat{\mathbf{i}} & \hat{\mathbf{j}} & \hat{\mathbf{k}} \\ 0 & 2|\boldsymbol{\Omega}| \cos \theta & 2|\boldsymbol{\Omega}| \sin \theta \\ u & v & w \end{vmatrix} \\
&= 2|\boldsymbol{\Omega}|[\hat{\mathbf{i}}(w \cos \theta - v \sin \theta) + \hat{\mathbf{j}} u \sin \theta - \hat{\mathbf{k}} u \cos \theta], \quad\quad (2.3)
\end{aligned}
$$

where $\hat{\mathbf{i}}, \hat{\mathbf{j}}$, and $\hat{\mathbf{k}}$ are the elementary unit vectors. Because we are making a shallow-water approximation, $w \ll v$, and so we can assume that the $w \cos \theta$ term in (2.3) is negligible [19]. Then we can write the three components of the Coriolis force as

$$
\begin{aligned}
(2\boldsymbol{\Omega} \times \mathbf{u})_x &= -(2|\boldsymbol{\Omega}| \sin \theta)v = -fv, \\
(2\boldsymbol{\Omega} \times \mathbf{u})_y &= (2|\boldsymbol{\Omega}| \sin \theta)u = fu, \\
(2\boldsymbol{\Omega} \times \mathbf{u})_z &= -(2|\boldsymbol{\Omega}| \cos \theta)u,
\end{aligned}
$$

where we have defined

$$
f = 2|\boldsymbol{\Omega}| \sin \theta,
$$

known as the *Coriolis parameter*. The vertical component of the Coriolis force is generally negligible, dominated by the other terms in the vertical equation of motion [19]. This allows us to reduce the Coriolis force to

$$
2\boldsymbol{\Omega} \times \mathbf{u} \approx f \begin{pmatrix} -v \\ u \\ 0 \end{pmatrix}.
$$

Although the Coriolis parameter, f, varies with latitude, this variance is only important for phenomena with very long length scales [19]. Otherwise, we can approximate f by a constant value,

$$
f_0 = 2|\boldsymbol{\Omega}| \sin \theta_0, \tag{2.4}
$$

where θ_0 is the central latitude of flow. This approximation is known as an *f-plane approximation* [19]. One can achieve a better approximation by expanding f in a Taylor series about θ_0,

$$
f = f_0 + \beta y, \tag{2.5}
$$

where

$$
\beta = \left. \frac{df}{dy} \right|_{\theta_0} = \left. \left(\frac{df}{d\theta} \frac{d\theta}{dy} \right) \right|_{\theta_0} = \frac{2|\boldsymbol{\Omega}| \cos \theta_0}{R}, \tag{2.6}
$$

where R is the radius of the earth, and we have used $dy = R\, d\theta$. The approximation (2.5) is known as a *β-plane approximation* [19]. Approximating the Coriolis force by

the β-plane approximation is valid for the ACC [15], and thus we let

$$2\mathbf{\Omega} \times \mathbf{u} \approx (f_0 + \beta y) \begin{pmatrix} -v \\ u \\ 0 \end{pmatrix}. \tag{2.7}$$

Our model is based upon two layers of fluid with a constant density value within each layer. However, for flows with sufficiently small velocity and depth scales, density changes in a fluid can be neglected in the horizontal components of the momentum equation (2.1). This approximation, known as the *Boussinesq approximation* [19], is used in our model [12]. We thus use $\bar{\rho}$ for our constant reference density in the horizontal components of (2.1). We note that in the vertical direction, the density difference is significant, and so we allow density to vary in the vertical component of (2.1). This is accomplished by letting ρ_1 and ρ_2 be the upper and lower layer constant densities, thereby discretizing the density profile.

Because we represent our ocean domain by two layers of fluid, equation (2.1) holds in each layer. We rewrite equation (2.1) for each layer in component form, using the subscripting convention that 1 refers to variables in the upper layer, while 2 refers to variables in the lower layer:

$$\frac{Du_1}{Dt} + (f_0 + \beta y)(-v_1) = -\frac{1}{\bar{\rho}}\frac{\partial p_1}{\partial x} - r_1 u_1 + \nu_1 \frac{\partial^2 u_1}{\partial x^2}, \tag{2.8}$$

$$\frac{Dv_1}{Dt} + (f_0 + \beta y)u_1 = -\frac{1}{\bar{\rho}}\frac{\partial p_1}{\partial y} - r_1 v_1 + \nu_1 \frac{\partial^2 v_1}{\partial y^2}, \tag{2.9}$$

$$\frac{Dw_1}{Dt} = -\frac{1}{\rho_1}\frac{\partial p_1}{\partial z} - g, \tag{2.10}$$

$$\frac{Du_2}{Dt} + (f_0 + \beta y)(-v_2) = -\frac{1}{\bar{\rho}}\frac{\partial p_2}{\partial x} - r_2 u_2 + \nu_2 \frac{\partial^2 u_2}{\partial x^2}, \tag{2.11}$$

$$\frac{Dv_2}{Dt} + (f_0 + \beta y)u_2 = -\frac{1}{\bar{\rho}}\frac{\partial p_2}{\partial y} - r_2 v_2 + \nu_2 \frac{\partial^2 v_2}{\partial y^2}, \tag{2.12}$$

$$\frac{Dw_2}{Dt} = -\frac{1}{\rho_1}\frac{\partial p_2}{\partial z} - g. \tag{2.13}$$

Furthermore, the continuity equation (2.2) holds in each layer, and with the same subscripting convention as above, we write

$$\nabla \cdot \mathbf{u}_1 = 0, \tag{2.14}$$

$$\nabla \cdot \mathbf{u}_2 = 0. \tag{2.15}$$

Because there is no bottom friction in the upper layer, we set $r_1 = 0$.

The ocean can be viewed as a very thin fluid sheet, in which the depth scale is much less than the horizontal scale. Fluid trajectories are very shallow, and vertical velocities are generally much smaller than horizontal velocities [19]. We can therefore assume that vertical acceleration in each layer, $\frac{Dw_1}{Dt}$ and $\frac{Dw_2}{Dt}$, is negligible compared with gravitational/buoyancy forces; this is known as a *hydrostatic state*. Then (2.10) and (2.13) reduce to

$$\frac{\partial p_1}{\partial z} = -g\rho_1, \tag{2.16}$$

$$\frac{\partial p_2}{\partial z} = -g\rho_2. \tag{2.17}$$

Equations (2.16) and (2.17) are the *hydrostatic equations* in each layer. Integrating (2.16) and (2.17), we write

$$p_1 = -g\rho_1 z + \bar{\rho}\, \tilde{p}_1(x, y, t), \tag{2.18}$$

$$p_2 = -g\rho_2 z + \bar{\rho}\, \tilde{p}_2(x, y, t), \tag{2.19}$$

where $\tilde{p}_1$ and $\tilde{p}_2$ denote the normalized time-dependent pressure in each layer (in units of pressure per unit density) called the *dynamic pressure*. Replacing p_1 and p_2 in (2.8)–(2.13),

$$\frac{Du_1}{Dt} + (f_0 + \beta y)(-v) = -\frac{1}{\bar{\rho}} \frac{\partial(-g\rho_1 z + \bar{\rho}\, \tilde{p}_1(x, y, t))}{\partial x} + \nu_1 \frac{\partial^2 u_1}{\partial x^2}, \tag{2.20}$$

$$\frac{Dv_1}{Dt} + (f_0 + \beta y)u = -\frac{1}{\bar{\rho}} \frac{\partial(-g\rho_1 z + \bar{\rho}\, \tilde{p}_1(x, y, t))}{\partial y} + \nu_1 \frac{\partial^2 v_1}{\partial y^2}, \tag{2.21}$$

$$\frac{Du_2}{Dt} + (f_0 + \beta y)(-v) = -\frac{1}{\bar{\rho}} \frac{\partial(-g\rho_2 z + \bar{\rho}\, \tilde{p}_2(x, y, t))}{\partial x} - r_2 u_2 + \nu_2 \frac{\partial^2 u_2}{\partial x^2}, \tag{2.22}$$

$$\frac{Dv_2}{Dt} + (f_0 + \beta y)u = -\frac{1}{\bar{\rho}}\frac{\partial(-g\rho_2 z + \bar{\rho}\,\tilde{p}_2(x,y,t))}{\partial y} - r_2 v_2 + \nu_2\frac{\partial^2 v_2}{\partial y^2}, \qquad (2.23)$$

where (2.10) and (2.13) are now redundant. We note that the horizontal components of the upper layer momentum equation (2.20) and (2.21) simplify to

$$\frac{Du_1}{Dt} + (f_0 + \beta y)(-v_1) = -\frac{\partial\tilde{p}_1(x,y,t)}{\partial x} + \nu_1\frac{\partial^2 u_1}{\partial x^2}, \qquad (2.24)$$

$$\frac{Dv_1}{Dt} + (f_0 + \beta y)(u_1) = -\frac{\partial\tilde{p}_1(x,y,t)}{\partial y} + \nu_1\frac{\partial^2 v_1}{\partial y^2}. \qquad (2.25)$$

From (2.24) and (2.25) it is clear that by applying the hydrostatic assumption, that the horizontal velocities, u_1 and v_1, are now independent of depth. The same argument applies in the lower layer, implying that u_2 and v_2 are also independent of depth. We are thus able to make a fundamental simplification. We transform the three-dimensional system to a two-dimensional system by incorporating the vertical effects into the horizontal equations. It will become clear as the derivation progresses that the continuity equations (2.14) and (2.15) allow this inclusion of vertical effects by connecting vertical velocities to changes in upper-layer height, h. In keeping with this simplification, we define

$$\mathbf{u}_{1,H} = (u_1, v_1), \qquad (2.26)$$

$$\mathbf{u}_{2,H} = (u_2, v_2),$$

to be the horizontal components of the velocity vector in each layer. As well, we require two-dimensional analogues of our standard three-dimensional operators. Thus we define

$$\nabla_H := \left(\frac{\partial}{\partial x}, \frac{\partial}{\partial y}\right), \qquad (2.27)$$

and

$$\hat{\mathbf{k}} \times \mathbf{u}_H := \begin{vmatrix} \hat{\mathbf{i}} & \hat{\mathbf{j}} & \hat{\mathbf{k}} \\ 0 & 0 & 1 \\ u & v & 0 \end{vmatrix}_H = (-v, u, 0)|_H = (-v, u). \qquad (2.28)$$

From (2.27) and (2.28) we note the following important identity:

$$\hat{\mathbf{k}} \cdot (\nabla_H \times (a, b)) = \hat{\mathbf{k}} \cdot \begin{vmatrix} \hat{\mathbf{i}} & \hat{\mathbf{j}} & \hat{\mathbf{k}} \\ \frac{\partial}{\partial x} & \frac{\partial}{\partial y} & 0 \\ a & b & 0 \end{vmatrix} = \hat{\mathbf{k}} \cdot \left(\frac{\partial b}{\partial x} - \frac{\partial a}{\partial y} \right) \hat{\mathbf{k}} = \frac{\partial b}{\partial x} - \frac{\partial a}{\partial y}. \qquad (2.29)$$

We also define the two-dimensional restriction of (2.7) as

$$(f_0 + \beta y) \begin{pmatrix} -v \\ u \\ 0 \end{pmatrix}_H := (f_0 + \beta y)\hat{\mathbf{k}} \times \mathbf{u}_H, \qquad (2.30)$$

where f_0 is defined by (2.4) and β is defined by (2.6).

We continue our derivation focusing on the upper layer, with the derivation for the lower layer being entirely analogous, unless otherwise stated.

We first replace $\mathbf{u}_1$ by $\mathbf{u}_{1,H}$ in (2.8)–(2.9), let all operators be their two-dimensional analogues where applicable (as defined in (2.27)–(2.28)) and replace the Coriolis term with (2.30), giving, in vector form,

$$\frac{D\mathbf{u}_{1,H}}{Dt} + (f_0 + \beta y)\hat{\mathbf{k}} \times \mathbf{u}_{1,H} = -\frac{1}{\bar{\rho}}\nabla_H \tilde{p}_1(x, y, t) + \nu_1 \nabla_H^2 \mathbf{u}_{1,H}, \qquad (2.31)$$

where we have replaced ∇p_1 by $\nabla \tilde{p}_1$ following (2.24) and (2.25). We further assume a continuous pressure across the layer interface (i.e., at $z = -h_1(x, y, t)$). Then (2.18) gives

$$g\rho_1 h_1(x, y, t) + \bar{\rho}\tilde{p}_1(x, y, t) = g\rho_2 h_1(x, y, t) + \bar{\rho}\tilde{p}_2(x, y, t),$$

from which we can solve for $\tilde{p}_1(x, y, t)$ as

$$\tilde{p}_1(x, y, t) = g\left(\frac{\rho_2 - \rho_1}{\bar{\rho}}\right)h_1(x, y, t) + \tilde{p}_2(x, y, t). \qquad (2.32)$$

We substitute this into (2.31), giving

$$\frac{D\mathbf{u}_{1,H}}{Dt} + (f_0 + \beta y)\hat{\mathbf{k}} \times \mathbf{u}_{1,H} = -g'\nabla_H h_1(x, y, t) - \nabla_H \tilde{p}_2(x, y, t) + \nu_1 \nabla_H^2 \mathbf{u}_{1,H}, \quad (2.33)$$

where $g' := g\left(\frac{\rho_2 - \rho_1}{\bar{\rho}}\right)$ is the *reduced gravity* [17].

We now expand the upper-layer continuity equation (2.11) to

$$\frac{\partial u_1}{\partial x} + \frac{\partial v_1}{\partial y} + \frac{\partial w_1}{\partial z} = 0,$$

and then integrate both sides over the depth of the upper layer, noting that u_1 and v_1 are independent of z, to obtain

$$\int_{-h_1(x,y,t)}^{0} \left(\frac{\partial u_1}{\partial x} + \frac{\partial v_1}{\partial y} + \frac{\partial w_1}{\partial z} \right) dz$$

$$= h_1(x,y,t) \left(\frac{\partial u_1}{\partial x} + \frac{\partial v_1}{\partial y} \right) + w(x,y,0,t) - w(x,y,-h_1(x,y,t),t) = 0. \qquad (2.34)$$

We account for the wind forcing by including a downward *Ekman pumping force* [12] at the surface of the upper layer; i.e,

$$w(x,y,0,t) = \tau_0 w_{1,e}(x,y,t), \qquad (2.35)$$

where τ_0 is a wind strength parameter and

$$w_{1,e}(x,y,t) = \begin{cases} w_e(x,y,t) & \text{if } h_1(x,y,t) > 0, \\ 0 & \text{if } h_1(x,y,t) = 0, \end{cases} \qquad (2.36)$$

where $w_e(x,y,t)$ is the Ekman pumping velocity. Incorporating the wind forcing in this manner is a distinguishing feature of this model as compared to other similar models. Because we model the resultant Ekman pumping force instead of the wind forcing directly, we do not include the surface Ekman layer in our model geometry, but instead include the effect of this Ekman layer on the subsurface ocean.

At the interface of the two layers, $z = -h_1(x,y,t)$, we apply a kinematic boundary condition (see [19]), such that the vertical velocity is given by the total change in the upper layer depth with respect to time; i.e.,

$$w(x,y,-h_1(x,y,t),t) = -\frac{Dh_1(x,y,t)}{Dt} = -\left[\frac{\partial h(x,y,t)}{\partial t} + \mathbf{u}_{1,H} \cdot \nabla_H h(x,y,t). \right] \qquad (2.37)$$

We substitute (2.35) and (2.37) into (2.34), noting that

$$h_1(x,y,t)\nabla_H \cdot \mathbf{u}_{1,H} + \mathbf{u}_{1,H}\nabla_H h_1(x,y,t) = \nabla_H \cdot (h_1(x,y,t)\mathbf{u}_{1,H}),$$

to obtain

$$\frac{\partial h_1(x,y,t)}{\partial t} + \nabla_H \cdot (h_1(x,y,t)\mathbf{u}_{1,H}) = -\tau_0 w_{1,e}(x,y,t). \qquad (2.38)$$

In the lower layer, the derivation is completely analogous. Thus, with the lower-layer analogues of (2.33) and (2.38), we arrive at the two-dimensional, two-layer shallow-water equations,

$$\frac{\partial \mathbf{u}_{1,H}}{\partial t} + \mathbf{u}_{1,H} \cdot \nabla_H \mathbf{u}_{1,H} + (f_0 + \beta y)\hat{\mathbf{k}} \times \mathbf{u}_{1,H}$$
$$= -g'\nabla_H h_1(x,y,t) - \nabla_H p_2(x,y,t) + \nu_1 \nabla_H^2 \mathbf{u}_{1,H}, \tag{2.39}$$

$$\frac{\partial h_1(x,y,t)}{\partial t} + \nabla_H \cdot (h_1(x,y,t)\mathbf{u}_{1,H}) = -\tau_0 w_{1,e}(x,y,t), \tag{2.40}$$

$$\frac{\partial \mathbf{u}_{2,H}}{\partial t} + \mathbf{u}_{2,H} \cdot \nabla_H \mathbf{u}_{2,H} + (f_0 + \beta y)\hat{\mathbf{k}} \times \mathbf{u}_{2,H}$$
$$= -\nabla_H p_2(x,y,t) - r_2 \mathbf{u}_{2,H} + \nu_2 \nabla_H^2 \mathbf{u}_{2,H}, \tag{2.41}$$

$$\frac{\partial h_2(x,y,t)}{\partial t} + \nabla_H \cdot (h_2(x,y,t)\mathbf{u}_{2,H}) = -\tau_0 w_{2,e}(x,y,t), \tag{2.42}$$

where

$$w_{2,e}(x,y,t) = \begin{cases} 0 & \text{if } h_1(x,y,t) > 0, \\ w_e(x,y,t) & \text{if } h_1(x,y,t) = 0. \end{cases} \tag{2.43}$$

We have defined our Ekman pumping forces in the upper layer (2.36) and lower layer (2.43) such that the forcing is applied on each layer only where that layer reaches the surface. In a typical model run, the upper layer covers the entire surface of the domain (i.e., $h(x,y,t) > 0$ everywhere on the domain). In this case, no forcing would be applied to the lower layer. However, there is also the case of *outcropping*, i.e., where the upper layer vanishes on some region of the domain, and the lower-layer outcrops, or reaches the surface. In this case, $w_e(x,y,t)$ is applied to the lower layer via (2.43) on the outcropping region.

Because our model deals with a number of variables, we seek to redefine these variables on a scale which allows each variable to be compared. This is accomplished by a nondimensionalization (see, e.g., [26]), wherein we rewrite our variables with associated characteristic scales. Thus, let

$$x = L\tilde{x}, \qquad y = L\tilde{y}, \qquad t = T\tilde{t}, \qquad \mathbf{u}_{1,H} = U_1 \tilde{\mathbf{u}}_{1,H}, \quad h_1 = H_1 \tilde{h}_1,$$
$$\mathbf{u}_{2,H} = U_2 \tilde{\mathbf{u}}_{2,H}, \quad p = P\tilde{p}_2, \quad w_{1,e} = W\tilde{w}_{1,e}, \quad w_{2,e} = W\tilde{w}_{2,e}$$

where L is a characteristic length scale, T is a characteristic time scale, U_1 and U_2 are characteristic horizontal velocity scales, H_1 and H_2 are characteristic layer depth scales, P is a characteristic pressure scale, and W is a characteristic Ekman pumping velocity scale.

We expand and rewrite equations (2.39)–(2.42) with the nondimensionalized variables, dropping the tildes, and suppressing all arguments:

$$\frac{U_1}{T}\frac{\partial u_1}{\partial t} + \frac{U_1^2}{L}u_1\frac{\partial u_1}{\partial x} + \frac{U_1^2}{L}v_1\frac{\partial u_1}{\partial y} - (f_0 + \beta y)U_1 v_1$$

$$= \frac{-g'H_1}{L}\frac{\partial h_1}{\partial x} - \frac{P}{L}\frac{\partial p_2}{\partial x} + \frac{U_1^2}{L^2}\nu_1\frac{\partial^2 u_1}{\partial x^2}, \tag{2.44}$$

$$\frac{U_1}{T}\frac{\partial v_1}{\partial t} + \frac{U_1^2}{L}u_1\frac{\partial v_1}{\partial x} + \frac{U_1^2}{L}v_1\frac{\partial v_1}{\partial y} + (f_0 + \beta y)U_1 u_1$$

$$= \frac{-g'H_1}{L}\frac{\partial h_1}{\partial y} - \frac{P}{L}\frac{\partial p_2}{\partial y} + \frac{U_1^2}{L^2}\nu_1\frac{\partial^2 v_1}{\partial y^2}, \tag{2.45}$$

$$\frac{H_1}{T}\frac{\partial h_1}{\partial t} + \frac{H_1 U_1}{L}\left(\frac{\partial h_1 u_1}{\partial x} + \frac{\partial h_1 u_1}{\partial y}\right) = -W\tau_0 w_{1,e}, \tag{2.46}$$

$$\frac{U_2}{T}\frac{\partial u_2}{\partial t} + \frac{U_2^2}{L}u_2\frac{\partial u_2}{\partial x} + \frac{U_2^2}{L}v_2\frac{\partial u_2}{\partial y} - (f_0 + \beta y)U_2 v_2$$

$$= -\frac{P}{L}\frac{\partial p_2}{\partial x} - U_2 r_2 u_2 + \frac{U_2^2}{L^2}\nu_2\frac{\partial^2 u_2}{\partial x^2}, \tag{2.47}$$

$$\frac{U_2}{T}\frac{\partial v_2}{\partial t} + \frac{U_2^2}{L}u_2\frac{\partial v_2}{\partial x} + \frac{U_2^2}{L}v_2\frac{\partial v_2}{\partial y} + (f_0 + \beta y)U_2 u_2$$

$$= -\frac{P}{L}\frac{\partial p_2}{\partial y} - U_2 r_2 v_2 + \frac{U_2^2}{L^2}\nu_2\frac{\partial^2 v_2}{\partial y^2}, \tag{2.48}$$

$$\frac{H_2}{T}\frac{\partial h_2}{\partial t} + \frac{H_2 U_2}{L}\left(\frac{\partial h_2 u_2}{\partial x} + \frac{\partial h_2 u_2}{\partial y}\right) = -W\tau_0 w_{2,e}. \tag{2.49}$$

Also, we note that

$$H_1 h_1 + H_2 h_2 = H, \tag{2.50}$$

with H the total depth. We now divide (2.44) and (2.45) by $U_1|f_0|$, and (2.46) by $H_1|f_0|$, noting that because we are dealing with a flow in the southern hemisphere, $\theta_0 < 0$, and hence $f_0 < 0$:

$$\frac{1}{T|f_0|}\frac{\partial u_1}{\partial t} + \frac{U_1}{L|f_0|}u_1\frac{\partial u_1}{\partial x} + \frac{U_1}{L|f_0|}v_1\frac{\partial u_1}{\partial y} - \frac{(f_0 + \beta y)}{|f_0|}v_1$$

$$= \frac{-g'H_1}{L|f_0|U_1}\frac{\partial h_1}{\partial x} - \frac{P}{L|f_0|U_1}\frac{\partial p_2}{\partial x} - \frac{r_2}{|f_0|}u_1 + \frac{U_1}{|f_0|L^2}\nu_2\frac{\partial^2 u_1}{\partial x^2}, \tag{2.51}$$

$$\frac{1}{T|f_0|}\frac{\partial v_1}{\partial t} + \frac{U_1}{L|f_0|}u_1\frac{\partial v_1}{\partial x} + \frac{U_1}{L|f_0|}v_1\frac{\partial v_1}{\partial y} + \frac{(f_0 + \beta y)}{|f_0|}u_1$$

$$= \frac{-g'H_1}{L|f_0|U_1}\frac{\partial h_1}{\partial y} - \frac{P}{L|f_0|U_1}\frac{\partial p_2}{\partial y}, - \frac{r_2}{|f_0|}v_1 + \frac{U_1}{|f_0|L^2}\nu_2\frac{\partial^2 v_1}{\partial y^2} \tag{2.52}$$

$$\frac{1}{T|f_0|}\frac{\partial h_1}{\partial t} + \frac{U_1}{L|f_0|}\left(\frac{\partial h_1 u_1}{\partial x} + \frac{\partial h_1 u_1}{\partial y}\right) = -\frac{W}{|f_0|H_1}\tau_0 w_{1,e}. \tag{2.53}$$

Similarly, we divide (2.47) and (2.48) by $U_2|f_0|$ and (2.49) by $H_2|f_0|$ to obtain

$$\frac{1}{T|f_0|}\frac{\partial u_2}{\partial t} + \frac{U_2}{L|f_0|}u_2\frac{\partial u_2}{\partial x} + \frac{U_2}{L|f_0|}v_2\frac{\partial u_2}{\partial y} - \frac{(f_0 + \beta y)}{|f_0|}v_2$$

$$= -\frac{P}{L|f_0|U_2}\frac{\partial p_2}{\partial x} - \frac{1}{|f_0|}r_2 u_2 + \frac{U_2}{|f_0|L^2}\nu_2\frac{\partial^2 u_2}{\partial x^2}, \tag{2.54}$$

$$\frac{1}{T|f_0|}\frac{\partial v_2}{\partial t} + \frac{U_2}{L|f_0|}u_2\frac{\partial v_2}{\partial x} + \frac{U_2}{L|f_0|}v_2\frac{\partial v_2}{\partial y} + \frac{(f_0 + \beta y)}{|f_0|}u_2$$

$$= -\frac{P}{L|f_0|U_2}\frac{\partial p_2}{\partial y} - \frac{1}{|f_0|}r_2 v_2 + \frac{U_2}{|f_0|L^2}\nu_2\frac{\partial^2 v_2}{\partial y^2}, \tag{2.55}$$

$$\frac{1}{T|f_0|}\frac{\partial h_2}{\partial t} + \frac{U_2}{L|f_0|}\left(\frac{\partial h_2 u_2}{\partial x} + \frac{\partial h_2 u_2}{\partial y}\right) = \frac{-W}{|f_0|H_2}\tau_0 w_{2,e}. \tag{2.56}$$

We now seek to determine the relative sizes of the non-dimensionalized variables. For this we define the *Rossby number*, ϵ, as the ratio of the nonlinear acceleration to the Coriolis force. The Rossby number has magnitude

$$\epsilon := \frac{U_1^2/L}{|f_0|U_1} = \frac{U_1}{|f_0|L}. \tag{2.57}$$

A small Rossby number; i.e., $\epsilon \ll 1$ (calculations are preformed in Chapter 3) implies a geostrophic balance in our model.

From (2.4) and (2.6), and noting that $L < R$, it is clear that at mid-latitudinal θ_0 values, $\beta y \ll f_0$. Then the coefficient of the Coriolis term in (2.51) and (2.52) satisfies

$$\frac{(f_0 + \beta y)}{|f_0|} = O(1).$$

Furthermore, geostrophic flow in the upper layer implies that both the Coriolis terms and pressure gradient terms in (2.51) and (2.52) are leading-order terms. Then it follows that the pressure gradient terms in (2.51) and (2.52) are also $O(1)$, and we thus set

$$\frac{-g'H_1}{L|f_0|U_1} = 1, \tag{2.58}$$

and

$$\frac{P}{L|f_0|U_1} = 1, \tag{2.59}$$

because these are the coefficients of the expanded normalized pressure $\tilde{p}_1(x, y, t)$ given by (2.32). At this point, we make a number of assumptions in the scaling of our variables. Depending on the chosen scaling, there are a number of models which can be derived; these are described in detail in [15]. Our scaling choice corresponds to the weak-β, thin-layer (WT) model from [15]. Continuing with this scaling, we assume the flow in the lower layer is an order of ϵ smaller than the upper layer; i.e.,

$$U_2 = \epsilon U_1 = \epsilon^2 |f_0| L. \tag{2.60}$$

We assume as well that the time scale is given by the advective scale in the lower layer; i.e.,

$$T = \frac{L}{U_2} = \frac{1}{\epsilon^2 |f_0|}. \tag{2.61}$$

Also, we assume a thin upper layer; i.e.,

$$H_1 = \mu \epsilon^2 H_2, \tag{2.62}$$

and

$$H_2 = H. \tag{2.63}$$

We include the additional parameter μ in (2.62) to more accurately compare the layer depths. In our model of the ACC, μ has a value of 1.21 (see Section 3.3). We choose

an upper-layer wind forcing of order $O(\epsilon^2)$; i.e.,

$$\frac{W}{|f_0|H_1} = \epsilon^2. \tag{2.64}$$

From (2.62) and (2.64), we can determine the lower-layer wind forcing scale:

$$\frac{W}{|f_0|H_2} = \mu\epsilon^2 \frac{W}{|f_0|H_1} = \mu\epsilon^4. \tag{2.65}$$

With the assumptions (2.58)–(2.65), we can rewrite (2.51)–(2.56) in terms of the original variables and ϵ, except for the following: the Coriolis term,

$$\frac{1}{|f_0|}\beta y$$

in (2.51), (2.52), (2.54), and (2.55), the upper-layer Laplacian friction term

$$\frac{U_1}{|f_0|L^2}\nu_1 \nabla_H^2 \mathbf{u}_{1,H}$$

in (2.51) and (2.52), and the lower-layer friction terms

$$\frac{r_2}{|f_0|}\mathbf{u}_{2,H} \quad \text{and} \quad \frac{U_2}{|f_0|L^2}\nu_2 \nabla_H^2 \mathbf{u}_{2,H}$$

in (2.54)–(2.55). Because each of these terms involve one of the model parameters β, r_2, ν_1 or ν_2, we can redefine these parameters such that we eliminate scaling factors, while also associating the aforementioned Coriolis term and friction terms with a more representative order of magnitude of ϵ. Thus, we write

$$\frac{1}{|f_0|}\beta y := \epsilon^2 \beta' y,$$

$$\frac{U_1}{|f_0|L^2}\nu_1 := \epsilon\nu_1' = \epsilon^2\nu_2', \tag{2.66}$$

$$\frac{1}{|f_0|}r_2 := \epsilon^2 r_2',$$

where β', r_2', ν_1', and ν_2' are suitably scaled parameters. Also, from (2.66) and (2.60), we have that

$$\frac{U_2}{|f_0|L^2}\nu_2 \nabla_H^2 \mathbf{u}_{2,H} = \epsilon^2 \nu_2' \nabla_H^2 \mathbf{u}_{2,H}.$$

We now divide (2.50) by H,

$$\frac{H_1}{H}h_1 + \frac{H_2}{H}h_2 = 1,$$

and using (2.62) and (2.63), we can then express h_2 in terms of h_1:

$$h_2 := 1 - \mu\epsilon^2 h_1. \tag{2.67}$$

By applying (2.58)–(2.67) to (2.51)–(2.56) and simplifying, we arrive at the *non-dimensional two-layer shallow-water equations*:

$$\epsilon^2 \frac{\partial \mathbf{u}_{1,H}}{\partial t} + \epsilon\left(\mathbf{u}_{1,H} \cdot \nabla_H \mathbf{u}_{1,H}\right) + (-1 + \epsilon^2 \beta' y)\hat{\mathbf{k}} \times \mathbf{u}_{1,H}$$

$$= -\nabla_H h_1 - \epsilon\left(\nabla_H p + \nu_1' \nabla_H^2 \mathbf{u}_{1,H}\right), \tag{2.68}$$

$$\epsilon \frac{\partial h_1}{\partial t} + \nabla_H \cdot (h_1 \mathbf{u}_{1,H}) = -\epsilon\tau_0 w_{1,e}, \tag{2.69}$$

$$\epsilon^2 \frac{\partial \mathbf{u}_{2,H}}{\partial t} + \epsilon^2 (\mathbf{u}_{2,H} \cdot \nabla_H)\mathbf{u}_{2,H} + (-1 + \epsilon^2 \beta' y)\hat{\mathbf{k}} \times \mathbf{u}_{2,H}$$

$$= -\nabla_H p - \epsilon^2 \left(r_2' \mathbf{u}_{2,H} - \nu_2' \nabla_H^2 \mathbf{u}_{2,H}\right), \tag{2.70}$$

$$-\mu\epsilon^2 \frac{\partial h_1}{\partial t} + \nabla_H \cdot \left((1 - \epsilon^2 \mu h_1)\mathbf{u}_{2,H}\right) = -\epsilon^2 \mu\tau_0 w_{2,e}, \tag{2.71}$$

where we have suppressed arguments of variables for notational ease. Henceforth, we also suppress the subscript 1 on h. We now rewrite the upper-layer momentum equation (2.68) as

$$\hat{\mathbf{k}} \times \mathbf{u}_{1,H} = \nabla_H h + \epsilon\left(\nabla_H p + (\mathbf{u}_{1,H} \cdot \nabla_H)\,\mathbf{u}_{1,H} - \nu_1' \nabla_H^2 \mathbf{u}_{1,H}\right) + O(\epsilon^2). \tag{2.72}$$

We then take $\hat{\mathbf{k}} \times$ (2.72) and drop $O(\epsilon^2)$ terms to obtain

$$\hat{\mathbf{k}} \times \left(\hat{\mathbf{k}} \times \mathbf{u}_{1,H}\right) = \hat{\mathbf{k}} \times \left[\nabla_H h + \epsilon\left(\nabla_H p + (\mathbf{u}_{1,H} \cdot \nabla_H)\,\mathbf{u}_{1,H} - \nu_1' \nabla_H^2 \mathbf{u}_{1,H}\right)\right].$$

This allows us to use the vector identity

$$\hat{\mathbf{k}} \times (\hat{\mathbf{k}} \times \mathbf{v}) = -\mathbf{v} \tag{2.73}$$

to solve implicitly for $\mathbf{u}_{1,H}$:

$$\mathbf{u}_{1,H} = -\hat{\mathbf{k}} \times \left[\nabla_H h + \epsilon\left(\nabla_H p + (\mathbf{u}_{1,H} \cdot \nabla_H)\,\mathbf{u}_{1,H} - \nu_1' \nabla_H^2 \mathbf{u}_{1,H}\right)\right]. \tag{2.74}$$

We expand

$$\mathbf{u}_{1,H} = \mathbf{u}_{1,H}^{(0)} + \epsilon \mathbf{u}_{1,H}^{(1)} + \cdots.$$

It is clear from (2.74) that

$$\mathbf{u}_{1,H}^{(0)} = -\hat{\mathbf{k}} \times \nabla_H h. \tag{2.75}$$

We can use $\mathbf{u}_{1,H}^{(0)}$ as an approximation for $\mathbf{u}_{1,H}$ to simplify the right-hand side of (2.74), giving

$$\mathbf{u}_{1,H} =$$

$$-\hat{\mathbf{k}} \times \left[\nabla_H h + \epsilon \left(\nabla_H p + ((\hat{\mathbf{k}} \times \nabla_H h) \cdot \nabla_H)(\hat{\mathbf{k}} \times \nabla_H h) + \nu_1' \nabla_H^2 (\hat{\mathbf{k}} \times \nabla_H h) \right) \right]. \tag{2.76}$$

We simplify this expression by noting that

$$
\begin{aligned}
-\hat{\mathbf{k}} \times \left[((\hat{\mathbf{k}} \times \nabla_H h) \cdot \nabla_H)(\hat{\mathbf{k}} \times \nabla_H h) \right] &= -\hat{\mathbf{k}} \times \left(\begin{bmatrix} -h_y \\ h_x \end{bmatrix} \cdot \begin{bmatrix} \frac{\partial}{\partial x} \\ \frac{\partial}{\partial y} \end{bmatrix} \right) \begin{bmatrix} -h_y \\ h_x \end{bmatrix} \\
&= -\hat{\mathbf{k}} \times \left(-h_y \frac{\partial}{\partial x} + h_x \frac{\partial}{\partial y} \right) \begin{bmatrix} -h_y \\ h_x \end{bmatrix} \\
&= -\hat{\mathbf{k}} \times \begin{bmatrix} h_y h_{yx} - h_x h_{yy} \\ -h_y h_{xx} + h_x h_{xy} \end{bmatrix} \\
&= \begin{bmatrix} h_x \\ h_y \end{bmatrix}_x h_y - h_x \begin{bmatrix} h_x \\ h_y \end{bmatrix}_y \\
&:= J(\nabla_H h, h),
\end{aligned}
$$

where $J(A, B) := A_x B_y - A_y B_x$ denotes the Jacobian in the determinant sense. Then we can write (2.76) as

$$\mathbf{u}_{1,H} = -\hat{\mathbf{k}} \times \nabla_H h - \epsilon \left[\hat{\mathbf{k}} \times \nabla_H p + J(\nabla_H h, h) - \nu_1' \nabla_H^2 \nabla h \right]. \tag{2.77}$$

From (2.77),

$$\mathbf{u}_{1,H}^{(1)} = -\hat{\mathbf{k}} \times \nabla_H p - J(\nabla_H h, h) + \nu_1' \nabla_H^2 \nabla h.$$

Substituting (2.77) into (2.69) and noting that the geostrophic velocity cannot advect the upper-layer depth [12], i.e.,

$$\nabla_H \cdot (\mathbf{u}_{1,H}^{(0)} h) = 0,$$

at order ϵ we get

$$\frac{\partial h}{\partial t} + \nabla_H \cdot \left(h\mathbf{u}_{1,H}^{(1)} \right) = \tau_0 w_{1,e}. \tag{2.78}$$

We similarly rearrange the lower-layer momentum equation (2.70) to get

$$-\hat{\mathbf{k}} \times \mathbf{u}_{2,H} = -\nabla_H p + O(\epsilon)$$

and again using (2.73), solve for $\mathbf{u}_{2,H}$, giving

$$\mathbf{u}_{2,H} = -\hat{\mathbf{k}} \times \nabla_H p + O(\epsilon). \tag{2.79}$$

Expanding $\mathbf{u}_{2,H}$ as

$$\mathbf{u}_{2,H} = \mathbf{u}_{2,H}^{(0)} + \epsilon \mathbf{u}_{2,H}^{(1)} + \cdots,$$

we note from (2.79) that the lower-layer geostrophic velocity is

$$\mathbf{u}_{2,H}^{(0)} = -\hat{\mathbf{k}} \times \nabla_H p. \tag{2.80}$$

We continue by applying the identity (2.29) to the momentum equation (2.70), giving

$$\hat{\mathbf{k}} \cdot \left(\nabla_H \times \left[\epsilon^2 \frac{\partial \mathbf{u}_{2,H}}{\partial t} + \epsilon^2 ((\mathbf{u}_{2,H} \cdot \nabla_H)\mathbf{u}_{2,H}) + (-1 + \epsilon^2 \beta' y)\hat{\mathbf{k}} \times \mathbf{u}_{2,H} \right] \right)$$

$$= \hat{\mathbf{k}} \cdot \left(\nabla_H \times [-\nabla_H p - \epsilon^2 (r_2' \mathbf{u}_{2,H} - \nu_2' \nabla_H^2 \mathbf{u}_{2,H})] \right),$$

or

$$\epsilon^2 \frac{\partial \hat{\mathbf{k}} \cdot (\nabla_H \times \mathbf{u}_{2,H})}{\partial t} + \epsilon^2 \hat{\mathbf{k}} \cdot (\nabla_H \times ((\mathbf{u}_{2,H} \cdot \nabla_H)\mathbf{u}_{2,H})) + \hat{\mathbf{k}} \cdot \left(\nabla_H \times [(-1 + \epsilon^2 \beta' y)\hat{\mathbf{k}} \times \mathbf{u}_{2,H}] \right)$$

$$= \hat{\mathbf{k}} \cdot \left(\nabla_H \times [-\nabla_H p - \epsilon^2 (r_2' \mathbf{u}_{2,H} - \nu_2' \nabla_H^2 \mathbf{u}_{2,H})] \right). \tag{2.81}$$

But, noting that

$$\hat{\mathbf{k}} \cdot \left(\nabla_H \times \left[(-1 + \epsilon^2 \beta' y)\hat{\mathbf{k}} \times \mathbf{u}_{2,H} \right] \right) = \nabla_H \cdot \left((-1 + \epsilon^2 \beta' y)\mathbf{u}_{2,H} \right), \tag{2.82}$$

and also that

$$\nabla_H \times \nabla_H p = \mathbf{0},$$

we can simplify (2.81) to

$$\epsilon^2 \frac{\partial \hat{\mathbf{k}} \cdot (\nabla_H \times \mathbf{u}_{2,H})}{\partial t} + \epsilon^2 \hat{\mathbf{k}} \cdot (\nabla_H \times ((\mathbf{u}_{2,H} \cdot \nabla_H)\mathbf{u}_{2,H})) + \nabla_H \cdot \left((-1 + \epsilon^2 \beta' y)\mathbf{u}_{2,H} \right)$$
$$= -\epsilon^2 \left(r_2' \hat{\mathbf{k}} \cdot (\nabla_H \times \mathbf{u}_{2,H}) - \nu_2' \hat{\mathbf{k}} \cdot \left(\nabla_H^2 \nabla_H \times \mathbf{u}_{2,H} \right) \right), \tag{2.83}$$

which we call the *vorticity equation* [12]. Noting that

$$\hat{\mathbf{k}} \cdot (\nabla_H \times [(\mathbf{u}_{2,H} \cdot \nabla_H)\, \mathbf{u}_{2,H}]) = \nabla_H \cdot \left(\left[\hat{\mathbf{k}} \cdot (\nabla_H \times \mathbf{u}_{2,H}) \right] \mathbf{u}_{2,H} \right),$$

we can rewrite (2.83) as

$$\epsilon^2 \frac{\partial \zeta}{\partial t} + \nabla_H \cdot \left(\left(\epsilon^2 \zeta - 1 + \epsilon^2 \beta' y \right) \mathbf{u}_{2,H} \right) = -\epsilon^2 \left(r_2' \zeta - \nu_2' \nabla_H^2 \zeta \right), \tag{2.84}$$

where $\zeta = \hat{\mathbf{k}} \cdot (\nabla_H \times \mathbf{u}_{2,H})$ is the *relative vorticity* [17].

We now rewrite (2.84) as follows:

$$\nabla_H \cdot \mathbf{u}_{2,H} = \epsilon^2 \left(\frac{\partial \zeta}{\partial t} + \nabla_H \cdot [(\zeta + \beta' y)\mathbf{u}_{2,H}] + r_2' \zeta - \nu_2' \nabla_H^2 \zeta \right). \tag{2.85}$$

We approximate $\mathbf{u}_{2,H}$ on the right-hand side of (2.85) with the geostrophic velocity in the lower layer $\mathbf{u}_{2,H}^{(0)}$, and use (2.80) to approximate ζ by

$$\zeta^{(0)} = \hat{\mathbf{k}} \cdot \left(\nabla_H \times \mathbf{u}_{2,H}^{(0)} \right) = -\nabla_H^2 p,$$

to get

$$\nabla_H \cdot \mathbf{u}_{2,H} = -\epsilon^2 \left(\frac{\partial \nabla_H^2 p}{\partial t} + \nabla_H \cdot \left[(\nabla_H^2 p - \beta' y)\mathbf{u}_{2,H}^{(0)} \right] + r_2' \nabla_H^2 p - \nu_2' \nabla_H^4 p \right). \tag{2.86}$$

We now consider the lower-layer depth equation (2.71). Expanding and using (2.86), we rewrite (2.71) as

$$-\mu \epsilon^2 \frac{\partial h}{\partial t} - \epsilon^2 \left(\frac{\partial \nabla_H^2 p}{\partial t} + \nabla_H \cdot \left[(\nabla_H^2 p - \beta' y)\mathbf{u}_{2,H}^{(0)} \right] + r_2' \nabla_H^2 p - \nu_2' \nabla_H^4 p \right)$$
$$-\epsilon^2 \nabla_H \cdot ((\mu h)\mathbf{u}_{2,H}) = -\epsilon^2 \mu \tau_0 w_{2,e}. \tag{2.87}$$

We approximate $\mathbf{u}_{2,H}$ in (2.87) by $\mathbf{u}_{2,H}^{(0)}$ and divide by $-\epsilon^2$ to get

$$\frac{\partial q}{\partial t} + \nabla_H \cdot \left(q\mathbf{u}_{2,H}^{(0)} \right) = \mu \tau_0 w_{2,e} - r_2' \nabla_H^2 p + \nu_2' \nabla_H^4 p \tag{2.88}$$

where

$$q := \nabla_H^2 p + \mu h - \beta' y. \tag{2.89}$$

Equation (2.88) is called the *potential vorticity* equation, where q, defined in (2.89), is the *potential vorticity*. This expression for potential vorticity can be independently derived by reduction of the shallow-water analogue of potential vorticity (see [19]).

Combining (2.78) and (2.88), we have the *advective form* of the two-layer FG model equations,

$$\frac{\partial h}{\partial t} + \nabla_H \cdot \left(h \mathbf{u}_{1,H}^{(1)} \right) = -\tau_0 w_{1,e}, \tag{2.90}$$

$$\frac{\partial q}{\partial t} + \nabla_H \cdot \left(q \mathbf{u}_{2,H}^{(0)} \right) = \mu \tau_0 w_{2,e} - r_2' \nabla_H^2 p + \nu_2' \nabla_H^4 p \tag{2.91}$$

where

$$\mathbf{u}_{1,H}^{(1)} = -\hat{\mathbf{k}} \times \nabla_H p - J(\nabla_H h, h) + \nu_1' \nabla_H^2 \nabla h, \tag{2.92}$$

$$\mathbf{u}_{2,H}^{(0)} = -\hat{\mathbf{k}} \times \nabla_H p, \tag{2.93}$$

and

$$q = \nabla_H^2 p + \mu h - \beta' y. \tag{2.94}$$

2.3   Spatial Domain, and Boundary Conditions

The ACC flows continuously eastward around the globe. Because the meridional spread and the depth scale of the ACC are sufficiently small, we can approximate the spatial domain of the ACC by a geometrically simple channel with periodic boundary conditions in the direction of flow (see Figure 2.9). We investigate a number of different channels with our model. We are interested in the effect of the presence of land masses on the flow, and so we run our model first in a simple channel with no land masses and then include a land barrier in our domain, such that we can compare the nature of the flow in each case.
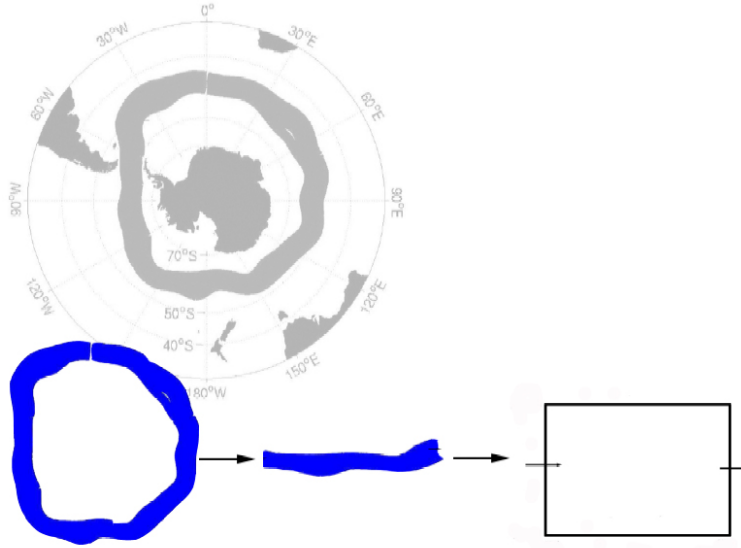
Figure 2.9: The true shape of the domain of the ACC is approximated by a simple periodic rectangular domain.

2.3.1 Simple Channel

In the simplest domain, we approximate the domain of the ACC by a rectangular region. With x oriented east-west and y oriented north-south, we express the nondimensionalized domain as

$$x_L \leq x \leq x_R,$$

$$0 \leq y \leq D,$$

where x_L, x_R, and D are suitably chosen real numbers. Because the mean oceanic flow is oriented east to west, we impose periodic boundary conditions in x; i.e.,

$$h(x_L, y, t) = h(x_R, y, t), \quad p(x_L, y, t) = p(x_R, y, t). \tag{2.95}$$

From (2.94), $q(x, y, t)$ is dependent only on $p(x, y, t)$, $h(x, y, t)$, and y. Then the periodicity in $h(x, y, t)$ and $p(x, y, t)$ implies periodicity in $q(x, y, t)$ as well. For the boundary conditions in y, we impose no-normal flow conditions on the upper and lower boundaries; i.e.,

$$v_1 = v_2 = 0 \ \text{ on } \ y = 0, D.$$

Recalling (2.75) and (2.80), the leading-order velocities in the upper and lower layer respectively are

$$\mathbf{u}_{1,H}^0 = -\hat{\mathbf{k}} \times \nabla_H h = \begin{bmatrix} h_y \\ -h_x \end{bmatrix}, \tag{2.96}$$

$$\mathbf{u}_{2,H}^0 = -\hat{\mathbf{k}} \times \nabla_H p = \begin{bmatrix} p_y \\ -p_x \end{bmatrix}. \tag{2.97}$$

Letting $v_1 = v_2 = 0$ in (2.96) and (2.97), we get that

$$h_x = 0 \ \text{ on } \ y = 0, D. \tag{2.98}$$

$$p_x = 0 \ \text{ on } \ y = 0, D. \tag{2.99}$$

These boundary conditions alone would create an ill-posed problem, however, because we cannot specify tangential derivatives on the boundary. At next order, we examine the upper-layer velocity,

$$\mathbf{u}_{1,H}^{(1)} = -\hat{\mathbf{k}} \times \nabla_H p - J(\nabla_H h, h) = \begin{bmatrix} p_y - h_{xx}h_y + h_{xy}h_x \\ -p_x - h_{xy}h_y + h_{yy}h_x \end{bmatrix}.$$

Imposing $v_1 = 0$ implies that

$$-p_x - h_{yx}h_y - h_{yy}h_x = 0.$$

Using (2.98) and (2.99) we can rewrite this boundary condition as

$$(h_y^2)_x = 0 \ \text{ on } \ y = 0, D. \tag{2.100}$$

We can now conclude that h_y is (at most) only a function of time on $y = 0, D$. Due to the aforementioned ill-posedness of our derived boundary conditions for $h(x, y, t)$ and $p(x, y, t)$, we must modify these conditions somewhat. We proceed with two methods of implementing a viable boundary condition on $h(x, y, t)$, with a short discussion of the effects of each implementation.

Boundary Method I for $h(x, y, t)$

We can enforce the condition on $h(x, y, t)$ from (2.98) and (2.100) by letting $h(x, y, t)$ be defined as only a function of time on $y = 0, D$. We implement this by defining a

Dirichlet condition for $h(x, y, t)$,

$$h(x, y, t) = h_{avg,0} \text{ on } y = 0,$$

$$h(x, y, t) = h_{avg,D} \text{ on } y = D.$$

Here, $h_{avg,0}$ is an average of 'nearby' values of $h(x, y, \hat{t})$ for some time $\hat{t}$; i.e.,

$$h_{avg,0} = \frac{1}{area(R_0)} \iint_{R_0} h(x, y, \hat{t}) dx dy, \tag{2.101}$$

where R_0 is a region near the boundary $y = 0$. Similarly, $h_{avg,D}$ is defined as

$$h_{avg,D} = \frac{1}{area(R_D)} \iint_{R_D} h(x, y, \hat{t}) dx dy, \tag{2.102}$$

where R_D is a region near the boundary $y = D$. With the above definition, $h(x, y, t)$ takes on a spatially constant, but time-dependent value on $y = 0, D$. In addition, the normal derivative of $h(x, y, t)$ at $y = 0, D$ is bounded by the deviation of $h(x, y, t)$ from the mean value (i.e., $h_{avg,0}$ or $h_{avg,D}$) along the boundary. In this sense, (2.101) and (2.102) approximate a Neumann condition for $h(x, y, t)$, i.e.,

$$\mathbf{n} \cdot \nabla_H h(x, y, t) \simeq 0, \text{ on } y = 0, D. \tag{2.103}$$

Because the upper-layer geostrophic velocity is along streamlines of $h(x, y, t)$, (2.103) is an approximation to a no-slip condition in the upper layer. Note that (2.103) also implies that (2.100) is approximately satisfied.

Boundary Method II for $h(x, y, t)$

Alternatively, we can directly impose

$$\mathbf{n} \cdot \nabla h = 0, \text{ on } y = 0, D,$$

such that we exactly impose a no-slip condition in the upper layer. However, this condition allows normal flow into the boundary; i.e., the tangential derivative of $h(x, y, t)$ along $y = 0, D$ is not constrained to 0. Therefore, we must modify our boundary condition to force h to be constant along $y = 0, D$, that is, to impose $v_1 = 0$ at each of these boundaries. We can accomplish this by using a *sponge layer*,

a technique used in a variety of atmospheric and oceanic models (see, e.g., [21]). A sponge layer is a region around a boundary in which velocities are artificially damped so that problematic or ill-posed boundary conditions may be satisfied. In our case, the sponge layer takes the form of two regions,

$$R_{0,sponge} = \{(x,y)|y \in [0,\delta], \delta > 0\},$$

and

$$R_{D,sponge} = \{(x,y)|y \in [D-\delta, D], \delta > 0\},$$

where the parameter δ controls the width of the sponge layer. In this layer, Ekman (i.e., linear) friction is increased via a large friction coefficient applied only on the regions $R_{0,sponge}$ and $R_{D,sponge}$. As the friction coefficient increases, the fluid in these two regions is artificially made more viscous. The viscosity in the regions can be raised sufficiently via the friction coefficient so that all velocities are damped; then all along the boundary regions $R_{0,sponge}$ and $R_{D,sponge}$, and thus all along the boundaries, the solution of $h(x,y,t)$ will 'settle' on a representative value for each boundary. This value is constant along each boundary at a given time step, but it can evolve through time.

Boundary Conditions for p

In determining the boundary condition for $p(x,y,t)$ on $y = 0, D$, we have some freedom. Equation (2.94) determines $p(x,y,t)$ only up to an additive constant. We are then free to choose the value of $p(x,y,t)$ somewhere on the domain. Because (2.99) implies that $p(x,y,t)$ is constant on $y = 0, D$, we can choose to set

$$p(x, D, t) = 0. \tag{2.104}$$

For the boundary $y = 0$, we impose a Neumann condition on $p(x,y,t)$,

$$\mathbf{n} \cdot \nabla p(x,y,t) = 0 \ \text{ on } \ y = 0. \tag{2.105}$$

This condition allows 'natural' values of $p(x,y,t)$ to evolve on the lower boundary; this is useful for calculating quantities (e.g., lower-layer transport) in the analysis of numerical simulations. Imposing (2.105) does not strictly enforce (2.99) for $p(x,y,t)$,

although the variation in $p(x, y, t)$ along the $y = 0$ boundary is small in numerical simulations.

Remaining Boundary Issues

We must choose between the two boundary implementation methods for $h(x, y, t)$, and we must also impose a boundary condition on $q(x, y, t)$. Boundary method I assigns a constant value along each of the boundaries $y = 0$ and $y = D$ via an integral average of nearby values. In deriving the shallow-water equations, the conservation of mass was a fundamental physical principle used. Indeed, for our reduced equations (2.90)–(2.94), it can be shown that mass is exactly conserved (see Section 4.2 for details). However, when using boundary method I, the representative boundary value arrived at via the integral average does not necessarily conserve mass. Instead, the boundary values of $h(x, y, t)$ that are imposed act as sources or sinks of mass. Although these mass changes are small at each time step, they accumulate over time and become significant over long-time integration. As the boundaries become more complex, this source/sink effect is heightened, and great mass changes can be seen. Through experimentation with the parameters defining the integral average regions R_0 and R_D, an attempt was made to try to minimize the mass drift. However, parameters were very sensitive to a host of factors, including τ_0, the geometry, and friction, and thus a given set of parameters minimizing mass change in one case did not necessarily minimize this change in another simulation. This property of mass drift is a violation of physical principles at the most fundamental level, and thus, we cannot use boundary method I for $h(x, y, t)$.

Boundary method II, however, does not artificially impose a value at the boundaries $y = 0, D$. Instead, through the high-viscosity sponge layer, the system itself determines an appropriate boundary value. This boundary method does allow for the conservation of mass, up to numerical error. This error arises because of the spatial discretization. The Ekman forcing function must integrate to 0 over the domain in order to conserve mass, but the use of a function which analytically integrates to 0 on the discretized domain can only approximate this zero-integration. The difference

accumulates at each time step, and leads to a small drift in mass. However, the relative mass drift is on the order of $1e^{-7}$ for our chosen resolution, whereas the relative mass drift using Boundary Method I can be on the order of 1; i.e., the change in mass can be as large as the initial total mass. This error predictably decreases as spatial resolution is increased. Although other issues arise from using these sponge layers (e.g., spikes in higher order derivatives near the δ-interfaces of $R_{0,sponge}$ and $R_{D,sponge}$) these issues do not invalidate the model.

For our model variable $q(x, y, t)$, we can determine its boundary condition according to its definition (2.94). We assume that

$$\nabla_H^2 p = 0$$

on the boundary, and thus, in a Dirichlet sense, we define q on the boundaries $y = 0, D$ to be

$$q = \mu h - \beta' y. \tag{2.106}$$

But here again we must determine a proper boundary value for $h(x, y, t)$. Using boundary method I to determine $h(x, y, t)$ in (2.106) does not affect conservation properties, and so it is used here. Thus we set

$$q(x, y, t) = \mu h_{avg,0} - \beta' y \quad \text{on} \quad y = 0,$$

and

$$q(x, y, t) = \mu h_{avg,D} - \beta' y \quad \text{on} \quad y = D.$$

2.3.2 Channel with Passage

The ACC flows around the earth largely uninhibited by land barriers. However, between the southern tip of South America and the Antarctic Peninsula lies a relatively narrow oceanic region called the Drake Passage (see Figure 2.10). In this region, the meridional spread of the ACC is constrained between the land barriers. In addition to providing a convenient station for measuring the transport of the ACC, the Drake Passage also influences the path of the flow. Because of these flow implications, we want to incorporate this geography into our model domain. The upper and lower
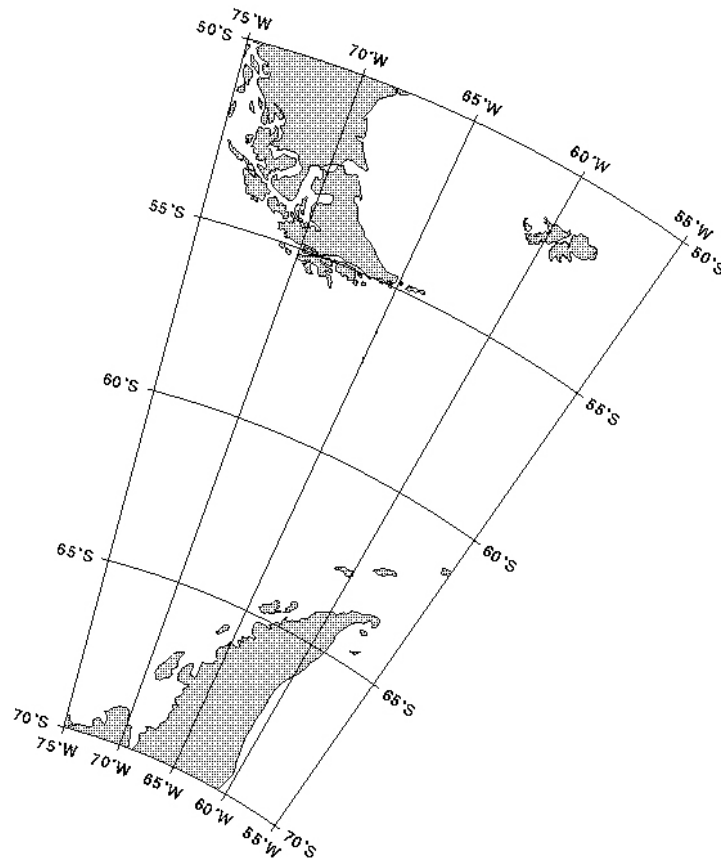
Figure 2.10: The Drake Passage (adapted from [8]).
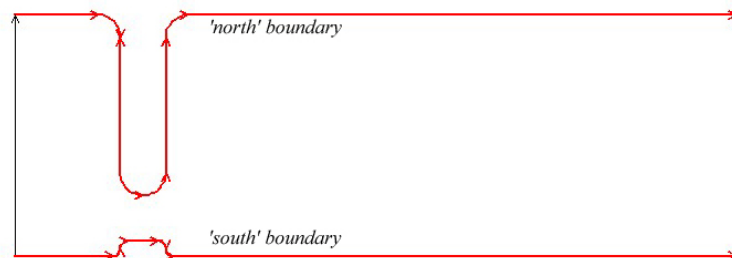
Figure 2.11: The model domain representing the ACC domain constrained by the Drake Passage.

boundaries of the simple channel are modified to include this constriction by drawing the two boundaries together on a small part of the domain (see Figure 2.11).

Although we have modified the boundaries of our domain, the conditions imposed remain largely the same. As in the simple channel, we impose the periodic conditions in x for both $h(x, y, t)$ and $p(x, y, t)$ (i.e., (2.95)). As in Section 2.3.1, this implies periodicity in $q(x, y, t)$ as well. The remaining boundaries are grouped as 'north' and 'south' as in Figure 2.11. This is done because the boundary conditions imposed are the same for all boundaries within the 'north' group. Similarly, the boundary conditions imposed are the same for all boundaries within the 'south' group. This designation simplifies our discussion. As in the simple channel, we impose no-flow conditions normal to the boundaries in both the upper and lower layers. Also, as in the simple channel, the ill-posedness of these conditions forces us to modify the conditions to imposing a spatially constant, but time-dependent boundary condition for $h(x, y, t)$ on the 'north' and 'south' boundaries. We impose the analogue of Boundary Method II for this domain by defining $R_{south,sponge}$ and $R_{north,sponge}$ to be suitable regions near the south and north boundaries respectively. Then in addition to the no-slip condition at the boundaries, the high viscosity along each boundary forces the solution to be constant along each boundary, and this imposes no-normal flow, as in the simple channel.

For $p(x, y, t)$ on the 'north' and 'south' boundaries, we apply the analysis from the simple channel, and thus impose $p(x, y, t) = 0$ along the 'north' boundary, and apply the analogue of (2.105) along the 'south' boundary,

$$\mathbf{n} \cdot \nabla p(x, y, t) = 0. \tag{2.107}$$

Again, we have not forced $p(x, y, t)$ to be constant along the 'south' boundary, but the variation along the boundary as a result of imposing (2.107) is small.

2.4 Initial Conditions and Time Integration

The evolution of the two-layer frontal geostrophic model can be likened to taking an unforced oceanic domain and 'turning on' the forcing, specifically the Ekman pumping

force caused by winds. The evolution has two distinct phases: the non-turbulent front-building interval and the turbulent phase. In the first phase, the Ekman pumping force acts upon the initially constant $h(x, y, t)$. This force creates a gradient, or front, in the solution of $h(x, y, t)$. The Ekman pumping force continually increases the magnitude of the gradient, until the buildup of potential energy in the front is released. This release occurs in the second phase. The gradient in $h(x, y, t)$ breaks into a turbulent profile, and the system eventually reaches a balance between the momentum imparted by the winds and the momentum dissipated by the turbulence and friction.

As the solution of $h(x, y, t)$ evolves and becomes turbulent, we want to analyze the 'steady state' solution that prevails as a result of the momentum balance. However, we do not seek a steady state in the typical sense of $h(x, y, t)$ and $p(x, y, t)$ remaining unchanged for all $t > T$ for some $T > 0$. Instead, we seek a steady state such that the time-averaged, zonally averaged profile of $h(x, y, t)$ and $p(x, y, t)$ over some time interval $T_b < t < T_c$ in the turbulent regime is unchanging (within some tolerance) compared to the same profile in a previous turbulent interval, $T_a < t < T_b$. We refer to this state as a *quasi-steady state*.

The model is evolved until a quasi-steady state is established in the solution of $h(x, y, t)$ and $p(x, y, t)$. The strength of the Ekman pumping force determines the length of time required for the first phase. The length of time of the second phase is determined by the time needed to establish steady state, and the desired amount of turbulent data needed to construct meaningful time-averages. In our model runs, we typically evolve our model to $t = 30000$ (corresponding to roughly 33 years), in which time the front is created, turbulence is established, and a quantitatively verifiable steady state is observed. For weak-forcing models and other models that take longer to establish a quasi-steady state, we evolve the model for longer, typically to $t = 60000$. In [33], in which similar experiments are performed, their model is evolved to 30 years.

Because the initial state of the model is a flat, unforced oceanic domain, both layers are flat; i.e., $h(x, y, t)$ is constant for all (x, y). Thus, we set $h(x, y, 0)$ to a constant value throughout the domain. Similarly, the pressure is initially constant throughout

the domain, and so we set $p(x, y, 0)$ equal to a constant (we choose $p(x, y, 0) = 0$ to satisfy boundary conditions). Because $q(x, y, t)$ is determined by the $h(x, y, t)$ and $p(x, y, t)$, we set

$$q(x, y, 0) = \nabla_H^2 p(x, y, 0) + \mu h(x, y, 0) - \beta y = \mu h(x, y, 0) - \beta y. \qquad (2.108)$$

Chapter 3

FEMLAB Implementation

3.1 Introduction

To numerically solve the model, we turn to the finite element method. The finite element method is a discretization method that easily allows for irregular domains. This is important in adapting our model to realistic domains. Because the flow of the ACC is affected by the presence of land barriers in the region of flow (e.g., the Drake Passage), representation of these land barriers is important for the validity of the model. We implement the model in the software package FEMLAB. FEMLAB is an interactive environment for solving a system of partial differential equations via the finite element method, and includes routines for spatial discretization (i.e., meshing), solving, and analysis of the solution. FEMLAB is most widely used for its application modes which contain predefined equations for a variety of physical phenomena, but the inclusion of general PDE forms allows the modelling of our FG model equations. In the following, we suppress arguments of variables, unless their inclusion aids clarity.

3.2 Solution of the Model Equations in FEMLAB

Adapting our model equations to the required FEMLAB input requires some manipulation. We use the time-dependent, general-form partial-differential-equation mode, which requires model equations in the form

$$d_a \frac{\partial u}{\partial t} + \nabla_H \cdot \mathbf{\Gamma} = F, \tag{3.1}$$

where d_a is the mass coefficient, and u is the model variable. From (2.92) and (2.93), it is clear that both $\mathbf{u}_{1,H}^{(1)}$ and $\mathbf{u}_{2,H}^{(0)}$ depend only on spatial derivatives of h and p. Thus, we can explicitly substitute for $\mathbf{u}_{1,H}^{(1)}$ and $\mathbf{u}_{2,H}^{(0)}$ in terms of h and p. This leaves us with 3 independent model variables, h, p, and q.

41

An additional restriction on solving our model equations with FEMLAB is that the $\mathbf{\Gamma}$ and F terms in (3.1) can contain only the dependent and independent variables and first partial derivatives. Thus, higher-order derivatives must be converted to lower order as a system of equations. To this end, we define a helper variable c as

$$c := \nabla_H^2 h, \tag{3.2}$$

which we can write in the form of (3.1) as

$$0 \frac{\partial c}{\partial t} + \nabla_H \cdot \begin{bmatrix} h_x \\ h_y \end{bmatrix} = c. \tag{3.3}$$

With the 4 model variables h, p, q, and c we transform our model equations (2.90)–(2.94) into a system of 4 equations of the form of (3.1).

We use this helper variable in writing equation (2.90) in an acceptable FEMLAB form. Though already in the form of (3.1), we must convert the second-order derivatives of h in $\mathbf{u}_{1,H}^{(1)}$ to first-order via c. In addition, we wish to do this conversion using as few extra variables (and thus, equations) as possible. The size of the linear system used in the solution of the model equations at each time step is directly related to the number of model variables, which motivates using a minimal number of extra variables. We can limit ourselves to just the one extra equation (3.3) by using the following identity:

$$-\nabla_H \cdot [hJ(\nabla_H h, h)] = \nabla_H \cdot \left(hc + \frac{h_x h_x + h_y h_y}{2} \begin{bmatrix} -h_y \\ h_x \end{bmatrix} \right). \tag{3.4}$$

We show this identity by expansion of the left- and right-hand sides of the equation. On the left, we have

$$-\nabla_H \cdot [hJ(\nabla_H h, h)] = -\nabla_H \cdot \left(h \begin{bmatrix} h_{xx} h_y + h_{xy} h_x \\ h_{yx} h_y + h_{yy} h_x \end{bmatrix} \right)$$

$$= -\nabla_H \cdot h \begin{bmatrix} h h_{xx} h_y + h h_{xy} h_x \\ h h_{yx} h_y + h h_{yy} h_x \end{bmatrix}$$

$$= -(h h_{xx} h_y)_x - (h h_{yx} h_y)_y + (h h_{xy} h_x)_x + (h h_{yy} h_x)_y$$

$$= -((h h_{xx})_x h_y + h h_{xx} h_{yx}) - ((h h_{yx})_y h_y + h h_{yx} h_{yy})$$

$$+ ((hh_{xy})_x h_x + hh_{xy} h_{xx}) + ((hh_{yy})_x h_x + hh_{yy} h_{xy})$$

$$= -h_x h_{xx} h_y - hh_{xxx} h_y - hh_x x h_y x - h_y h_{yx} h_y - hh_{yxy} h_y - hh_{yx} h_{yy}$$

$$+ h_x h_{xy} h_x + hh_{xyx} h_x + hh_{xy} h_{xx} + h_y h_{yy} h_x + hh_{yyy} h_x + hh_{yy} h_{xy}. \tag{3.5}$$

Assuming sufficient continuity in h, we can interchange the order of the partial derivatives, cancel terms, and simplify the left-hand side (3.5) to

$$-h_x h_{xx} h_y - hh_{xxx} h_y - h_y h_{yx} h_y - hh_{yxy} h_y + h_x h_{xy} h_x + hh_{xyx} h_x + h_y h_{yy} h_x + hh_{yyy} h_x. \tag{3.6}$$

We now expand the right-hand side of (3.4):

$$\nabla_H \cdot \left(hc + \frac{h_x h_x + h_y h_y}{2} \begin{bmatrix} -h_y \\ h_x \end{bmatrix} \right) = \nabla_H \cdot \begin{bmatrix} -hh_{xx} h_y - hh_{yy} h_y - \frac{h_x h_x}{2} h_y - \frac{h_y h_y}{2} h_y \\ -hh_{xx} h_x + hh_{yy} h_x + \frac{h_x h_x}{2} h_x + \frac{h_y h_y}{2} h_x \end{bmatrix}$$

$$= -h_x h_{xx} h_y - hh_{xxx} h_y - hh_{xx} h_{yx} - h_x h_{yy} h_y - hh_{yyx} h_y$$

$$- hh_{yy} h_{yx} - h_y h_x h_{xx} - h_y h_y h_{yx} - \frac{h_x h_x + h_y h_y}{2} h_{yx}$$

$$+ h_y h_{xx} h_x + hh_{xxy} h_x + hh_{xx} h_{yy} + h_y h_{yy} h_x + hh_{yyy} h_x$$

$$+ hh_{yy} h_{xy} + h_x h_x h_{xy} + h_x h_y h_{yy} + \frac{h_x h_x + h_y h_y}{2} h_{yx}. \tag{3.7}$$

Similarly, we can simplify the right-hand side (3.7) to

$$-hh_{xxx} h_y - hh_{yyx} h_y - h_y h_x h_{xx} - h -_y h_y h_{yx} + hh_{xxy} h_x + hh_x h_{yyy} + h_x h_x h_{xy} + hxh_y h_{yy}. \tag{3.8}$$

It is easily verified by inspection that (3.6) is equal to (3.8), and we have thus verified (3.4).

We now expand (2.90):

$$\frac{\partial h}{\partial t} + \nabla_H \cdot \left(h \left(-\hat{\mathbf{k}} \times \nabla_H p - J(\nabla_H h, h) + \nu_1' \nabla_H^2 \nabla_H h \right) \right) = -\tau_0 w_{1,e};$$

i.e.,

$$\frac{\partial h}{\partial t} + \nabla_H \cdot \begin{bmatrix} hp_y \\ -hp_x \end{bmatrix} - \nabla_H \cdot (hJ(\nabla_H h, h))$$

$$- \nabla_H \cdot \left(\nu_1' h \nabla_H^2 \nabla_H h \right) = -\tau_0 w_{1,e}.$$

Then, using (3.4) and (3.2), we get

$$\frac{\partial h}{\partial t} + \nabla_H \cdot \left(\begin{bmatrix} hp_y + \nu_1' hc_x \\ -hp_x + \nu_1' hc_y \end{bmatrix} + \left(hc + \frac{h_x h_x + h_y h_y}{2} \begin{bmatrix} -h_y \\ h_x \end{bmatrix} \right) \right) = -\tau_0 w_{1,e}. \quad (3.9)$$

Now (2.90) is written in the form of (3.1) using only the model variables and first partial derivatives in the $\mathbf{\Gamma}$ and F terms. We can input this equation into FEMLAB.

Now expanding (2.91)

$$\frac{\partial q}{\partial t} + \nabla_H \cdot \left(q \begin{bmatrix} p_y \\ -p_x \end{bmatrix} \right) = \mu \tau_0 w_{2,e} - r_2' \nabla_H^2 p + \nu_2' \nabla_H^4 p$$

we rewrite it in the form of (3.1) as

$$\frac{\partial q}{\partial t} + \nabla_H \cdot \left(q \begin{bmatrix} p_y \\ -p_x \end{bmatrix} + r_2' \begin{bmatrix} p_x \\ p_y \end{bmatrix} \right) = \mu \tau_0 w_{2,e} + \nu_2' \nabla_H^4 p. \quad (3.10)$$

To eliminate the high-order derivatives in the friction term

$$\nu_2' \nabla_H^4 p,$$

we rewrite in terms of q. First, we expand

$$\begin{aligned} \nabla_H^2 q &= \nabla_H^2 (\nabla_H^2 p + \mu h - \beta' y) \\ &= \nabla_H^4 p + \mu \nabla_H^2 h. \end{aligned} \quad (3.11)$$

Thus,

$$\nu_2' \nabla_H^4 p = \nu_2' \left(\nabla_H^2 q - \mu \nabla_H^2 h \right). \quad (3.12)$$

We can use (3.12) to rewrite (3.10) as

$$\frac{\partial q}{\partial t} + \nabla_H \cdot \left(q \begin{bmatrix} p_y \\ -p_x \end{bmatrix} + r_2' \begin{bmatrix} p_x \\ p_y \end{bmatrix} - \nu_2' \begin{bmatrix} q_x \\ q_y \end{bmatrix} + \nu_2' \mu \begin{bmatrix} h_x \\ h_y \end{bmatrix} \right) = \mu \tau_0 w_{2,e}. \quad (3.13)$$

Now (3.13) is also expressed in the form of (3.1), using only the model variables and first partial derivatives in the $\mathbf{\Gamma}$ and F terms.

We now rewrite the expression $q = \nabla_H^2 p + \mu h - \beta' y$ in the form of (3.1):

$$0\frac{\partial q}{\partial t} + \nabla_H \cdot \begin{bmatrix} p_x \\ p_y \end{bmatrix} = q - \mu h + \beta' y. \tag{3.14}$$

Combining (3.3), (3.9), (3.13), and (3.14), we have our model equations as a system of 4 PDEs in the required form (3.1):

$$\frac{\partial h}{\partial t} + \nabla_H \cdot \left(\begin{bmatrix} hp_y + \nu_1' c_x \\ -hp_x + \nu_1' c_y \end{bmatrix} + \left(hc + \frac{h_x h_x + h_y h_y}{2} \begin{bmatrix} -h_y \\ h_x \end{bmatrix} \right) \right) = -\tau_0 w_{1,e}, \tag{3.15}$$

$$\frac{\partial q}{\partial t} + \nabla_H \cdot \left(q \begin{bmatrix} p_y \\ -p_x \end{bmatrix} + r_2' \begin{bmatrix} p_x \\ p_y \end{bmatrix} - \nu_2' \begin{bmatrix} q_x \\ q_y \end{bmatrix} + \nu_2' \mu \begin{bmatrix} h_x \\ h_y \end{bmatrix} \right) = \mu \tau_0 w_{2,e}, \tag{3.16}$$

$$0\frac{\partial q}{\partial t} + \nabla_H \cdot \begin{bmatrix} p_x \\ p_y \end{bmatrix} = q - \mu h + \beta' y, \tag{3.17}$$

$$0\frac{\partial c}{\partial t} + \nabla_H \cdot \begin{bmatrix} h_x \\ h_y \end{bmatrix} = c. \tag{3.18}$$

3.3   Parameters

After implementing the model equations in the FEMLAB environment, we specify parameter values for our model. Model parameters will fall into two categories: fixed parameters, which remain constant throughout all experiments, and variable parameters, which vary in a range of values in our experiments.

We base our numerical experiments on the work of Tansley and Marshall [33], wherein numerical experiments were conducted using a balanced *geostrophic vorticity* model. Like the equations of the frontal geostrophic model, the geostrophic vorticity equations are asymptotic reductions of the shallow-water equations [33]. Because we are basing our experiments on [33], we derive our parameter values from there. The geostrophic vorticity model is *dimensional*; i.e., it has not been non-dimensionalized. Therefore, we non-dimensionalize the parameter values in [33] following Section 2.2. However, in our determination of the non-dimensional horizontal turbulent viscosity

Table 3.1: Dimensional model parameters from [33]

parameter	symbol	value
Longitudinal extent	$3L_H$	5760 km
Latitudinal extent	L_H	1920 km
Upper-layer height scale	H_1	1200 m
Total Depth	H	4000 m
Coriolis parameter	f_0	-1.3×10^{-4} s^{-1}
Beta parameter	β_0	1.5×10^{-11} m^{-1}s^{-1}
Surface wind-stress	$\hat{\tau}_0$	0.01 - 0.25 Nm^{-2}
Reduced gravity	g'	0.02 ms^{-2}
Reference density	ρ_0	1035 kg m^{-3}
Bottom linear friction coefficient	R_2	1×10^{-7} s^{-1}

friction parameters, ν_1' and ν_2', we cannot use the parameter values in [33], because the geostrophic vorticity model does not include this type of friction. The geostrophic vorticity model instead uses a higher-order friction called *hyperviscosity*. To obtain a value for ν_1' and ν_2', these parameter spaces were explored. From (2.66), we can deduce that

$$\nu_2' = \frac{1}{\epsilon}\nu_1',$$

and thus, we need only explore one parameter space. With $\nu_1' = 0$, the solver is prematurely halted due to a failure in convergence of the modified Newton iteration (see Section 4.6 for details of the solver), caused by the growth of small-scale noise. A relatively large value of ν_1' can affect the balances established (see Chapter 4). We choose a value of $\nu_1' = 1.93$e-3, which implies a value of $\nu_2' = 3.86$e-3. This choice corresponds to a dimensional horizontal turbulent viscosity of 400 m^2s^{-1}, considerably smaller than 2000 m^2s^{-1} used in [4] for a three-dimensional primitive equation model of the ACC, but in the (fairly wide) range of 10^2 m^{2}s^{-1} to 10^4 m^{2}s^{-1} given in [17]. The chosen value for ν_1' adequately smooths the solution via damping of high-order derivatives, while leaving the established layer balances largely unaffected. Table 3.1 shows the dimensional model parameters used in [33].

We calculate the value of the *eddy Rossby number* using (2.57) along with the

parameter values from Table 3.1:

$$\epsilon = \frac{g'H_1}{(|f_0|L_{eddy})^2} = 0.50, \qquad (3.19)$$

where $L_{eddy} = 60$km is a characteristic eddy length scale. Geostrophy requires $\epsilon \ll 1$; here ϵ is small enough to imply geostrophy [12], though this value lies in the limits of applicability.

There is some difference in implementation of the forcing term between the geostrophic vorticity model and our model. The former uses a surface wind stress given by

$$\tau_s = \hat{\tau}_0 \cos\left(\frac{\pi y}{L}\right), \quad -\frac{L}{2} \le y \le \frac{L}{2}. \qquad (3.20)$$

The Ekman pumping force used in our model implementation is given by the non-dimensionalized curl of the wind stress [12]:

$$\tau_0 w_e = \nabla_H \times \frac{\tau_s}{|f_0|\rho_0} = \frac{d}{dy}\frac{\tau_s}{|f_0|\rho_0} = \frac{\hat{\tau}_0 \pi}{\rho_0 |f_0| L}\sin(\frac{\pi y}{L}), \quad -\frac{L}{2} \le y \le \frac{L}{2}.$$

Additionally, we model over the latitudinal domain $y = [0, D]$, where D is the non-dimensionalized analogue of L, and so we translate the forcing term into our domain, obtaining

$$\tau_0 w_e = \frac{\hat{\tau}_0 \pi}{\rho_0 |f_0| L} \cos\left(\frac{\pi y}{D}\right), \quad 0 \le y \le D. \qquad (3.21)$$

Then from (3.21) we can obtain the coefficient of the Ekman pumping force, τ_0, as

$$\tau_0 = \frac{\hat{\tau}_0 \pi}{\rho_0 |f_0| L}.$$

From Table 3.1, $\hat{\tau}_0$ ranges from $0.01 - 0.25$ Nm^{-2}; the corresponding range for τ_0 is $3.961 \times 10^{-6} - 9.905 \times 10^{-5}$. Next, we calculate β', the nondimensional analogue of β_0, as

$$\beta' = \frac{\beta_0}{|f_0|L\epsilon^2} = 0.03.$$

We also calculate μ from (2.62) and (2.63):

$$\mu = \frac{H_1/H}{\epsilon^2} = 1.21.$$

Next, we calculate our non-dimensional frictional parameters. However, we deviate somewhat from the values given in Table 3.1. The value of R_2 in [33] is given for

Table 3.2: Non-dimensional model parameters

Non-dimensional parameter	symbol	value
Longitudinal extent	$3D$	96
Latitudinal extent	D	32
Beta parameter	β'	0.03
Relative layer depth parameter	μ	1.21
Surface wind-stress	τ_0	$3.961 \times 10^{-6} - 9.905 \times 10^{-5}$
Bottom linear friction coefficient	r_2	0.04
Upper-layer horizontal turbulent viscosity	ν_1	1.93×10^{-3}
Lower-layer horizontal turbulent viscosity	ν_2	3.86×10^{-3}

a typical channel with bottom topography. However, without the dissipative role of bottom topography, artificially large transports occur that are an order of magnitude larger; these transports do not interest us. In our simple channel without bottom topography, we increase the amount of bottom friction to compensate for the artificially smooth bottom. We thus use a dimensional bottom friction coefficient of

$$R_2 = 1.0 \times 10^{-6} \text{s}^{-1}.$$

We proceed to calculate the non-dimensional friction parameters:

$$r_2 = \frac{R_2/|f_0|}{\epsilon^2} = 0.04,$$

$$\nu_1 = \frac{A_h/L^2|f_0|}{\epsilon} = 1.93 \times 10^{-3}, \quad \nu_2 = \frac{A_h/L^2|f_0|}{\epsilon^2} = 3.86 \times 10^{-3}.$$

We also obtain our domain parameter, $D = L/L_{eddy} = 32$. We summarize our non-dimensional model parameters in Table 3.2.

3.4   Domain and Bottom Topography

We have thus far avoided any mention of the bottom topography of the ocean, except for a short justification of altering the bottom linear friction coefficient. Indeed the ocean bottom in the region of the ACC contains a widely varying topography that has profound effects on the nature and course of the flow of the ACC. Fortunately,

the inclusion of bottom topography in our model is fairly simple. Because we are modelling in a two-dimensional regime, we do not alter our domain. Instead, we rewrite (2.67) as

$$h_2 := 1 - \mu\epsilon^2 h_1 - \mu_B\epsilon^2 h_B(x, y),$$

where μ_B is a bottom topography parameter, and $h_B(x, y)$ is a function which describes the topography of the ocean bottom. When this additional term is carried through the derivation, it results only in a modification of equation (2.94) defining q, to

$$q = \nabla_H^2 p + \mu h + \mu_B h_B(x, y) - \beta' y.$$

We can easily modify the FEMLAB implementation of this equation accordingly by replacing the right-hand side of (3.17) with

$$q - \mu h - \mu_B h_B(x, y) + \beta' y.$$

For simulations without bottom topography, we set $\mu_B = 0$. The variations of domain and topography provide the basis for our experiments with the model, following the experiments of [33].

3.4.1   Simple Channel

Our simplest experiment involves a latitudinally re-entrant (i.e., periodic in x), flat-bottom (i.e., $h_B(x, y) = 0$) rectangular domain, $\Omega = \{[0, 3D] \times [0, D]\} = \{[0, 96] \times [0, 32]\}$. See Figure 3.1.a.

3.4.2   Simple Channel with Topographic Ridge

We modify our simple channel to include a simple ridge in the bottom topography. We thus define

$$h_B(x, y) = \exp\left(-\left(\frac{x - 17}{3}\right)^2\right), \tag{3.22}$$

i.e., $h_B(x, y)$ defines a ridge of maximal height 1, centered at $x = 17$, and independent of y. We retain the domain of the simple channel run; i.e., $\Omega = \{[0, 3D] \times [0, D]\} = \{[0, 96] \times [0, 32]\}$. See Figure 3.1.b.
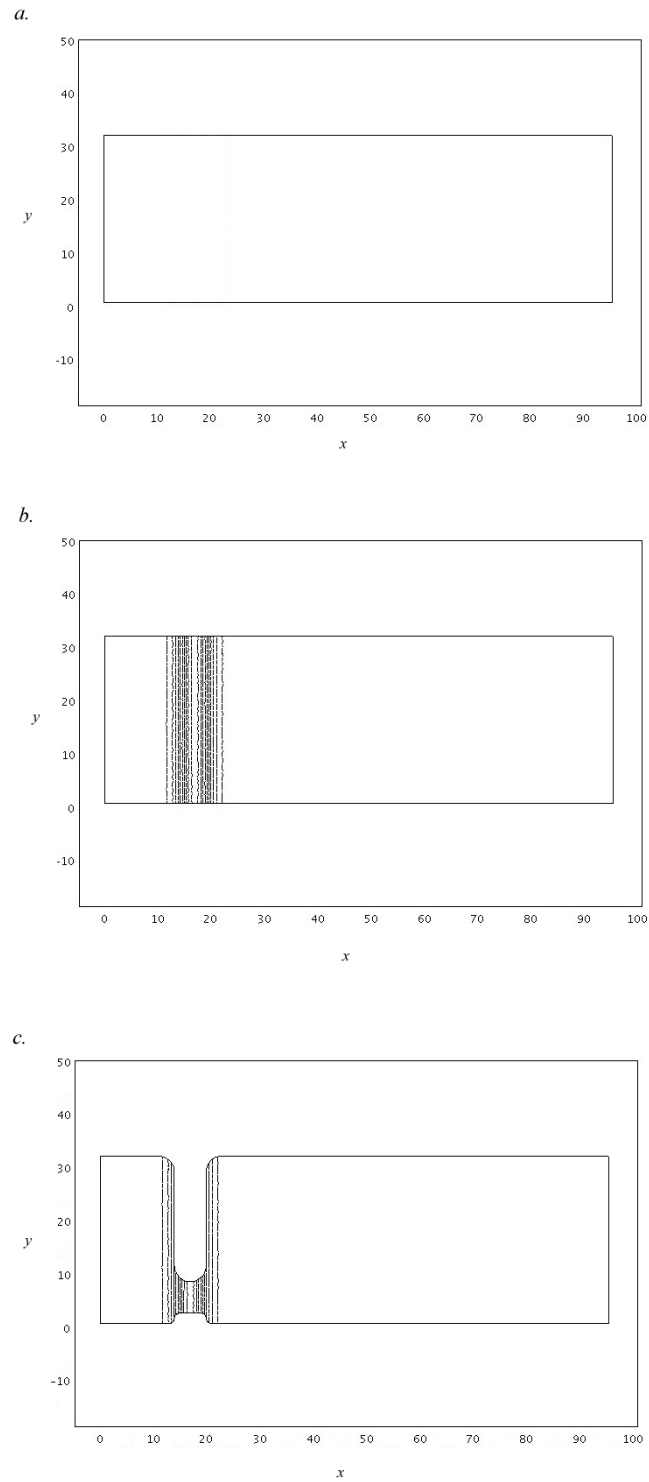
Figure 3.1: *a*: Simple channel domain. *b*: Simple channel domain with contoured topographic ridge. *c*. Channel with passage domain and contoured topographic ridge. These experiments are based on [33].

3.4.3   Channel with Passage and Topographic Ridge

We further modify our simple channel to include a passage as described in Section 2.3.2. We begin with the simple channel geometry, using a base domain of $\Omega = \{[0, 3D] \times [0, D]\} = \{[0, 96] \times [0, 32]\}$. Following [33], two rectangular regions of width 6 centered at $x = 17$ are subtracted from this domain, leaving a restricted passage for the flow centered approximately at $D/4$. However, the construction of the domain using rectangles leads to sharp corners, or *singularities* [1] in the modelling domain. Singularities can cause errors in meshing and in the solution; however they can be avoided by *filleting* [1] any singularities in the modelling geometry. Filleting is a process by which sharp corners are rounded by a given radius. In our geometry, the passage created by subtracting the two rectangular domains is filleted at the corners, rounding the land barriers. This is not unphysical; the use of rectangular sections to construct our original domain is idealized. Indeed, rounded land barriers are more in keeping with observed coastlines. The bottom topography in (3.22) is included. Taken together, the topography and ridge geometry are a simplification of the topography of the Drake Passage, as illustrated in Figure 3.2. See Figure 3.1.c. for the idealized domain.

3.5   Implementation of Boundary Conditions, Initial Conditions

FEMLAB implements boundary conditions via the system of equations

$$-\mathbf{n} \cdot \Gamma_i = G_i + \Sigma_{j=1}^{n} \frac{\partial R_j}{\partial \upsilon_i} \alpha_j, \quad i = 1 \ldots n, \tag{3.23}$$

$$R_i = 0, \quad i = 1 \ldots n, \tag{3.24}$$

where $\mathbf{n}$ is the outward unit normal vector, Γ_i is the ith component of $\mathbf{\Gamma}$ from (3.1), G_i and R_i are fields specified by the user, α_j is a *Lagrange multiplier* [1], υ_i is the ith model variable, and n is the number of model variables. Additionally, the user specifies the boundary as either Neumann or Dirichlet. The combination of this specification and the system (3.23)–(3.24) allows for 3 boundary definition possibilities. First, when specifying a boundary as Neumann, FEMLAB imposes

$$R_i = 0, \quad i = 1 \ldots n,$$
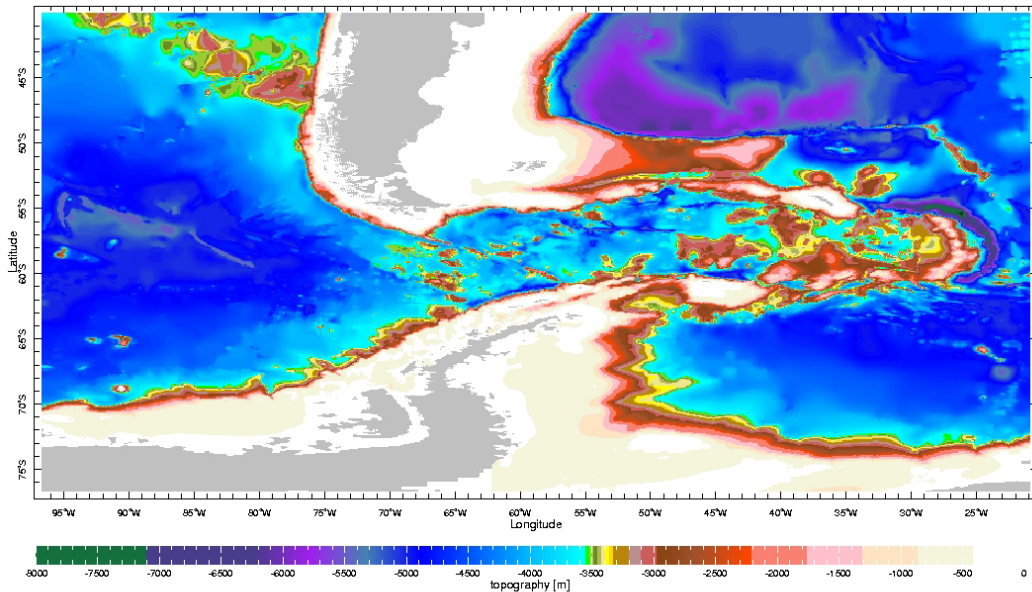
Figure 3.2: The topography of the Drake Passage, from WORLDBATH:ETOPO5 U.S. Navy data. The bottom topography through the Drake Passage is much higher than the surrounding ocean, which motivates our topographic ridge in the geometry of Figure 3.1.c.

and (3.24) reduces to

$$-\mathbf{n} \cdot \Gamma_i = G_i, \quad i = 1 \ldots n.$$

Alternatively, by specifying a boundary as Dirichlet but having non-zero entries for G_i for all $i = 1 \ldots n$, the Lagrange multipliers are chosen so as to render (3.23) redundant; i.e., the left-hand side of (3.23) is made equal to the right-hand side, such that nothing is imposed. This redundnacy leaves just the condition (3.24). Lastly, one can impose a combination of Dirichlet and Neumann conditions on a boundary by specifying the boundary as Dirichlet, but setting some (but not all) entries of R_i equal to 0. For illustration, we consider the boundary conditions for our model variables on the $y = 0$ (or, equivalently, 'south') boundary.

Specifying the boundary as Dirichlet, both (3.23) and (3.24) apply. We set

$$\mathbf{R} = \begin{bmatrix} 0 \\ q - \mu h_{avg,0} - \mu_B h_B + \beta' y \\ 0 \\ 0 \end{bmatrix},$$

where $\mathbf{R} = [R_1 \ R_2 \ R_3 \ R_4]^T$, and $h_{avg,0}$ is given by (2.101). We also set

$$\mathbf{G} = \begin{bmatrix} 0 \\ 0 \\ 0 \\ 0 \end{bmatrix},$$

where $\mathbf{G} = [G_1 \ G_2 \ G_3 \ G_4]^T$. Additionally, define the vector of dependent variables by $\mathbf{\Upsilon} = [v_1 \ v_2 \ v_3 \ v_4]^T = [h \ q \ p \ c]^T$. With these definitions, (3.23) gives the system of equations

$$-\mathbf{n} \cdot \Gamma_1 = 0, \tag{3.25}$$

$$-\mathbf{n} \cdot \Gamma_2 = \alpha_2, \tag{3.26}$$

$$-\mathbf{n} \cdot \Gamma_3 = 0, \tag{3.27}$$

$$-\mathbf{n} \cdot \Gamma_4 = 0. \tag{3.28}$$

Now (3.26) is solved for the Lagrange multiplier α_2 so as to render the equation redundant. (3.27) and (3.28) are obtained by noting that all of the derivative terms in the summation in (3.23) vanish, and we are left with two homogeneous Neumann conditions. From (3.17) and (3.18), we deduce that

$$\Gamma_3 = \begin{bmatrix} p_x \\ p_y \end{bmatrix},$$

and

$$\Gamma_4 = \begin{bmatrix} h_x \\ h_y \end{bmatrix},$$

which implies that (3.27) and (3.28) give the Neumann conditions

$$-\mathbf{n} \cdot \nabla_H p = 0,$$

Table 3.3: Boundary Condition Implementation

boundary	i	G_i	R_i	Resultant Boundary Condition
$y = 0$, 'south'	1	0	0	$-\mathbf{n} \cdot \nabla_H \left(h\mathbf{u}_{1,H} \right) = 0$
	2	0	$q - \mu h_{avg,0} - \mu_B h_B + \beta' y$	$q = \mu h_{avg,0} + \mu_B h_B - \beta' y$
	3	0	0	$-\mathbf{n} \cdot \nabla_H p = 0$
	4	0	0	$-\mathbf{n} \cdot \nabla_H h = 0$
$y = D$, 'north'	1	0	0	$-\mathbf{n} \cdot \nabla_H \left(h\mathbf{u}_{1,H} \right) = 0$
	2	0	$q - \mu h_{avg,D} - \mu_B h_B + \beta' y$	$q = \mu h_{avg,D} + \mu_B h_B - \beta' y$
	3	0	p	$p = 0$
	4	0	0	$-\mathbf{n} \cdot \nabla_H h = 0$

$$-\mathbf{n} \cdot \nabla_H h = 0.$$

In this sense, boundaries can contain both Dirichlet and Neumann conditions. There is a separate procedure for defining periodic boundaries; these are implemented as *extrusion coupling variables* [1]. An extrusion coupling variable is defined by a non-local expression in a source domain that is mapped to a destination domain while maintaining some orientation. The implementation is straightforward in the FEM-LAB GUI. We summarize our implementation of the boundary conditions discussed in Section 2.3 in Table 3.3. We include both the simple channel domain and the passage domain in the same table because the boundary conditions are identical except for the shape of the boundary.

Initial conditions must be specified for all model variables in FEMLAB. As we have non-dimensionalized $h(x, y, t)$ with respect to a characteristic upper-layer depth, we set $h(x, y, 0) = 1$. Next, we set $p(x, y, 0) = 0$, which we note is consistent with the boundary conditions imposed upon $p(x, y, t)$. We set $c(x, y, 0) = 0$ because all spatial derivatives of $h(x, y, 0)$ are initially 0. Lastly, using (3.4) in (2.108), the initial condition $q(x, y, 0)$ is determined in terms of $p(x, y, 0)$ and $h(x, y, 0)$; i.e.,

$$q(x, y, 0) = \nabla_H^2 p(x, y, 0) + \mu h(x, y, 0) + \mu_B h_B(x, y) - \beta' y = \mu + \mu_B h_B(x, y) - \beta' y.$$

Chapter 4

Results

4.1 Introduction

Numerical simulations of our FEMLAB model were performed to correspond to the various domain and bottom topography cases - namely, the simple channel, the simple channel with bottom topography, the channel with a passage, and the channel with a passage and bottom topography. In addition to examining the effects of domain and topography, we explore a number of parameter spaces. The relatively short computational times needed to perform a full simulation allow this parameter investigation; this investigation is not feasible with the more complex, higher-resolution models (e.g., OCCAM [35]), or with models using the full shallow-water equations (e.g., HIM [9]). In addition to the parameter investigations that are described here, a number of parameter values in the model were obtained by systematically experimenting with a range of values and choosing the optimal one. This process was primarily used in determining the boundary parameters, specifically the width of the sponge layer, the sponge layer linear friction coefficient, and the region width corresponding to boundary method I (see Section 2.3.1). These values were chosen so as to have minimal impact on the nature of the solution while still achieving the intended purpose of obtaining well-posed and physical boundary conditions.

Included in this section is an investigation of the effects of wind forcing on the characteristics of the flow. We study the effects (primarily on the transport of the flow) of changing the strength of winds via the parameter τ_0 and also the effects of varying the structure of the wind. In the latter, we study both balanced and unbalanced winds (having zero and non-zero integrals over the domain, respectively) that have important effects on conserved quantities. Because our model represents wind forcing by the resultant Ekman pumping forcing, variations in wind are manifested in variations in the Ekman pumping forcing. We also study the effects of varying

initial upper-layer depth. In using relatively shallow initial upper-layer depths, our model allows for the study of outcroppings, that is, locations where the upper layer vanishes, and the lower layer outcrops; i.e., the lower layer reaches the surface. This is an advantage that our model has over other similar models of the ACC (e.g., quasi-geostrophic models (e.g., [37]) and semi-geostrophic models (e.g., [32])) that do not permit outcroppings and consequently either use relatively deep upper layers, or artificially maintain a thin upper layer.

In this section, we also discuss a number of numerical issues involved with the model. These include an investigation of the effects on the model of varying the timestepping parameters; this has implications in various physical quantities associated with the model. As well, we discuss the effects of mesh resolution.

In the model simulations, we are concerned with the momentum balance that occurs between the wind forcing and dissipation via turbulence, as described in Chapter 2. This balance is discussed in the context of our model results.

4.2 Physical Quantities of the Model

The two-layer FG model is derived from the two-layer shallow-water equations. These equations are based on two fundamental physical principles for fluid flow: the conservation of mass and the conservation of momentum. These quantities are conserved locally, however; in this section we concern ourselves with quantities that are globally conserved. Naturally, these globally conserved quantities are related to the locally conserved quantities.

The non-dimensional mass of the fluid in our model is given by

$$M_{nd} = \iint_\Omega h\rho_1 + (1 - \mu\epsilon^2 h)\rho_2 \, dxdy, \tag{4.1}$$

where Ω is the non-dimensional model domain. Because $\rho_1, \rho_2, \mu,$ and ϵ are all constants, M_{nd} is a linear function of the quantity

$$M = \iint_\Omega h \, dxdy, \tag{4.2}$$

and thus we use this quantity as representative of the mass of the fluid in our model.

Consider the time variation of M,

$$\frac{\partial}{\partial t} \iint_\Omega h \, dx dy,$$

which we can write as

$$\iint_\Omega \frac{\partial h}{\partial t} \, dx dy. \tag{4.3}$$

Using equation (2.90), we rewrite (4.3) as

$$\iint_\Omega \tau_0 w_{1,e} dx dy - \iint_\Omega \nabla_H \cdot \left(h \mathbf{u}_{1,H}^{(1)} \right) dx dy. \tag{4.4}$$

Writing

$$\iint_\Omega \nabla_H \cdot \left(h \mathbf{u}_{1,H}^{(1)} \right) dx dy \tag{4.5}$$

from (4.4) as

$$\iint_\Omega \left(h u_{1,H}^{(1)} \right)_x dx dy + \iint_\Omega \left(h v_{1,H}^{(1)} \right)_y dx dy, \tag{4.6}$$

where $u_{1,H}^{(1)}$ and $v_{1,H}^{(1)}$ are the components of $\mathbf{u}_{1,H}^{(1)}$, we can further simplify by noting that

$$
\begin{aligned}
\iint_\Omega \left(h u_{1,H}^{(1)} \right)_x dx dy &= \int_{y=0}^{y=D} \left(h u_{1,H}^{(1)} \right) \Big|_{x=x_L}^{x=x_R} dy \\
&= \int_{y=0}^{y=D} 0 \, dy \\
&= 0,
\end{aligned}
$$

by the periodicity of h.

Additionally, we exchange the order of integration on

$$\iint_\Omega \left(h v_{1,H}^{(1)} \right)_y dx dy$$

from (4.6), which we can then write as

$$
\begin{aligned}
\int_{x=x_L}^{x=x_R} \left(h v_{1,H}^{(1)} \right) \Big|_{y=0}^{y=D} dx &= \int_{x=x_L}^{x=x_R} 0 \, dx \\
&= 0,
\end{aligned}
$$

where we have used that

$$v_{1,H}^{(1)} = 0 \quad \text{on} \quad y = 0, D,$$

due to the imposition of no-normal flow at the boundaries. Then we have that (4.5) vanishes, and therefore, from (4.3) and (4.4),

$$\iint_\Omega \frac{\partial h}{\partial t}\, dxdy = \iint_\Omega \tau_0 w_{1,e} dxdy. \tag{4.7}$$

If we apply an Ekman forcing function $w_{1,e}$ to the upper layer such that

$$\iint_\Omega w_{1,e} dxdy = 0, \tag{4.8}$$

we have from (4.7) that

$$\frac{\partial}{\partial t} \iint_\Omega h\, dxdy = 0; \tag{4.9}$$

i.e., that mass is invariant through time. We denote an Ekman forcing function satisfying (4.8) as *balanced*. Accordingly, if

$$\iint_\Omega w_{1,e} dxdy \neq 0,$$

we denote the Ekman forcing function as *unbalanced*.

There are a number of quantities that remain invariant under the evolution of the two-layer shallow-water equations (2.68)–(2.71) in the absence of Ekman forcing, (i.e., $\tau_0 = 0$). Our model loses this exact conservation in two ways; first by neglecting higher-order terms in the derivation of the FG model equations, and second, by using Ekman forcing terms. Unforced models (e.g., [28], [29]) prescribe an initial gradient in $h(x,y,t)$ with sufficient magnitude such that turbulence develops, whereas the implementation in this thesis prescribes an initially constant upper-layer depth, with the gradient in $h(x,y,t)$ growing through time as a result of the forcing.

The first such quantity we consider is the *total energy*. The total energy for the unforced two-layer shallow-water equations is given by

$$E_{sw} = \frac{1}{2} \iint_\Omega \left(g' h_1^2 + h_1 \mathbf{u}_{1,H} \cdot \mathbf{u}_{1,H} + h_2 \mathbf{u}_{2,H} \cdot \mathbf{u}_{2,H} \right) dxdy, \tag{4.10}$$

where all variables are as in (2.68)–(2.71) [11]. The first term in (4.10) represents the potential energy, while the second and third terms represent the kinetic energy in the upper and lower layer, respectively. We replace $\mathbf{u}_{1,H}$ and $\mathbf{u}_{2,H}$ by their leading-order terms, and according to the convention of Chapter 2, we let $h(x,y,t) := h_1(x,y,t)$. We then approximate the lower-layer (non-dimensional) height using (2.67) as

$$h_2(x,y,t) = 1 - \mu\epsilon^2 h(x,y,t) \approx 1.$$

After an appropriate scaling, the FG analogue of (4.10) becomes

$$\iint_{\Omega} \left(h^2 + \epsilon h \left(h_x^2 + h_y^2 \right) + \epsilon \left(p_x^2 + p_y^2 \right) \right) dxdy.$$

We then define the *non-dimensional FG potential energy* as

$$\iint_{\Omega} h^2 dxdy \tag{4.11}$$

and the *non-dimensional kinetic energy* as

$$\iint_{\Omega} \left(\epsilon h \left(h_x^2 + h_y^2 \right) + \left(p_x^2 + p_y^2 \right) \right) dxdy. \tag{4.12}$$

In the unforced FG model equations, the quantity in (4.11) is exactly conserved. In our forced FG model implementation however, potential energy is not conserved; it changes as a result of forcing and turbulence. Kinetic energy (4.12) is not conserved in either the forced or unforced FG model, although it is a useful quantity for discussing the evolution of the solution.

Next, we consider the lower-layer momentum. The *two-layer zonal momentum invariant* for the two-layer unforced shallow-water equations is given by

$$N_{sw} = \iint_{\Omega} h_1 u_1 + (H - h)u_2 - H \left(f_0 y + \frac{1}{2} \beta y^2 \right),$$

where all variables are as in (2.68)–(2.71) [11]. A similar process of leading-order approximations and appropriate scaling yields the non-dimensional FG lower-layer momentum

$$N = \iint_{\Omega} y \nabla_H^2 p \, dxdy \tag{4.13}$$

(see [11] for details). In the unforced FG model equations, (4.13) is exactly conserved; the presence of forcing in our implementation destroys this conservation property.

In addition to facilitating a discussion of the evolution of the solution, the unconserved quantities associated with the model (potential energy, kinetic energy, momentum) provide an indication of the establishment of a quasi-steady state. These quantities (and indeed, any physical measure based on the model variables) will oscillate about a mean constant value at the quasi-steady state.

4.3   The Meridional Balance of the ACC

As discussed in Chapter 2, a process of meridional overturning occurs in the ACC that is called the Deacon cell. This process of overturning maintains the isopycnal slope and thus maintains the leading-order velocities. In this section, we examine this balance more closely. Because the flow in which we are interested is turbulent, we are concerned with mean quantities, both in time and in the x-direction, to quantify the properties of the model. We introduce a number of definitions for evaluating our system in a mean sense. We use the quantity $h(x, y, t)$ for our definitions, although they are applicable to all quantities in our model.

We define a *zonal average* of a quantity $h(x, y, t)$ as

$$\overline{h(y, t)} = \frac{1}{x_R - x_L} \int_{x_L}^{x_R} h(x, y, t) dx,$$

where x_L and x_R are the x domain limits. With this definition, we can decompose a model variable, h, into its mean and zonally varying components as

$$h(x, y, t) = \overline{h(y, t)} + h'(x, y, t).$$

It is clear that the zonal average of the non-averaged term is zero; i.e.,

$$\overline{h'(y, t)} = 0. \tag{4.14}$$

In addition to zonally averaging, we also average quantities in time. Because we are investigating the turbulent quasi-steady state that occurs in the time evolution of our system, averaging in time eliminates the local effects of the turbulence and facilitates an analysis on a true steady state from our time-dependent quasi-steady state. We do not alter our notation to denote the time-mean, but instead henceforth assume that all quantities are time-averaged unless otherwise denoted. The time-averages are calculated over a period in which the system has reached a quasi-steady state. As a result of this time-averaging, we let

$$\frac{\partial \overline{h}}{\partial t} = 0, \quad \frac{\partial \overline{p}}{\partial t} = 0, \quad \frac{\partial \overline{q}}{\partial t} = 0. \tag{4.15}$$

We now return to our frontal geostrophic equations, (2.90)–(2.91), and formulate the time-averaged, zonally averaged analogues. Applying (4.15) to (2.90)–(2.91) and

dropping arguments gives

$$\nabla_H \cdot \left(\overline{h\mathbf{u}_{1,H}^{(1)}} \right) = -\tau_0 \overline{w_{1,e}}, \tag{4.16}$$

and

$$\nabla_H \cdot \left(\overline{q\mathbf{u}_{2,H}^{(0)}} \right) = \mu\tau_0 \overline{w_{2,e}} - r_2' \nabla_H^2 \overline{p} + \nu_2' \nabla_H^4 \overline{p}. \tag{4.17}$$

Considering (4.16), we replace all variables by their (zonal) mean and varying components; i.e.,

$$\nabla_H \cdot \left(\overline{\left(\overline{h} + h' \right) \left(\overline{\mathbf{u}_{1,H}^{(1)}} + \mathbf{u}_{1,H}^{(1)'} \right)} \right) = -\tau_0 \overline{w_{1,e}}. \tag{4.18}$$

Noting that x-derivatives vanish, we have that

$$\frac{\partial}{\partial y} \left(\overline{\left(\overline{h} + h' \right) \left(\overline{v_{1,H}^{(1)}} + v_{1,H}^{(1)'} \right)} \right) = -\tau_0 \overline{w_{1,e}}, \tag{4.19}$$

where $v_{1,H}^{(1)}$ is the y-component of $\mathbf{u}_{1,H}^{(1)}$. Recalling (4.14), we can expand and simplify (4.19) to

$$\frac{\partial}{\partial y} \left(\overline{\overline{h}v_{1,H}^{(1)} + h'v_{1,H}^{(1)'}} \right) = -\tau_0 \overline{w_{1,e}};$$

i.e.,

$$\frac{\partial}{\partial y} \left(\overline{\overline{h}v_{1,H}^{(1)}} \right) + \frac{\partial}{\partial y} \left(\overline{h'v_{1,H}^{(1)'}} \right) = -\tau_0 \overline{w_{1,e}}. \tag{4.20}$$

From (4.20), we note that we have decomposed the zonally averaged *total height flux* $\overline{hv_{1,H}^{(1)}}$ into the zonally averaged *mean height flux* $\overline{\overline{h}v_{1,H}^{(1)}}$ and the zonally averaged *eddy height flux*, $\overline{h'v_{1,H}^{(1)'}}$; i.e.,

$$\overline{hv_{1,H}^{(1)}} = \overline{\overline{h}v_{1,H}^{(1)}} + \overline{h'v_{1,H}^{(1)'}}. \tag{4.21}$$

Using (4.21) in (4.20) we express the upper-layer, time-averaged, zonally averaged equation as

$$\frac{\partial}{\partial y} \left(\overline{hv_{1,H}^{(1)}} \right) = -\tau_0 \overline{w_{1,e}}. \tag{4.22}$$

We also note that by integrating both sides of (4.22),

$$\overline{hv_{1,H}^{(1)}} + C = -\tau_0 \overline{\tau_1(y)}, \tag{4.23}$$

where $\overline{\tau_1(y)}$ is the wind stress applied to the upper layer and C is a constant of integration.

Now moving to (4.17), we replace all variables by their (zonal) mean and varying components and drop arguments as in (4.16); i.e.,

$$\nabla_H \cdot \left(\overline{(\overline{q} + q') \left(\mathbf{u}_{2,H}^{(0)} + \mathbf{u}_{2,H}^{(0)'} \right)} \right) = \mu \tau_0 \overline{w_{2,e}} - r_2' \nabla_H^2 \left(\overline{p} + \overline{p'} \right) + \nu_2' \nabla_H^4 \left(\overline{p} + \overline{p'} \right), \quad (4.24)$$

where we note that $w_{2,e}$ is independent of x. Noting that x-derivatives of the time averaged, zonally averaged variables vanish (see Section 4.4.1 for a discussion), we rewrite (4.24) as

$$\frac{\partial}{\partial y} \left(\overline{(\overline{q} + q') \left(v_{2,H}^{(0)} + v_{2,H}^{(0)'} \right)} \right) = \mu \tau_0 \overline{w_{2,e}} - r_2' \frac{\partial^2}{\partial y^2} \left(\overline{p} + \overline{p'} \right) + \nu_2' \frac{\partial^4}{\partial y^4} \left(\overline{p} + \overline{p'} \right), \quad (4.25)$$

where $v_{2,H}^{(0)}$ is the y-component of $\mathbf{u}_{2,H}^{(0)}$. As above, with (4.14), we expand and simplify (4.25) to

$$\frac{\partial}{\partial y} \left(\overline{\overline{q} v_{2,H}^{(0)} + q' v_{2,H}^{(0)'}} \right) = \mu \tau_0 \overline{w_{2,e}} - r_2' \frac{\partial^2}{\partial y^2} \overline{p} + \nu_2' \frac{\partial^4}{\partial y^4} \overline{p};$$

i.e.,

$$\frac{\partial}{\partial y} \left(\overline{\overline{q} v_{2,H}^{(0)}} \right) + \frac{\partial}{\partial y} \left(\overline{q' v_{2,H}^{(0)'}} \right) = \mu \tau_0 \overline{w_{2,e}} - r_2' \frac{\partial^2}{\partial y^2} \overline{p} + \nu_2' \frac{\partial^4}{\partial y^4} \overline{p}. \quad (4.26)$$

Using the property (4.21) for q and $v_{2,H}^{(0)}$, we can simplify the left-hand side of (4.26) to get the lower-layer, time-averaged, zonally averaged equation as

$$\frac{\partial}{\partial y} \left(\overline{q v_{2,H}^{(0)}} \right) = \mu \tau_0 \overline{w_{2,e}} - r_2' \frac{\partial^2}{\partial y^2} \overline{p} + \nu_2' \frac{\partial^4}{\partial y^4} \overline{p}. \quad (4.27)$$

Integrating in y, we have the alternate equation

$$\overline{q v_{2,H}^{(0)}} + C = \mu \tau_0 \overline{\tau_2(x, y, t)} - r_2' \frac{\partial}{\partial y} \overline{p} + \nu_2' \frac{\partial^3}{\partial y^3} \overline{p}, \quad (4.28)$$

where $\overline{\tau_2(x, y, t)}$ is the zonal-mean wind stress in the lower layer, and C is a constant of integration.

Combining (4.22) with (4.27), we have the time-averaged, zonally averaged analogues of the FG model equations.

In (4.22), $\overline{h v_{1,H}^{(1)}}$ is the mass transport in the upper layer. At quasi-steady state, time-averaged leading-order streamlines are essentially zonally invariant (see Section 4.4.1) and thus there is essentially no net meridional transport. Equation (4.22) suggests that this zero net transport is achieved by the balancing of the Ekman

pumping forcing by a mass transport in the upper layer. Similarly, (4.27) suggests that the potential vorticity flux $\overline{qv_{2,H}^{(0)}}$ is balanced by a combination of lower-layer friction and Ekman forcing on the lower layer (via outcroppings). To more precisely analyze the balance in the upper layer, we decompose upper-layer meridional transport as

$$
\begin{aligned}
\overline{hv_{1,H}^{(1)}} &= \overline{-hp_x} + \overline{hJ(\nabla_H h, h)} + \overline{h\nu_1' h_{yyy}} \\
&:= T_{geostrophic} + T_{nonlinear} + T_{friction},
\end{aligned}
\tag{4.29}
$$

where we have expanded $hv_{1,H}^{(1)}$ using the y-component of (2.92). The lower-layer terms are already suitably decomposed into potential vorticity flux, lower-layer Ekman pumping, and friction terms.

4.4 Simple Channel

In equation (4.21), we separated $\overline{hv_{1,H}^{(1)}}$ into mean and eddy components. However, the time-averaged zonally averaged meridional velocity $\overline{v_{1,H}^{(1)}}$ is typically very small in the simple channel; i.e.,

$$
\overline{v_{1,H}^{(1)}} \approx 0.
$$

With this assumption, we note from (4.21) that

$$
\overline{hv_{1,H}^{(1)}} \approx \overline{h' v_{1,H}^{(1)'}}.
\tag{4.30}
$$

Thus, $T_{geostrophic}$ represents the second-order geostrophic *eddy height flux*, noting that the flux associated with the leading-order geostrophic velocity is 0 (see Section 2.2). By a similar argument, we define $\overline{q' v_{2,H}^{(0)'}} :\approx \overline{qv_{2,H}^{(0)}}$ to be the *eddy potential vorticity flux*.

The simulations that were performed in the simple channel geometry are summarized in Table 4.1. In this table, we assign a name to each simulation performed for easy referencing (i.e., (SC-1)–(SC-16)). Each simulation is described by 4 aspects of the model that is varied. The second column lists the initial upper-layer height used, and the third column list the type of Ekman pumping force used. The term 'balanced' is used to refer to an Ekman pumping force $w_e(x, y, t)$ satisfying (4.8). For the simple channel,

$$
\Omega = \{[0, 96] \times [0, 32]\},
$$

Table 4.1: Simple Channel Simulations

simulation	$h(x, y, 0)$	forcing type	τ_0	bottom topography
SC-1	1.00	balanced	1.981e-5	no
SC-2	1.00	balanced	3.961e-5	no
SC-3	1.00	balanced	5.942e-5	no
SC-4	1.00	balanced	7.922e-5	no
SC-5	0.25	balanced	1.981e-5	no
SC-6	0.25	balanced	3.961e-5	no
SC-7	0.25	balanced	5.942e-5	no
SC-8	0.25	balanced	7.922e-5	no
SC-9	0.25	unbalanced	1.981e-5	no
SC-10	0.25	unbalanced	3.961e-5	no
SC-11	0.25	unbalanced	5.942e-5	no
SC-12	0.25	unbalanced	7.922e-5	no
SC-13	1	balanced	1.981e-5	yes
SC-14	1	balanced	3.961e-5	yes
SC-15	1	balanced	5.942e-5	yes
SC-16	1	balanced	7.922e-5	yes

and the Ekman pumping force as given in (3.21) is balanced in this domain. For an unbalanced wind, we use an alternate forcing function

$$w_e(y) = \chi_{(y<8)} + \chi_{(y>8)} \cos\left(\frac{\pi(8-y)}{24}\right), \tag{4.31}$$

where χ is the characteristic function over the given domain. Because

$$\int_{x_L}^{x_R}\int_{y=8}^{y=32} \cos\left(\frac{\pi(8-y)}{24}\right) dxdy = 0,$$

it is clear that

$$\iint_\Omega w_e(y)dxdy > 0, \tag{4.32}$$

where $w_e(y)$ is as in (4.31). Noting the negative sign on the right-hand side of (2.90), (4.32) implies a net upward Ekman pumping force, which destroys upper-layer mass. We discuss the implications in Section 4.4.3. The fourth column lists the Ekman pumping strength and the last column indicates whether a topographic ridge (yes) or a flat bottom (no) has been used in the simulation.

4.4.1 SC-1 – SC-4

We first consider the simulations SC-1 to SC-4. This is a basic set of simulations in which the lower layer will not outcrop due to the sufficiently large initial upper-layer depth and balanced Ekman forcing.

In the presence of a balanced wind, we showed in Section 4.2 that mass should be conserved; i.e., (4.9) holds. The model clearly displays conservation of M (4.2), and thus conservation of total mass. For SC-4, relative error in the conservation of M over the entire integration period is on the order of 1e-7, in the realm of numerical error as discussed in Section 2.3.1.

Figure 4.2 shows the evolution of FG potential energy (4.11) for SC-4. As the front builds (see Figure 4.1.a), potential energy increases. At the onset of turbulence (see Figure 4.1.b), the potential energy decreases due to the release of potential energy stored in the front into kinetic energy (4.12) via eddy formation. We see a rapid corresponding increase in kinetic energy at the onset of turbulence; see Figure 4.3. At the establishment of a quasi-steady state (see Figure 4.1.c), both potential energy and kinetic energy oscillate about a mean constant value. Figure 4.4 shows lower-layer FG momentum (4.13), which also indicates a quasi-steady state by oscillating about a mean constant value. Thus, while the conservation of mass lends credence to the validity of the numerical solution, the oscillation about a mean of the energies and momentum support the notion that a quasi-steady state has been established.

The leading-order, geostrophic flow in the upper and lower layers respectively is given by (2.75) and (2.80). From these equations, we can deduce that the upper and lower-layer velocities are oriented perpendicular to the gradient of $h(x,y,t)$ and $p(x,y,t)$ respectively. Therefore, we can easily construct streamlines of the leading-order flow in the upper layer via contours of $h(x,y,t)$, and in the lower layer via contours of $p(x,y,t)$. In the absence of any topography or land barriers as in the simple channel case, the time-mean flow should be invariant in x. The time-averaged leading-order streamlines in both layers are shown in Figure 4.5. These streamlines imply that since the leading-order flow is primary directed zonally, time-averaged meridional velocities are very small.

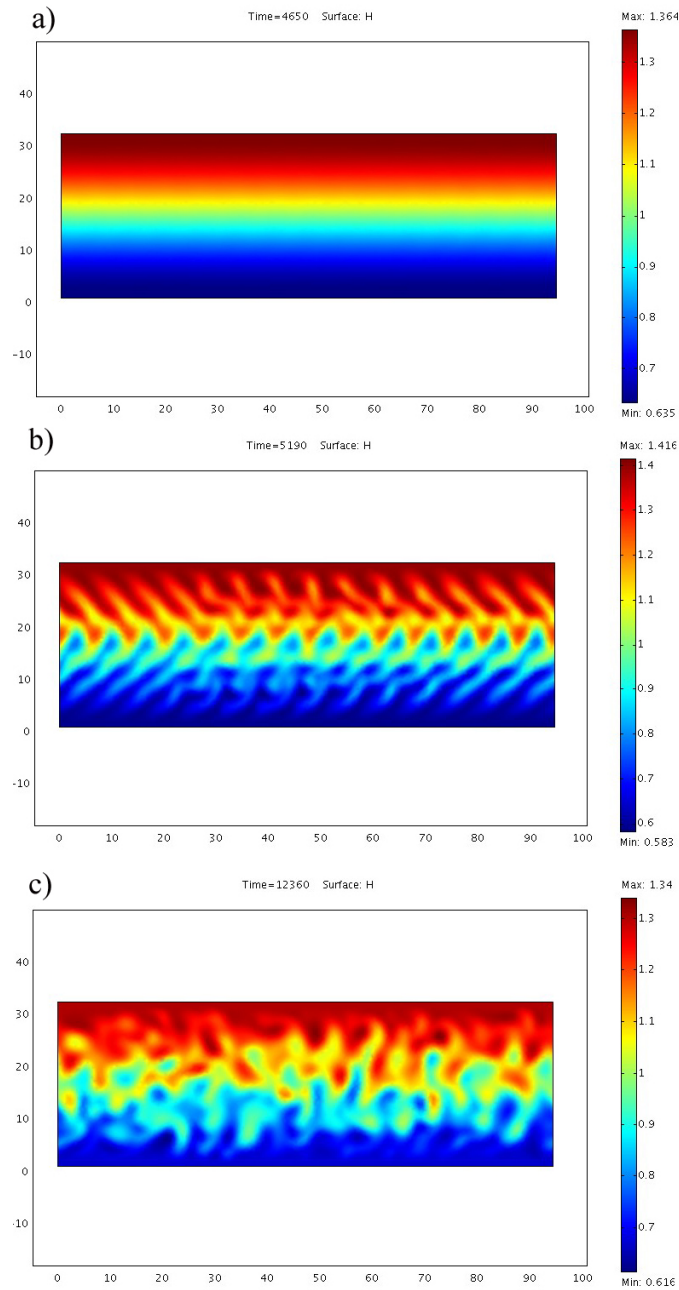Figure 4.6 shows the zonally averaged geostrophic leading-order velocity in each

Figure 4.1: a): A snapshot in time of $h(x, y, t)$ before turbulence, $t = 4180$, b): a snapshot in time of $h(x, y, t)$ at the initial onset of turbulence, $t = 5190$, c): a snapshot in time of $h(x, y, t)$ at quasi-steady state, $t = 12360$. (SC-4)
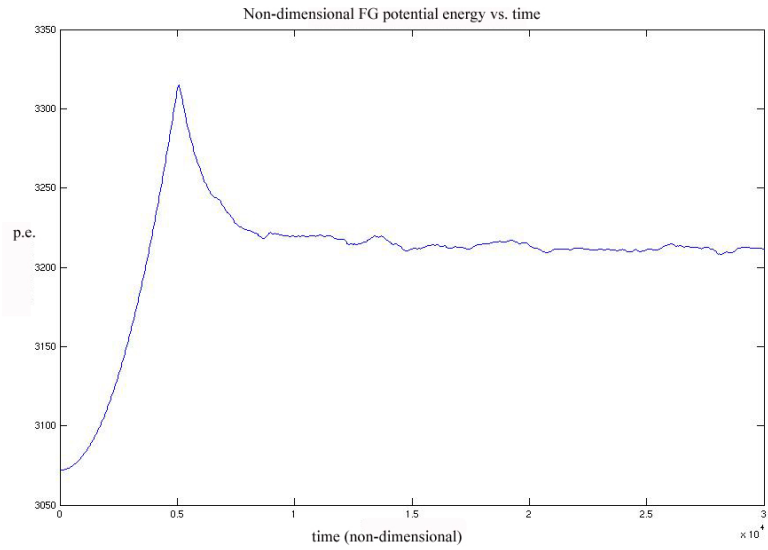
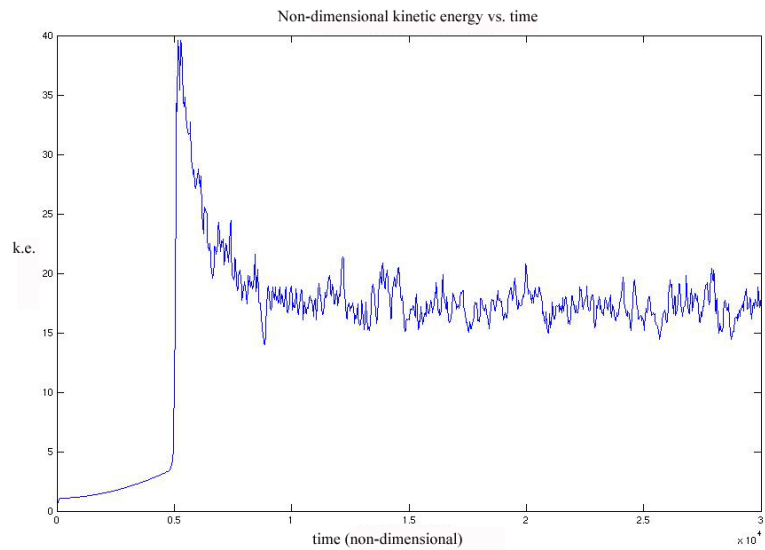Figure 4.2: Time series of nondimensional FG potential energy (4.11). (SC-4)

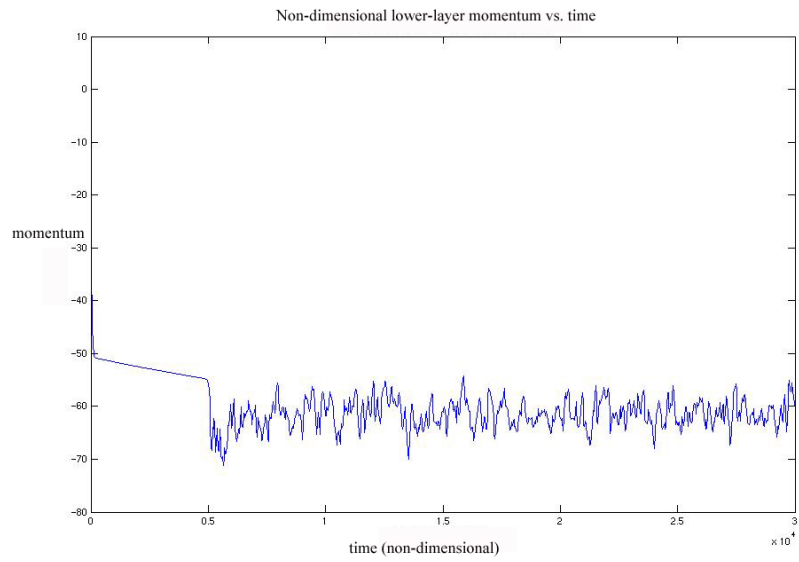Figure 4.3: Time series of nondimensional FG kinetic energy (4.12). (SC-4)

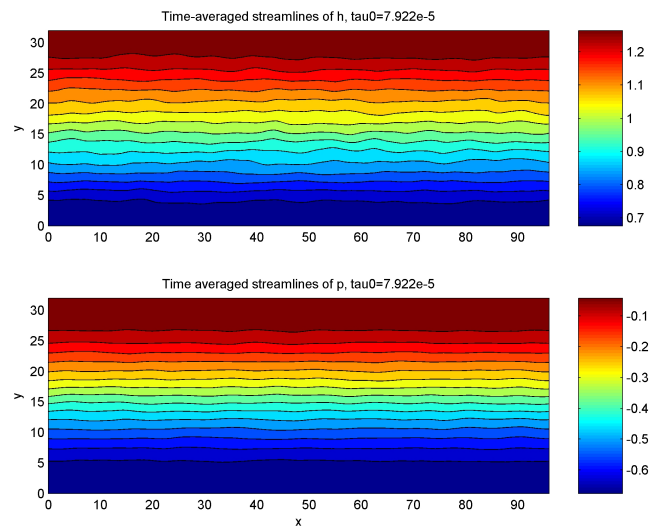Figure 4.4: Time series of nondimensional FG lower-layer momentum N (4.13). (SC-4)

Figure 4.5: Streamlines of geostrophic flow in each layer for a strong wind, $\tau_0 =$7.922e-5. (SC-4)
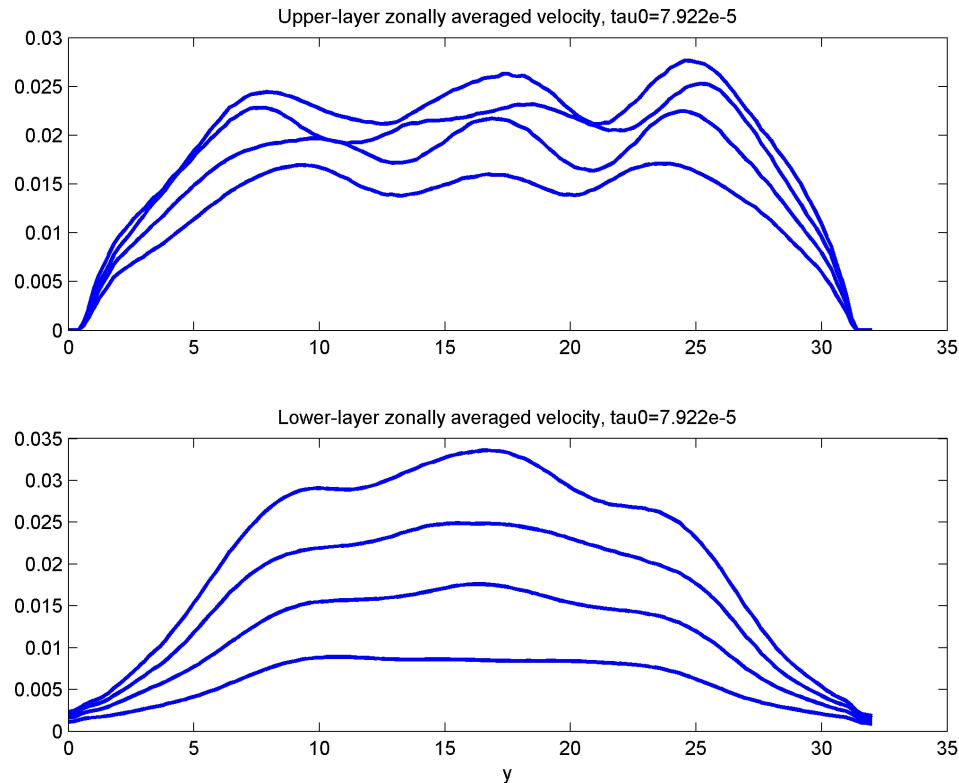
Figure 4.6: Upper- and lower-layer time-averaged, zonally averaged velocity for $\tau_0 = $ 1.981e-5 – 7.922e-5. As τ_0 increases, the magnitude of velocity in each layer increases. Note that these are nondimensional velocity values. (SC-1 – SC-4)

layer for 4 Ekman pumping strengths. In the upper layer, the flow is organized into zonal jets, in keeping with the results of [33]. As the Ekman pumping strength increases, the velocity required to balance the forcing also must increase to achieve a quasi-steady state. Thus, the zonal velocity increases in magnitude through successively larger values of τ_0, as indicated in Figure 4.6. For $\tau_0 = 5.942$e-5, results from the geostrophic vorticity model [33] show a single jet predominating; this is not the case for this FG model implementation nor the HIM model [12]. The single jet is caused by low values of lower-layer Ekman friction, allowing an unphysically large transport as discussed in Section 3.3.

We now examine the upper-layer zonally averaged mass balance in the context of our model results. As discussed in Section 4.3, we can analyze the upper-layer

balance via either (4.22) or (4.23). However, numerical results for (4.22) require a fair amount of smoothing to clearly observe the signals present in the balance due to the non-smooth high-order y-derivatives and relatively small signals in the time-mean. Thus, we mainly show results using (4.23), and show results for (4.22) only where necessary.

Figures 4.7 and 4.8 show upper-layer mass balances using (4.23) for 2 values of τ_0 corresponding to SC-1 and SC-4. Because we must have an essentially zero net meriodional transport of $h(x, y, t)$ at a quasi-steady state, we must have a balance of the transport terms, and thus, the constant of integration C in (4.23) is 0. This is evident in Figures 4.7 and 4.8. We can deduce from these plots that the leading-order balance occurs between the transport driven by the geostrophic eddy height flux, $T_{geostrophic}$, and the transport driven by the Ekman pumping force, defined as T_{Ekman} (supporting the use of a geostrophic model). Although the nonlinear component of transport, $T_{nonlinear}$, is small, these terms are important for the development of eddies, and hence they are not negligible [15]. The nonlinear component also plays a role in the acceleration of zonal jet as evidenced by the correspondence between the position of the upper-layer jets in Figure 4.6 and the nonlinear component in Figure 4.8. Additionally, although the frictional component of transport, $T_{friction}$, is small, the presence of friction is important for the stability and smoothness of solutions, as well as the feasibility of our boundary conditions. The composition of the upper-layer mass balance remains similar as τ_0 increases. However, the leading-order balance terms, $T_{geostrophic}$ and T_{Ekman} increase in magnitude with τ_0 relative to the frictional and nonlinear terms. Thus, as τ_0 increases, the leading-order balance becomes even more dominant.

We also include a plot indicating the same balance as shown in Figure 4.8, but instead using Equation (4.22). The data in Figure 4.8 are rather noisy, and this effect is magnified upon calculating the derivative. As a result, a 5-point *moving average* smoothing calculation was performed to reduce the noise. This moving average computes a point x_i using an average of the 5 previous points; i.e.,
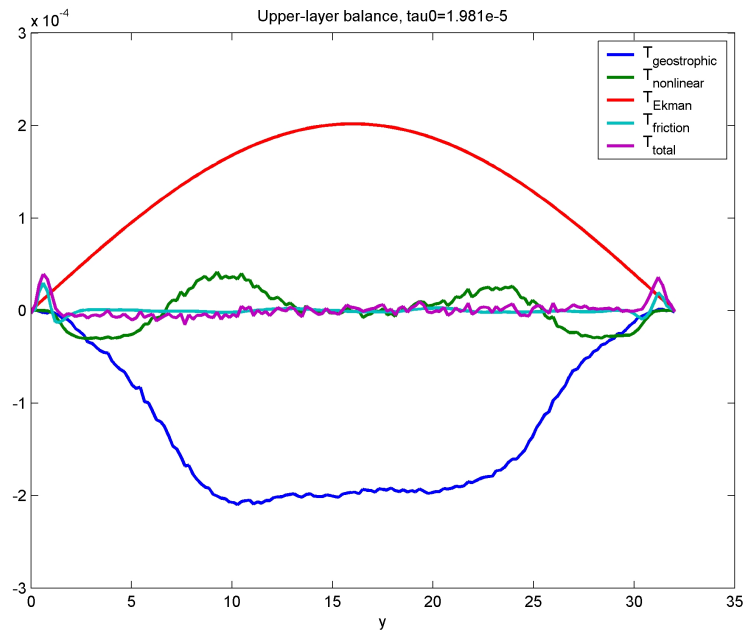
$$x_i = \frac{1}{5} \sum_{j=1}^{5} x_{i-j}.$$

Figure 4.7: Time-averaged zonal-mean balance in upper layer for a weak wind, $\tau_0 =$1.981e-5, from (4.23). Transport terms are defined by (4.29). (SC-1)
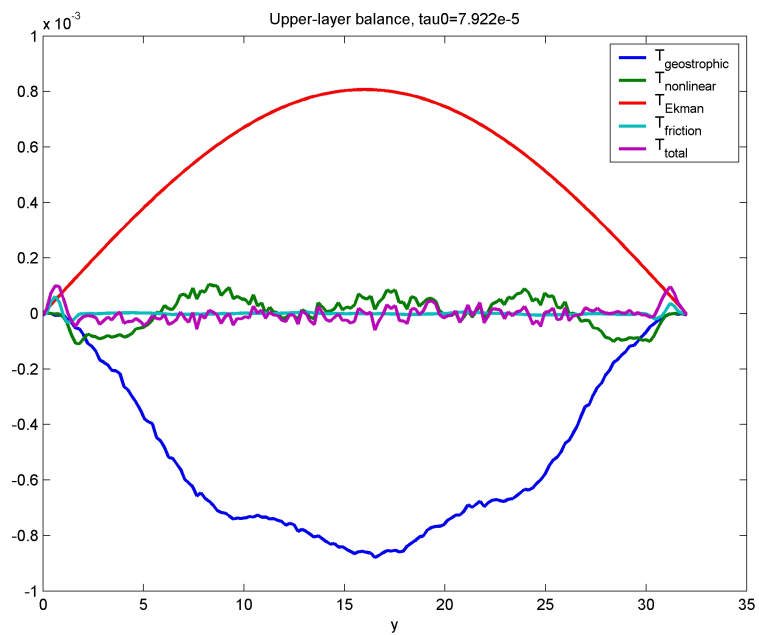

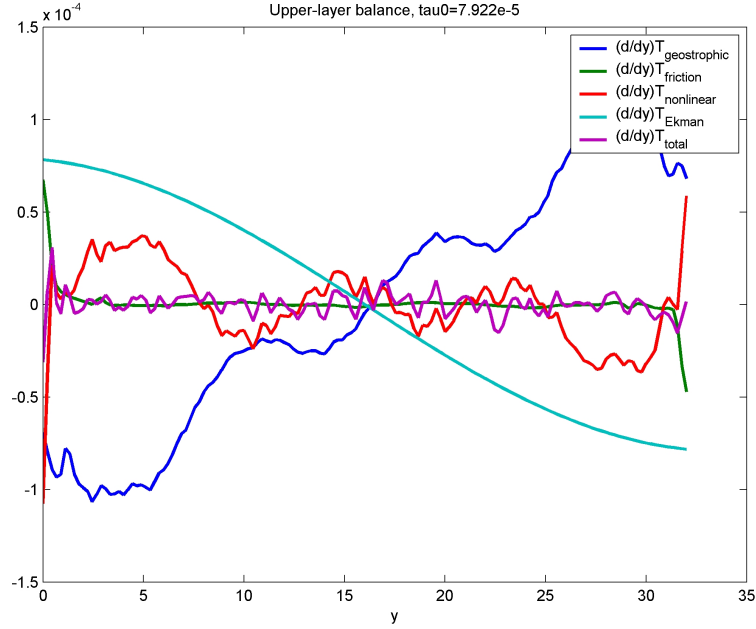Figure 4.8: Time-averaged zonal-mean balance in upper layer, $\tau_0 =$7.922e-5, from (4.23). (SC-4)

Figure 4.9: Time-averaged zonal-mean balance in upper layer, $\tau_0 = 7.922$e-5, from (4.22). (SC-4)

Nevertheless, the balance between components of (4.22) shown in Figure 4.9 is clear. The presence of this balance is conclusive evidence that a quasi-steady state has been reached in the upper layer.

We now consider the lower-layer zonally averaged balances using the model results from SC-1 – SC-4. We note that because $\mathbf{n} \cdot \nabla_H p$ and $\mathbf{n} \cdot \nabla_H q$ are not necessarily zero at the boundary $y = 32$ (where instead we have applied a Dirichlet condition; see (2.104)), the constant of integration in (4.28) is nonzero. However, it remains constant in y, and thus (4.27) still holds. Figures 4.10 and 4.11 show the balance established in the lower layer using (4.28) for 2 values of τ_0. Additionally, we show this balance via (4.27) for $\tau_0 = 7.922$e-5 in Figure 4.12. As in the upper layer, the data are smoothed using a moving-average calculation due to the noisy derivative terms. These figures clearly show that the leading-order balance is between the eddy potential vorticity flux $\overline{-q'p'_x}$, and linear friction. As in the upper layer, the balances remain largely similar as τ_0 increases save for an increase in magnitude of potential vorticity flux and linear friction terms. To further understand the lower-layer balance,
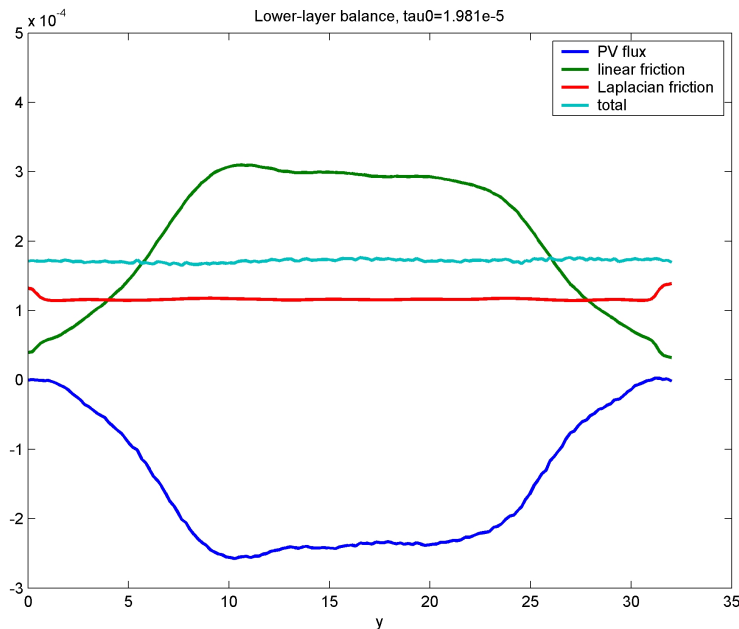
Figure 4.10: Time-averaged zonal-mean balance in lower layer, $\tau_0 = 1.981e\text{-}5$, from (4.28). (SC-1)

we decompose $\overline{q'p'_x}$ by expanding $q(x, y, t)$ from (2.94). Figure 4.13 plots the zonally averaged decomposition of $\overline{q'p'_x}$ into $\overline{\mu h'p'_x}$, $\overline{\beta y'p'_x}$, and $\overline{\nabla^2_H p'p'_x}$. From this plot, it is evident that $\overline{q'p'_x}$ is essentially determined by $\overline{\mu h'p'_x}$, which is an eddy mass flux.

We now can formulate a balance mechanism based on the simulation results SC-1 – SC-4. Momentum is imparted at the surface by a wind stress, which is manifested by a resultant Ekman pumping force in our model. This momentum is balanced in the upper layer by an eddy height flux. In the lower layer, the eddy height flux is balanced by the Ekman friction at the bottom. Thus the eddy height flux acts to transfer momentum from the upper layer to the lower layer, where it is eventually dissipated at the bottom. We note that the eddy height flux can be interpreted as the eddy interfacial formstress, as discussed in Section 2.1 [12].

4.4.2   SC-5 – SC-8

The simulations SC-5 – SC-8 use a relatively shallow initial upper-layer depth with a balanced Ekman pumping force. Then, as the front develops, outcropping will occur;
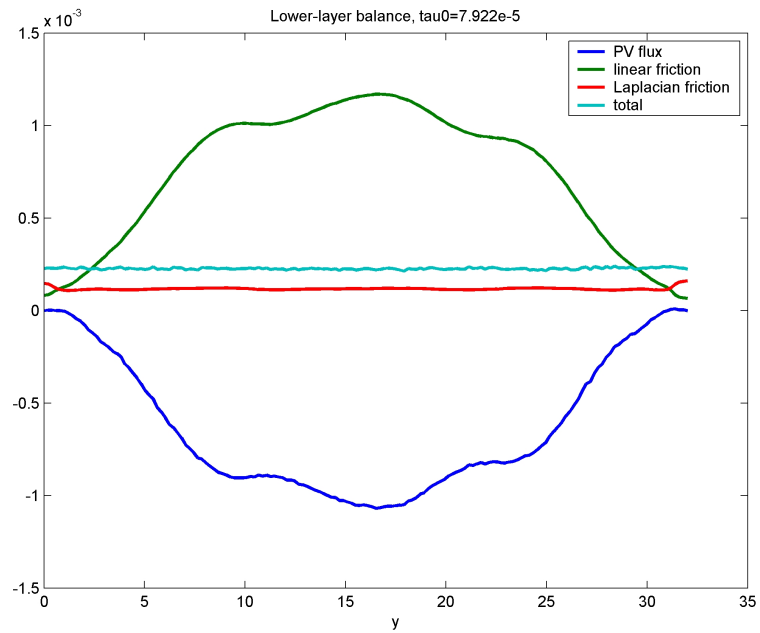
Figure 4.11: Time-averaged zonal-mean balance in lower layer, $\tau_0 = 7.922e\text{-}5$, from (4.28). (SC-4)
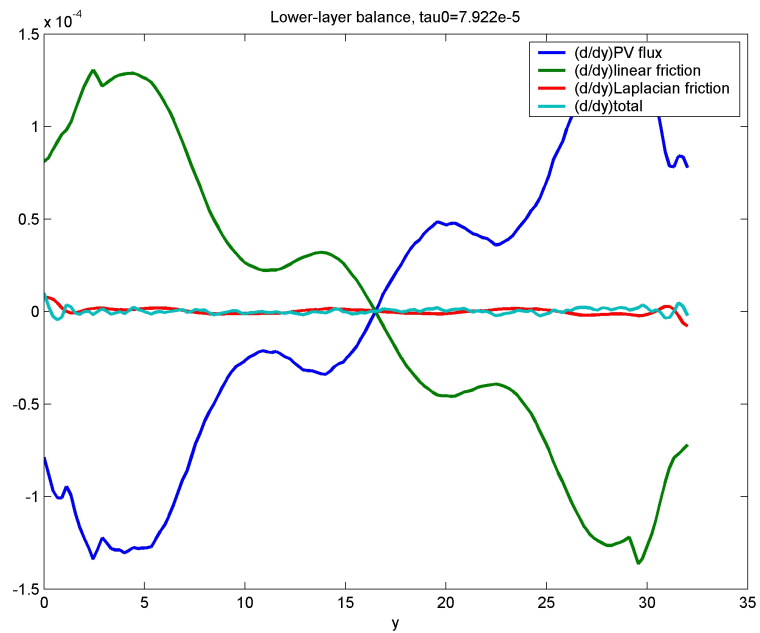

Figure 4.12: Time-averaged zonal-mean balance in lower layer, $\tau_0 = 7.922e\text{-}5$, from (4.27). (SC-4)
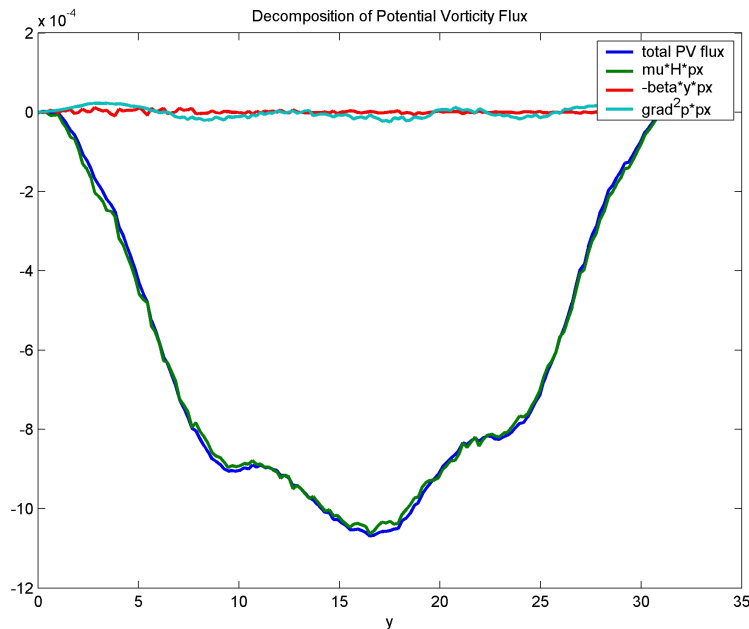
Figure 4.13: Decomposition of $\overline{-q'p'_x}$. (SC-4)

that is, a region of $h(x, y, t) = 0$ will form, such that the lower layer intersects the surface. Recall the definition of the upper Ekman pumping force $w_{1,e}(x, y, t)$ defined in (2.36):

$$w_{1,e}(x, y, t) = \begin{cases} w_e(x, y, t) & \text{if } h(x, y, t) > 0, \\ 0 & \text{if } h(x, y, t) = 0, \end{cases}$$

where $w_e(x, y, t)$ is the Ekman pumping velocity. Thus, on the region where $h(x, y, t) = 0$, there is no forcing applied to the upper layer. Then the Ekman pumping force is no longer balanced, and mass is not conserved. Yet for a quasi-steady state to exist, the mass must be constant, as otherwise the frontal profile of $h(x, y, t)$ would be changing. The system still reaches a steady state, however. By advection of $h(x, y, t)$, the outcropping region (i.e., where $h(x, y, t) = 0$) becomes smaller in area until the winds are once again balanced. In the case of a balanced wind, this can only occur when the outcropping region vanishes, at which point the system can achieve a quasi-steady state. Figure 4.14 shows a time series of mass for SC-8. This process of establishing a steady state via the vanishing of an outcropping is time consuming – Figure 4.14 was run to 90 000 units, or 3 times the normal time-integration period.
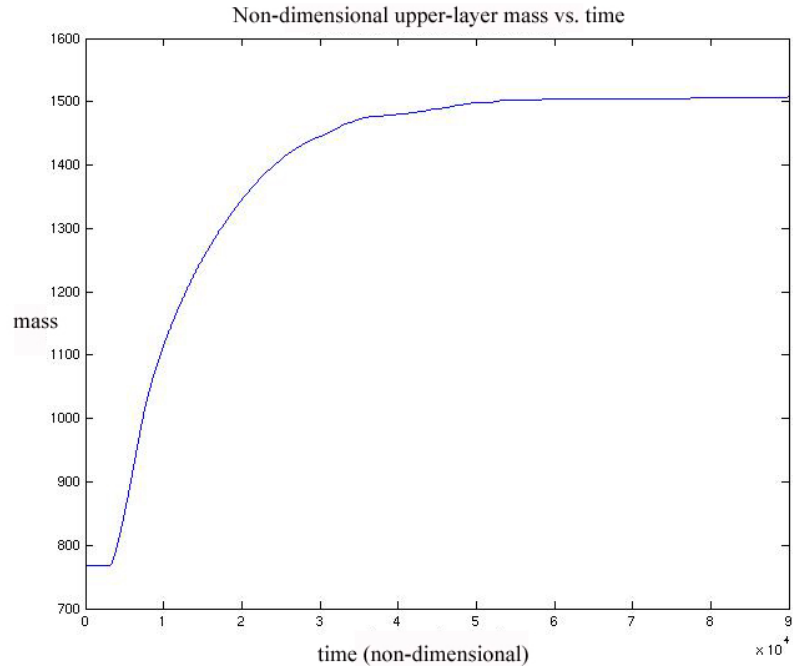
Figure 4.14: Time series of nondimensional upper-layer mass M. The mass remains constant until an outcropping occurs, at which time the unbalanced winds create a mass influx. This outcropping slowly disappears, at which point mass becomes conserved again. (SC-8)

Data from simulations SC-5 – SC-7 are not shown because the weaker winds require much longer integration times to achieve a steady state, and these data are of no particular interest.

For SC-8, we plot the upper- and lower-layer balances in Figures 4.15 and 4.16 to validate the existence of a quasi-steady state. Because the outcropping region disappears at quasi-steady state, the balances are qualitatively the same as for simulations SC-1 – SC-4.

Figure 4.17 shows a time series of upper-layer mass for SC-8 with a variety of initial values for $h(x, y, t)$. These results suggest that for simulations that exhibit outcropping, the upper-layer depth at quasi-steady state is independent of the initial upper-layer depth. Outcropping will occur when the initial value of $h(x, y, t)$ is less than the mean value of $h(x, y, t)$ at quasi-steady state. From Figure 4.17 we note that the upper-layer mass at quasi-steady state for SC-8 is given by approximately 1507.5.
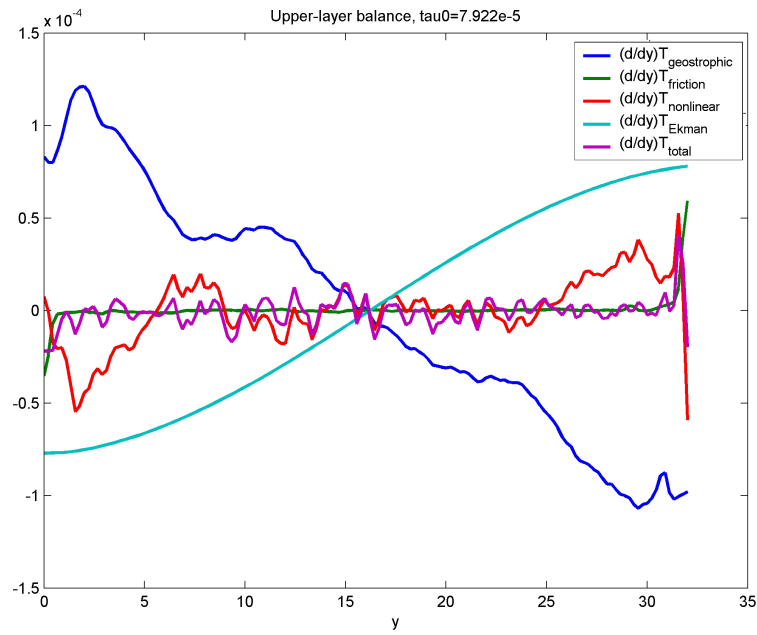
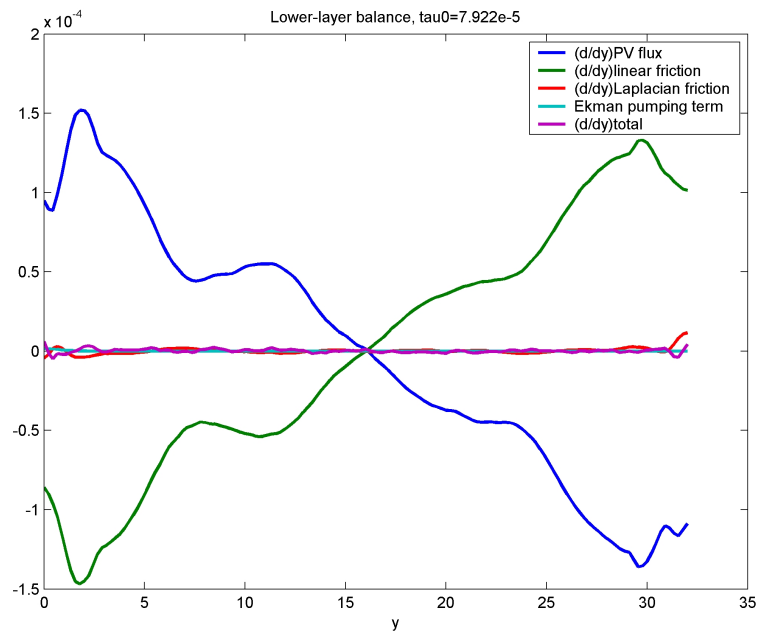Figure 4.15: Time-averaged zonal-mean balance (4.22) in upper layer. (SC-8)

Figure 4.16: Time-averaged zonal-mean balance (4.27) in lower layer. (SC-8)
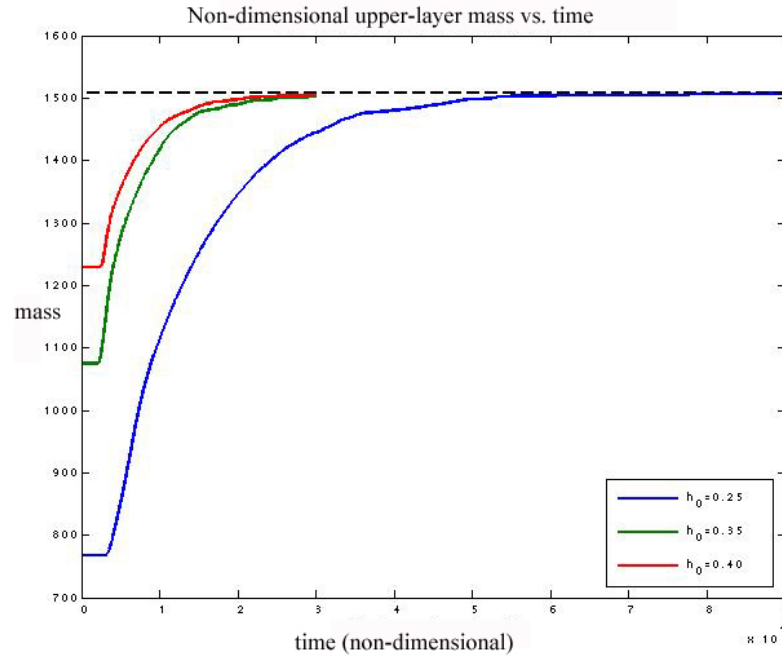
Figure 4.17: Time series of upper-layer mass M for 3 different initial values for $h(x, y, t)$. In each run, an upper-layer mass of approximately 1507.5 prevails at the quasi-steady state. (SC-8)

Thus, we find a mean value of $h(x, y, t)$ at quasi-steady state of $1507.5/(32 \cdot 96) = 0.4907$.

4.4.3   SC-9 – SC-12

Runs SC-5 – SC-8 are characterized by an outcropping of the lower layer that vanishes at quasi-steady state. However, it is possible to have an outcropping at the quasi-steady state. If an unbalanced Ekman forcing term is used, the system evolves to form an outcropping. This outcropping increases in area until the Ekman forcing term is balanced on the remaining upper layer. Thus, the effect of the lower-layer outcropping is to redefine the upper-layer domain such that the forcing is balanced on this new domain, and thus a quasi-steady state solution can be established.

Runs SC-9 – SC-12 use an unbalanced Ekman forcing function as defined in (4.31). Here, we have defined $w_e(y)$ such that on $\chi_{(y>8)}$, $w_e(y)$ is balanced. Then we expect
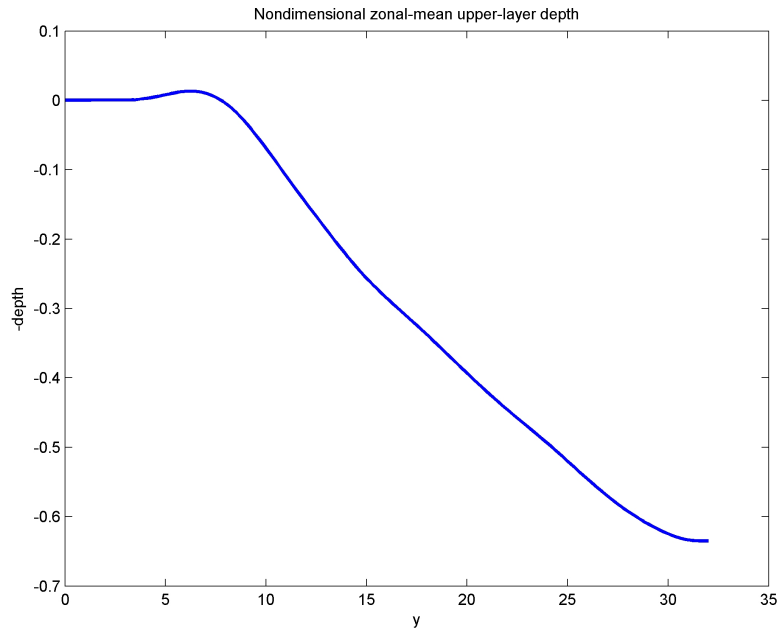
Figure 4.18: Time-averaged zonal-mean profile of h, the upper-layer depth, from SC-12. The y-axis has been negated to intuitively display h as a depth. The outcropping (where $h=0$) covers the predicted region $y \approx [0,8]$.

the outcropping to cover the area $\{[0, 96] \times [0, 8]\}$. Figure 4.18 shows the zonal-mean upper layer depth from SC-12. Clearly, the outcropping interface occurs in the predicted region of $y = 8$. Notice in Figure 4.18 that our FEMLAB implementation smooths discontinuities in the solution of $h(x, y, t)$, and thus we get small, but non-physical negative values near the outcropping interface.

Associated balances for the runs are similar (except for the specific values of the magnitudes) for the various values of τ_0, and thus, we show upper- and lower-layer balances for just one value of τ_0 in Figures 4.19 and 4.20. We proceed with this convention of showing balances for only one value of τ_0 for the remainder of the chapter. In the region of lower-layer outcropping, the Ekman pumping force is applied to the lower layer via $w_{2,e}(x, y, t)$ (see 2.43)). As a result, the prevailing lower-layer balance on the outcropping region is between the Ekman pumping force and the linear friction dissipation, as shown in Figure 4.20. There is some error in the balance in the region of the outcropping interface. This is likely due to small negative values of $h(x, y, t)$ that cannot be forced to 0 after each timestep. Negative values of $h(x, y, t)$
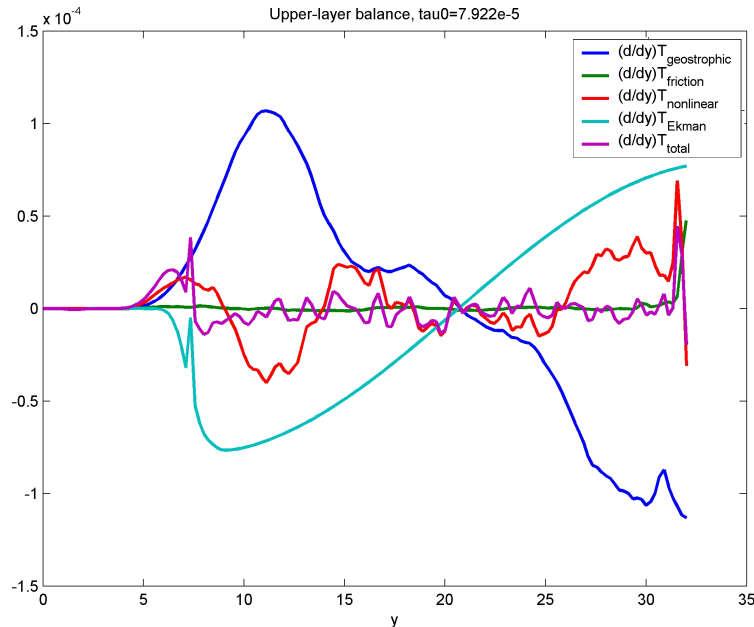
Figure 4.19: Nondimensional zonal-mean upper-layer balance (4.22). (SC-12)

cause significant problems in the finite-difference FG implementation [29], requiring a modified timestepping scheme that eliminates negative values at each time step [12]. However, the presence of negative values does not affect the stability of the finite element implementation in this thesis, although unphysical values of $h(x, y, t) < 0$ are present.

The final state of $h(x, y, t)$ in these simulations is independent of the initial value, $h(x, y, 0)$. Figure 4.21 shows upper-layer mass for a variety of initial values in simulation SC-12. For each initial value, the upper-layer mass converges to a value of approximately 836.3.

4.4.4 SC-13 – SC-16

Simulations SC-13 – SC-16 are characterized by the inclusion of a topographic ridge defined by (3.22). The inclusion of bottom topography significantly affects the flow profile in the simulations. Figure 4.22 shows the time-averaged flow in the upper and lower layers for a weak wind, $\tau_0 = 1.981e-5$. The flow in the upper layer is deflected northward along the topographic ridge. The zonal transport is significantly
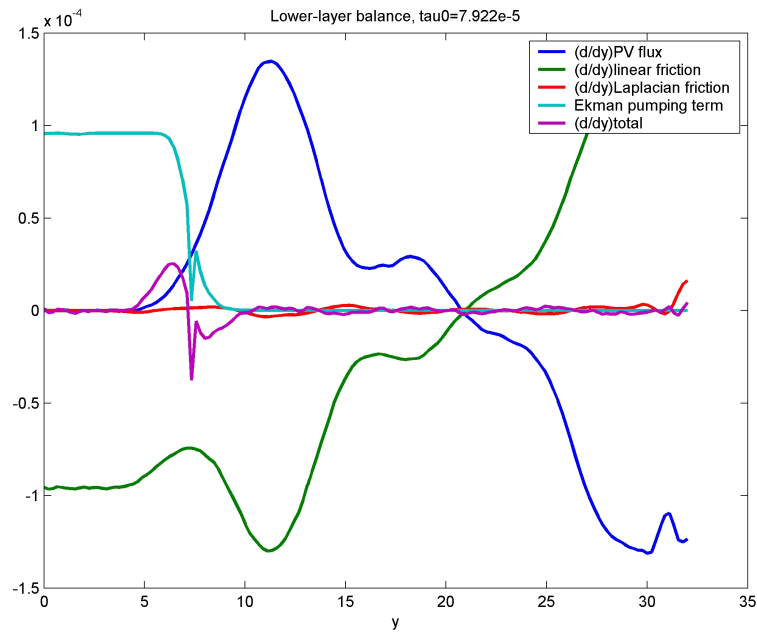
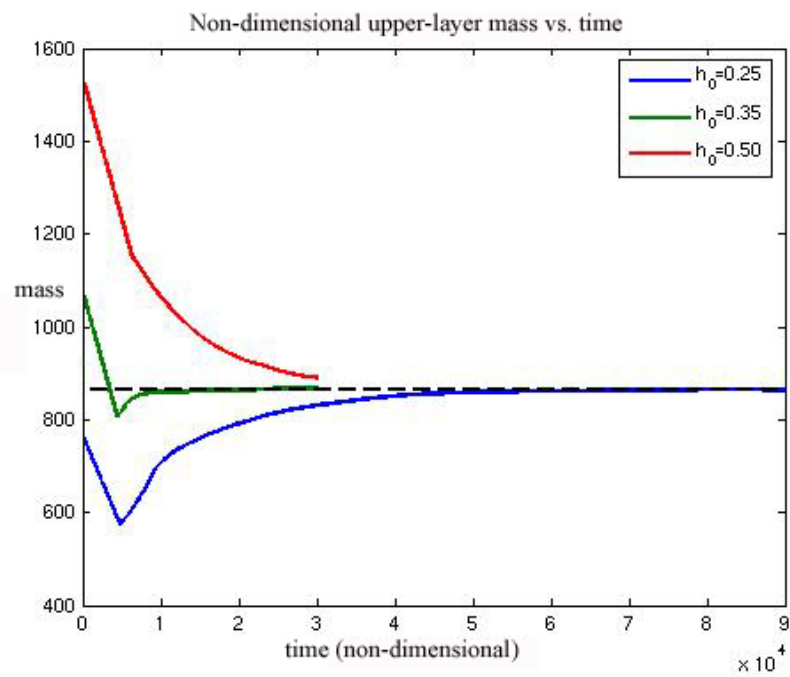Figure 4.20: Nondimensional zonal-mean lower-layer balance (4.27). (SC-12)

Figure 4.21: Time series of upper-layer mass for varying values of $h(x, y, 0)$. Also shown in the dashed line is the mass value to which the system converges. (SC-12)
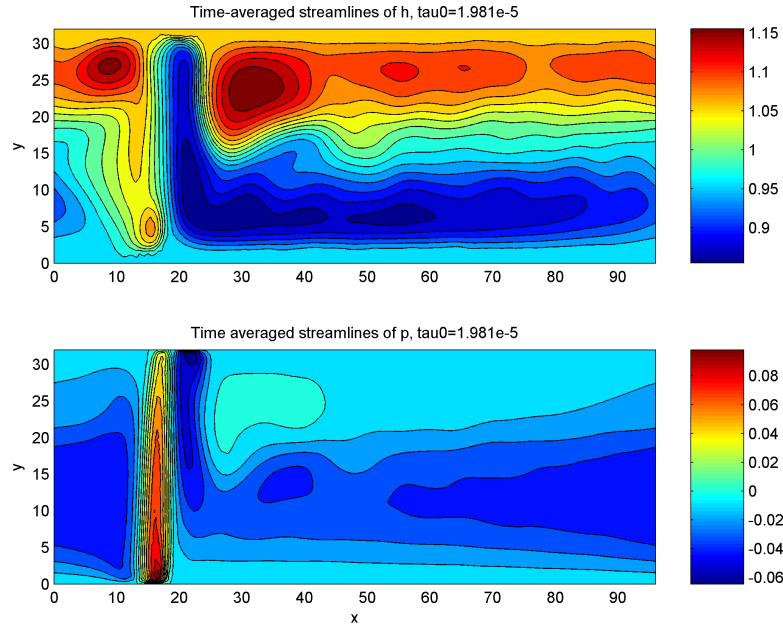
Figure 4.22: Time-averaged streamlines in the upper and lower layers. (SC-13)

reduced, and recirculating gyres appear on both sides of the ridge. In the lower layer, the topographic ridge effectively eliminates any zonal transport, although an unrealistically strong flow appears above the topographic ridge, which is a known problem in a number of other idealized models [12]. Figure 4.23 shows the time-averaged flow in the upper and lower layers for a strong wind, $\tau_0 = 7.922$e-5. The profile is similar to Figure 4.22, although in the upper layer, the recirculating gyres are smaller, allowing a larger zonal transport.

In contrast to the simple channel simulations with no bottom topography, simulations with bottom topography do not have a zonally invariant mean flow. Therefore, there is the possibility of meridional mean mass fluxes and eddy mass fluxes, as in (4.21). However, in Figures 4.22 and 4.23, there is a northward flow west of the topography, and an southward flow to the east of the topography. Upon zonally averaging meridional flow, these two flows essentially cancel out, leaving a very small net meridional mean flow. The decomposition of $\overline{hp_x}$ is shown in Figure 4.24.

Figures 4.25 shows the upper-layer balance for a strong wind, $\tau_0 =7.922$e-5. As in the simple channel simulations with no topography, the leading-order upper-layer
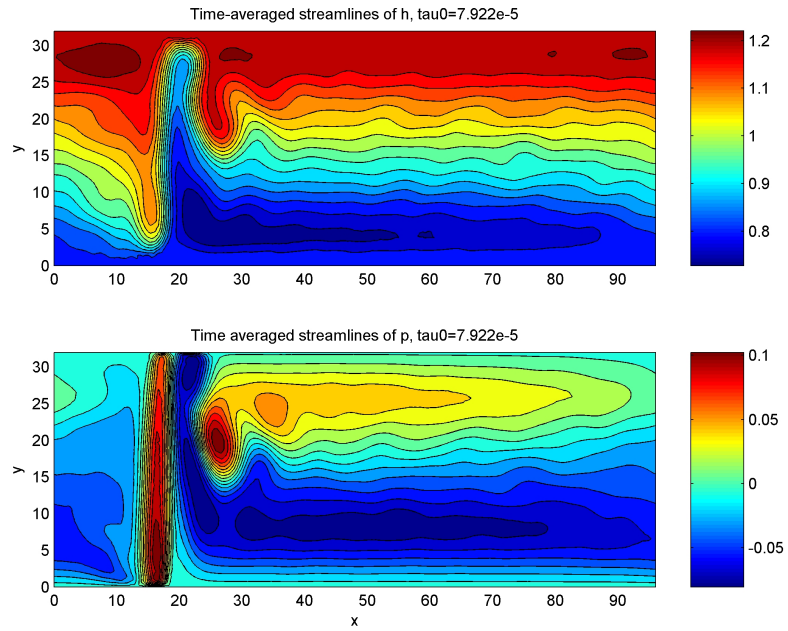
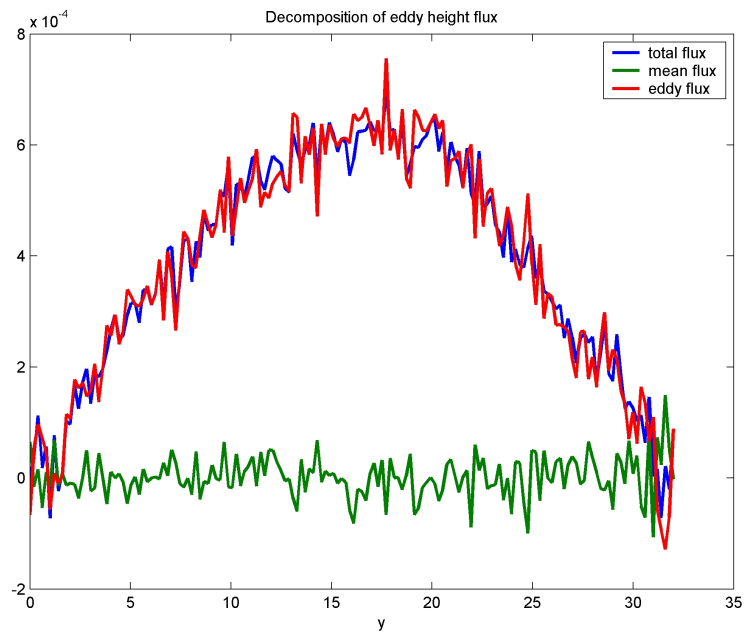Figure 4.23: Time-averaged streamlines in the upper and lower layers. (SC-16)

Figure 4.24: Decomposition of $\overline{hp_x}$ into mean $(\overline{h}\,\overline{p_x})$ and eddy $(\overline{h'p'_x})$ components. (SC-16)
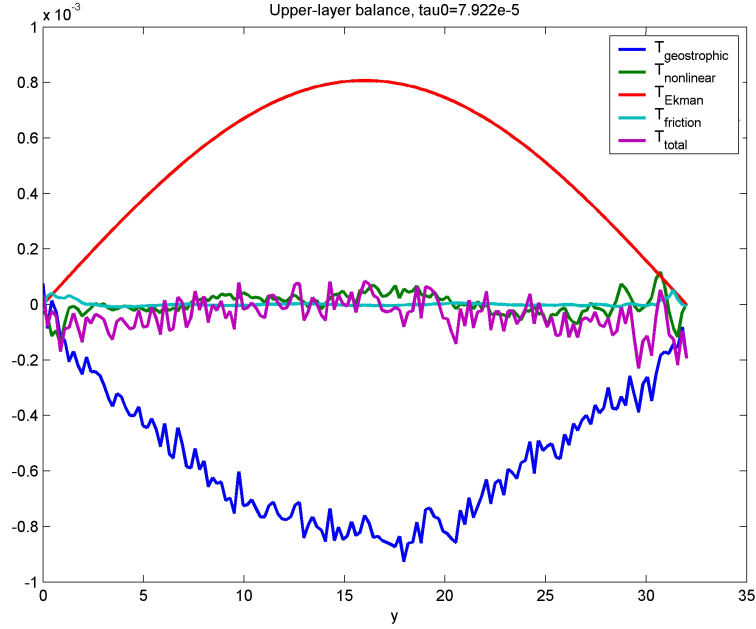
Figure 4.25: Time-averaged zonal-mean balance (4.22) in upper layer. (SC-16)

balance is established between the eddy-flux transport and the Ekman transport. In the lower layer, as in simulations SC-1 – SC-4 the potential vorticity flux is balanced by bottom friction. However, the implication of this balance is different due to the inclusion of bottom topography. In these simulations, $q(x, y, t)$ includes the additional term $\mu_B h_b(x, y)$ representing bottom topography. With this additional term, $\overline{q' p'_x}$ is no longer essentially determined just by $\overline{\mu h' p'_x}$, but instead it is the addition of this term and $\overline{\mu_B h_B(x, y) p_x}$ that essentially determines $\overline{q' p'_x}$. The lower-layer balance is shown in Figure 4.26. In this figure, potential vorticity flux is decomposed into $\overline{\mu h' p'_x}$ and $\overline{\mu_B h_B(x, y) p_x}$.

From Figure 4.26, we deduce an altered balance mechanism in the presence of bottom topography. As is the case with no topography, momentum imparted at the surface by a wind stress is balanced in the upper layer by an eddy height flux (i.e., interfacial formstress) that transfers momentum to the lower layer. However, in the lower layer, now a combination of bottom friction and bottom topography (i.e., bottom formstress) act in concert to dissipate the momentum and achieve a balanced state. As bottom friction is reduced, the bottom formstress dominates the balance.
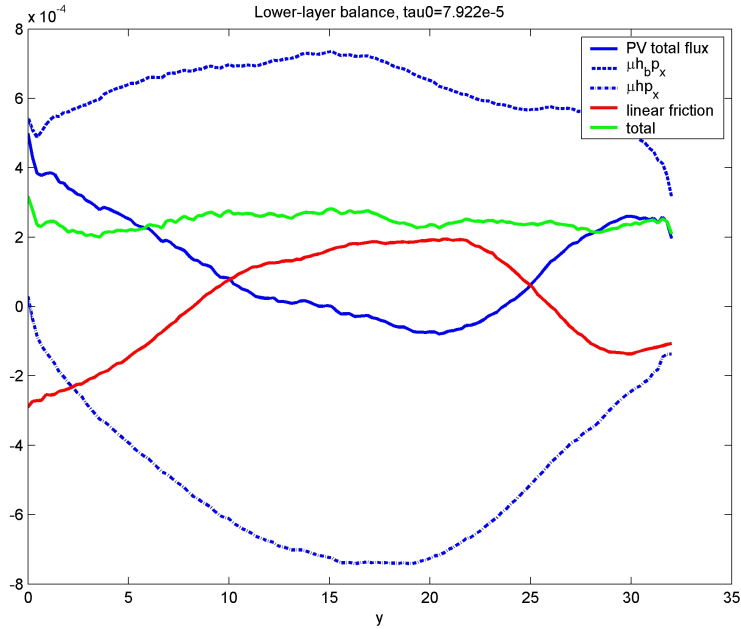
Figure 4.26: Time-averaged zonal-mean balance (4.27) in lower layer. PV total flux has been smoothed by a 5-point moving average. (SC-16)

We now compare the upper-layer depth and lower-layer pressure profiles for the three simple channel simulation types. Figure 4.27 shows profiles of $\overline{h(x,y,t)}$ for SC-4, SC-8, and SC-12. To display slope differences, profiles for SC-8 and SC-12 have been translated to agree with SC-4 at $y = 0$. Figure 4.27 suggests that the occurrence of outcropping in SC-8, although transient, enables a steeper gradient in $\overline{h(x,y,t)}$ at quasi-steady state, implying a stronger upper-layer flow. For SC-12, in which the outcropping prevails at quasi-steady state, the gradient in $h(x,y,t)$ is very similar to that of SC-8, except on the region of outcropping, where the gradient is essentially flat. The total change in $h(x,y,t)$ in SC-4 and SC-12 is almost equal, as the stronger gradient in SC-12 is counterbalanced by the outcropping region of essentially zero slope.

Figure 4.28 shows profiles of $\overline{p(x,y,t)}$ for SC-4, SC-8, and SC-12. The gradient is smallest with no outcropping (SC-4); it is considerably stronger for the outcropping simulations (SC-8 and SC-12). There is a tailing off effect in $p(x,y,t)$ for SC-12 due to the outcropping region.
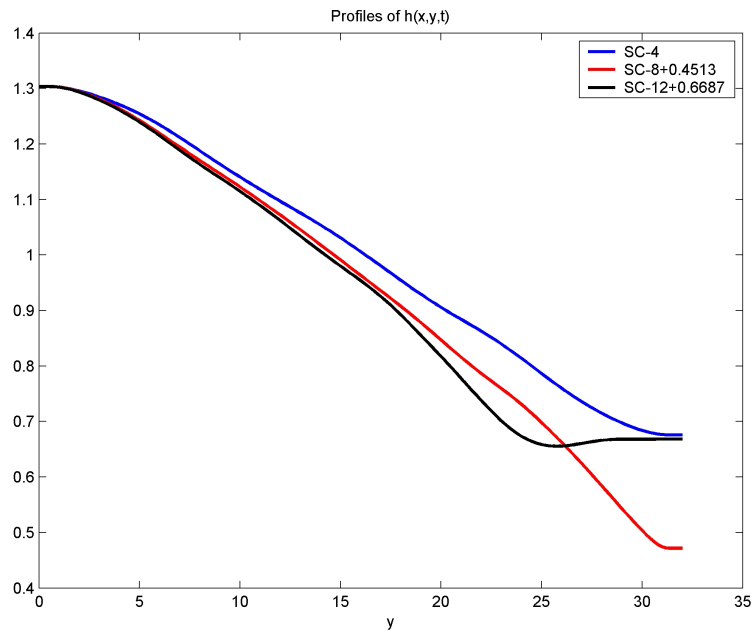
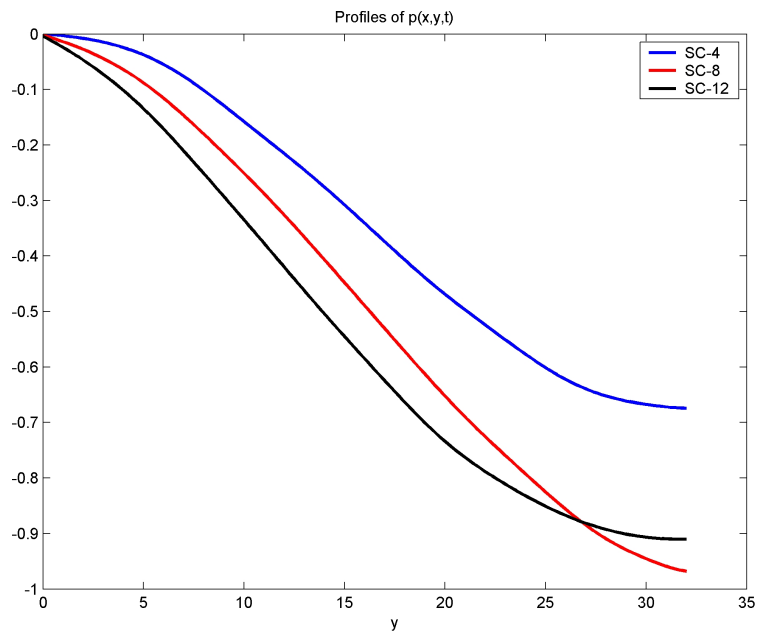Figure 4.27: Upper-layer depth profiles, $h(x, y, t)$. (SC-4, SC-8, SC-12)

Figure 4.28: Lower-layer pressure profiles, $p(x, y, t)$. (SC-4, SC-8, SC-12)

Table 4.2: Channel with Passage Runs

run	$h(x, y, 0)$	forcing type	τ_0	bottom topography
DP-1	1.00	balanced	1.981e-5	no
DP-2	1.00	balanced	3.961e-5	no
DP-3	1.00	balanced	5.942e-5	no
DP-4	1.00	balanced	7.922e-5	no
DP-5	1.00	balanced	1.981e-5	yes
DP-6	1.00	balanced	3.961e-5	yes
DP-7	1.00	balanced	5.942e-5	yes
DP-8	1.00	balanced	7.922e-5	yes

4.5   Channel with Passage

The runs that were performed in the channel with passage geometry are summarized in Table 4.2. In this table, 'topography' indicates a value of μ_B defined by (3.22), while 'no topography' indicates $\mu_B = 0$. 'Balanced' and 'unbalanced' forcing types are as in Table 4.1.

4.5.1   DP-1 – DP-4

In simulations DP-1 – DP-4, we consider simulations in the passage domain as described in Section 3.4.3, with no bottom topography. The presence of the land barriers in this geometry restricts the circumpolar flow to the gap between the land barriers. Figure 4.29 shows the time-averaged streamlines for both layers in the presence of a weak Ekman forcing ($\tau_0 = 1.981$e-5) while Figure 4.30 shows the time-averaged streamlines for a strong Ekman forcing ($\tau_0 = 7.922$e-5). In both cases, part of the flow enters into a recirculating gyre in the northern part of the domain, while the remaining flow passes through the passage, with a northward deflection after exiting the passage. In the lower layer, flow is similar to the upper-layer flow in both wind cases, admitting a combination of recirculating and circumpolar flow. Whereas the upper-layer velocity is not affected greatly by varying the Ekman pumping strength, the lower-layer velocity increases almost linearly with the Ekman pumping strength, as shown in Figure 4.31. As in simulations SC-13 – SC-16, mean meridional flow is possible. However, a similar cancelling of meridional flows is seen after zonally averaging, as in simulations SC-13 – SC-16, leading to a very small mean meridional
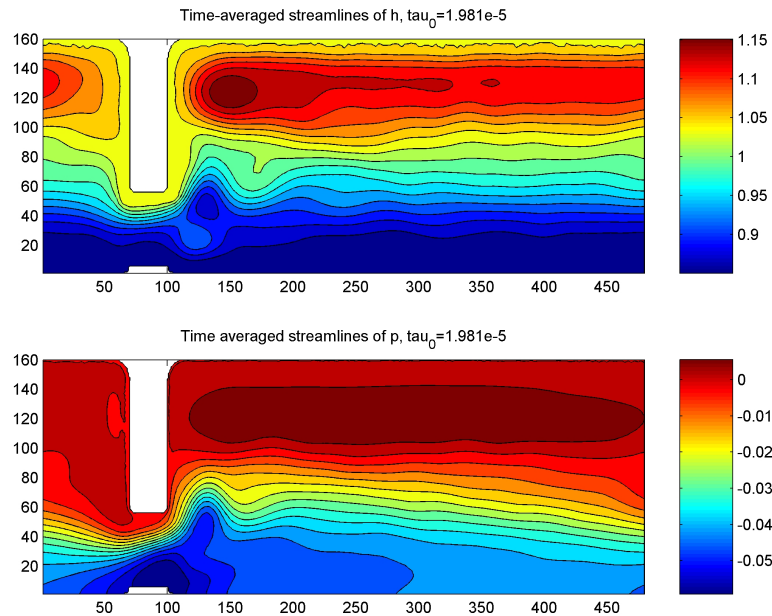
Figure 4.29: Time-averaged streamlines in the upper and lower layer. (DP-1)

eddy height flux (see Figure 4.32).

The balance in the upper layer for DP-4 is shown in Figure 4.33. Whereas the simple channel has a clear leading-order balance between eddy flux and Ekman forcing, the Ekman forcing in the upper layer for DP-4 is balanced by a combination of eddy flux and upper-layer friction. Friction becomes important in this balance as a result of the highly viscous region along the land barriers. This viscous boundary region allows a meridional transport via a mean flux along the peninsula [12]. The contribution of friction to the upper-layer momentum balance can be likened to the effect of a horizontal friction (i.e., the effect of the current rubbing against continents). See [20] for a detailed explanation of this effect.

The balance in the lower layer for DP-4 is shown in Figure 4.34. A clear leading-order balance is established between the potential vorticity flux and linear friction.

4.5.2   DP-5 – DP-8

We consider the runs DP-5 – DP-8 that are characterized by the passage domain as described in Section 3.4.3, and also include a topographic ridge at the passage
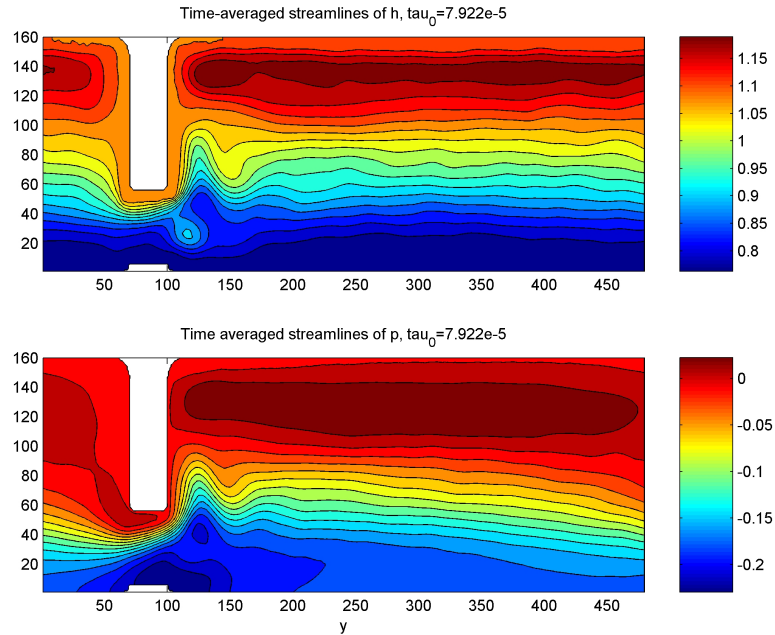
Figure 4.30: Time-averaged streamlines in the upper and lower layer. (DP-4)

as in Figure 3.1.c. Figure 4.35 shows the time-averaged streamlines for both layers in the presence of a weak Ekman forcing (τ_0 = 1.981e-5), while Figure 4.36 shows the time-averaged streamlines for a strong Ekman forcing (τ_0 = 7.922e-5). In both cases, the upper-layer velocity is deflected northward as the flow moves through the passage. As the wind increases, this deflection becomes somewhat more pronounced. In both cases, the presence of the land barriers creates closed contours indicating a recirculation of flow that reduces the overall zonal transport. In the lower layer, the presence of the topographic ridge effectively shuts off lower-layer transport, blocking all circumpolar contours and instead creating two recirculating gyres as found in [33].

Figure 4.37 shows the zonal-mean geostrophic velocity in each layer for 4 Ekman pumping strengths. As in simulations DP-1 – DP-4, there is a weak dependence on τ_0 in the upper layer velocity, while increasing τ_0 almost linearly increases the strength of the gyre flow in the lower layer.

Upper- and lower-layer balances are shown in Figures 4.38 and 4.39 for DP-8, where the potential vorticity flux has been decomposed as in Section 4.4.4 and 4.5.1. The upper-layer balance is very similar to the DP-4 simulation, exhibiting friction
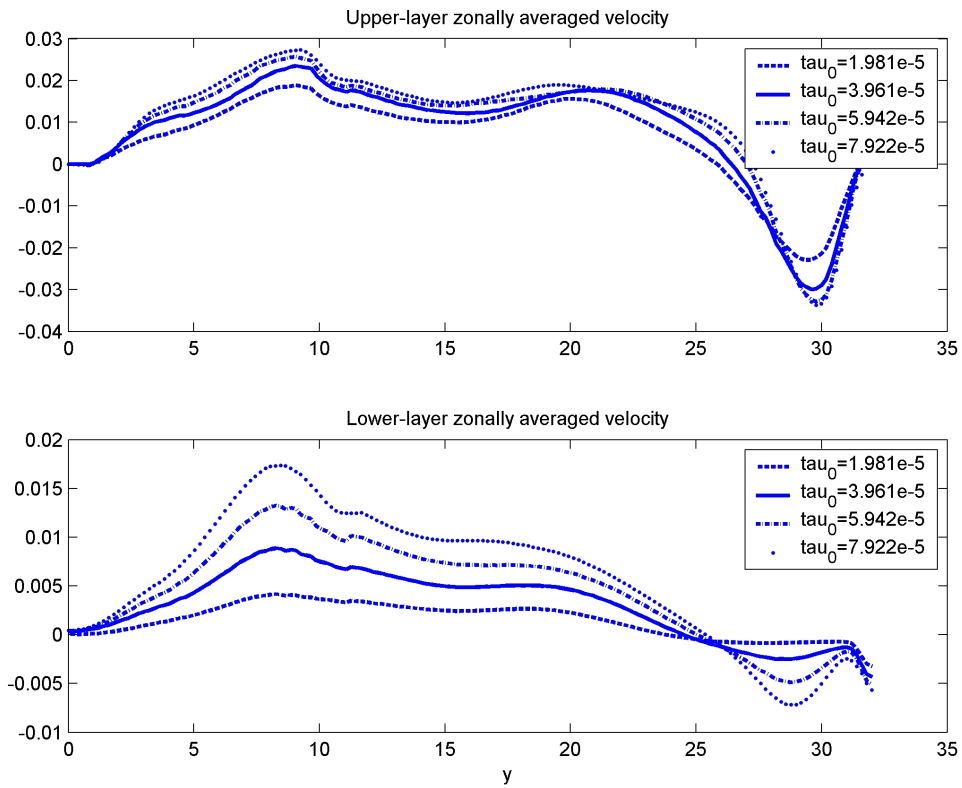
Figure 4.31: Upper- and lower-layer time-averaged zonally averaged velocity for τ_0 =1.981e-5 – 7.922e-5. There is a stronger dependence on τ_0 for the lower-layer velocity as compared to the upper-layer velocity. (DP-1 – DP-4)
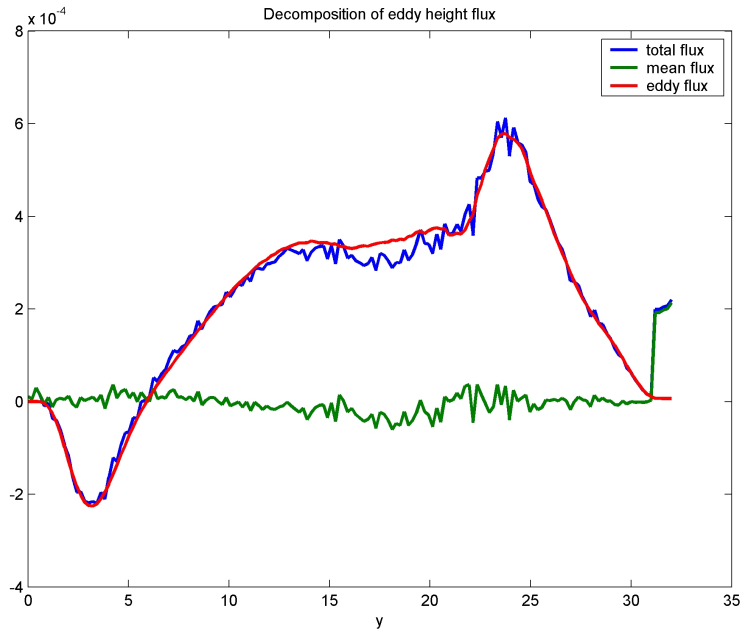
Figure 4.32: Decomposition of $\overline{hp_x}$ into mean $(\overline{h}\,\overline{p_x})$ and eddy $(\overline{h'p'_x})$ components. (DP-4)

Figure 4.33: Nondimensional zonal-mean upper-layer balance (4.22). (DP-4)
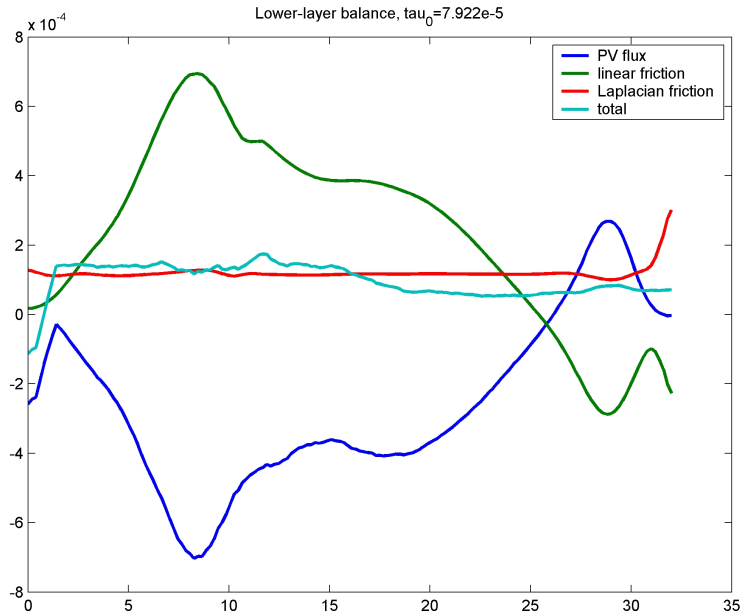
Figure 4.34: Nondimensional zonal-mean lower-layer balance (4.27). (DP-4)

and potential vorticity flux balancing the Ekman forcing. The lower-layer balance is less clear. Although noisy, there is a balance established through the passage, and another balance established in the meridional region of the land barrier, although there is a slight upward drift in y. By decomposing potential vorticity flux, we can deduce that the bottom formstress is predictably most prevalent in the gap between the land barriers, which is the only region that the flow interacts with the topography.

4.6   Transport

There is some debate concerning what determines the circumpolar transport of the ACC (see [33] for a review of theories). A number of numerical studies have been performed, including [33], in which the authors conclude that the zonal transport is determined by a 'complex interplay between wind forcing, eddy fluxes, and topographic effects.' In this section, we study the relationship between transport and Ekman pumping magnitude for the various experiments that were conducted with our implementation of the FG model. Because we wish to compare our numerical results with those of other models, we dimensionalize our quantities in this section

Figure 4.35: Time-averaged streamlines in the upper and lower layer. (DP-5)


Figure 4.36: Time-averaged streamlines in the upper and lower layer. (DP-8)

Figure 4.37: Upper- and lower-layer time-averaged zonally averaged velocity for $\tau_0 =$1.981e-5 – 7.922e-5. (DP-5 – DP-8)
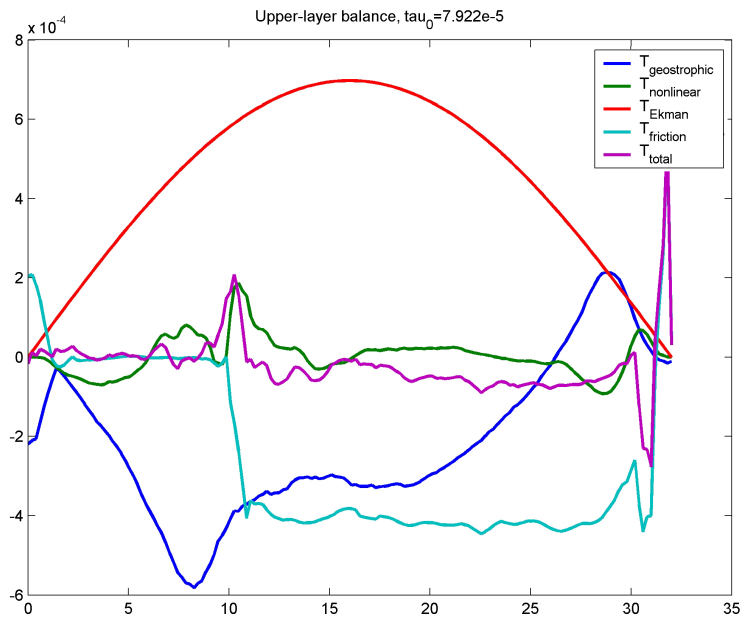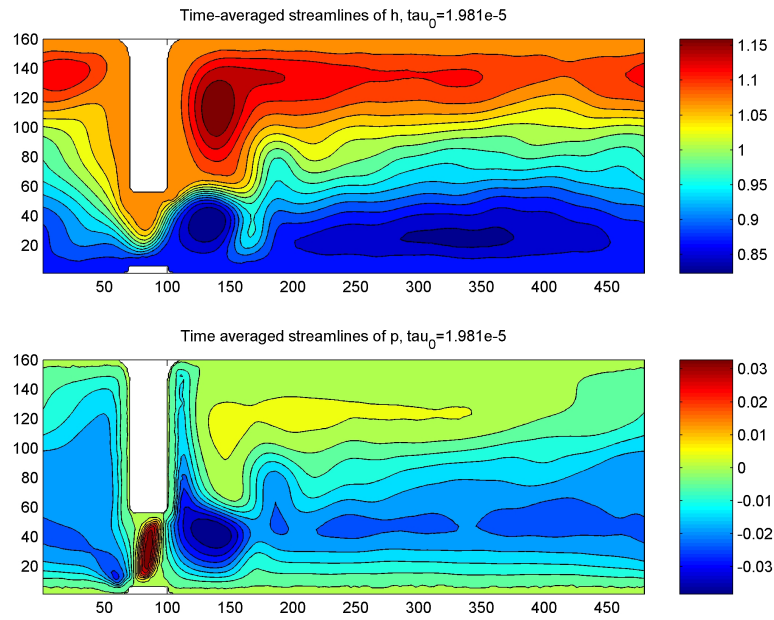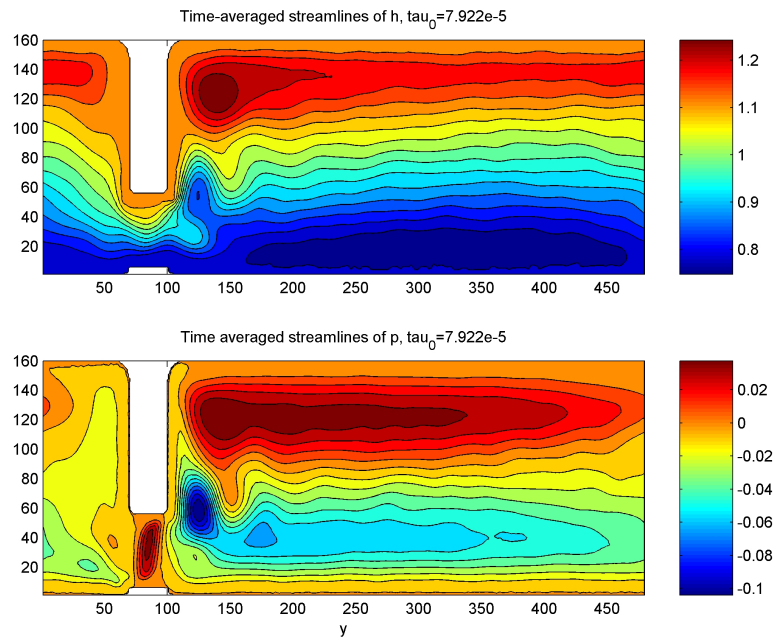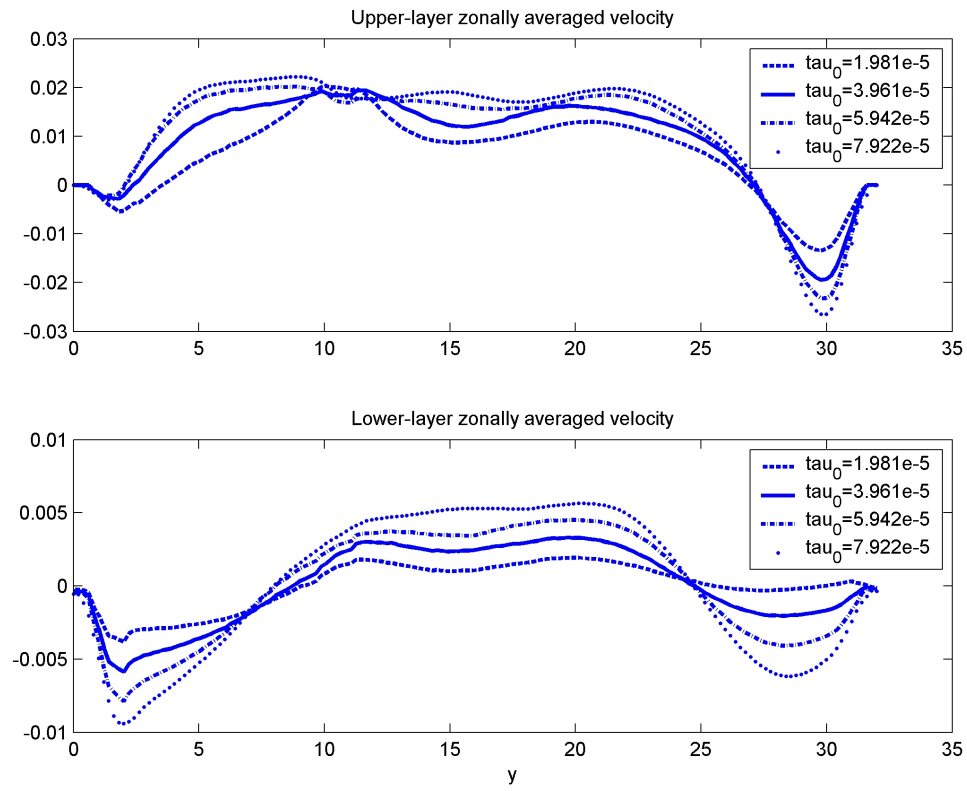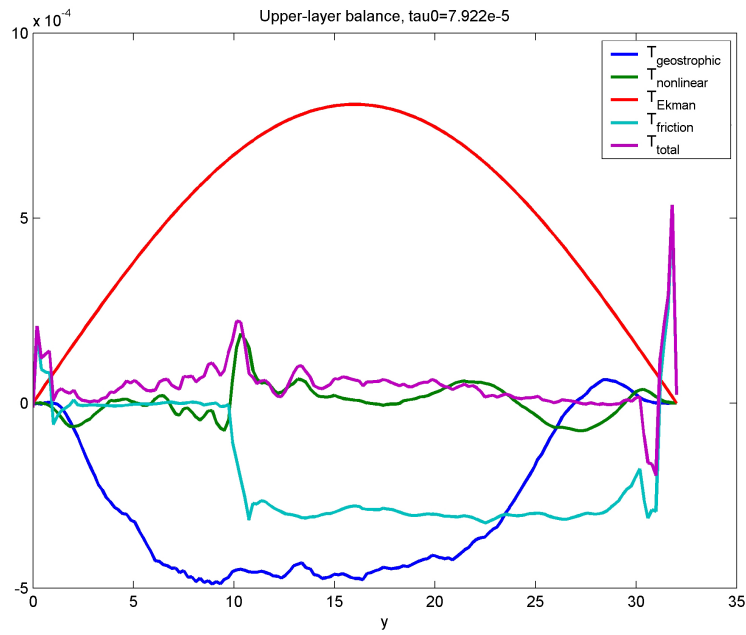
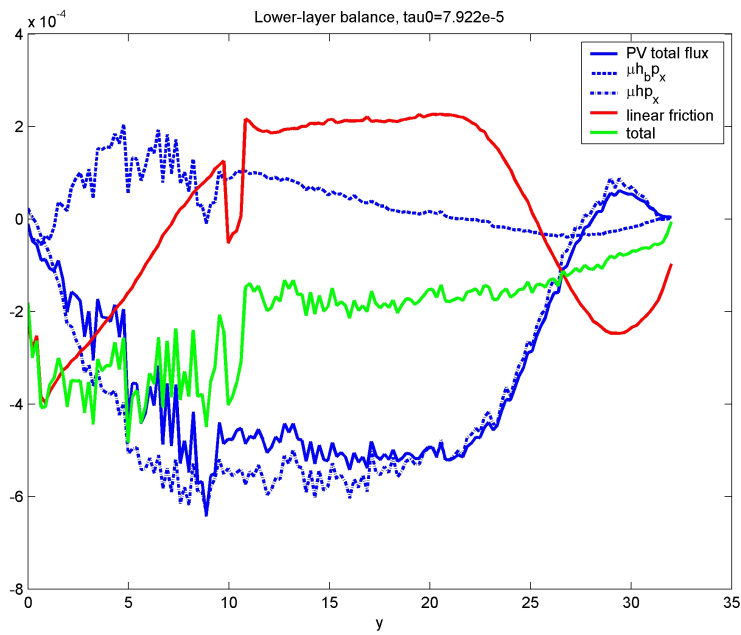Figure 4.38: Nondimensional zonal-mean upper-layer balance (4.22). (DP-8)

Figure 4.39: Nondimensional zonal-mean lower-layer balance (4.27). (DP-8)

by multiplying variables by their scale factors from Section 2.2.

We first define a number of terms to distinguish components of zonal transport.

A (dimensional) *barotropic transport* is defined by

$$T_{barotropic} = \int_0^D L_H H U_2 \overline{u_{2,H}^{(0)}} dy, \tag{4.33}$$

where $u_{2,H}^{(0)}$ is the x-component of $\mathbf{u}_{2,H}^{(0)}$, U_2 is the lower-layer velocity scale factor, L_H is the dimensional domain width, and H is the total depth. The term 'barotropic' refers to a flow in which motions are uniform over the depth of the ocean.

A (dimensional) *baroclinic transport* is defined by

$$T_{baroclinic} = \int_0^D L_H H_1 h \left(U_1 \overline{u_{1,H}^{(0)}} - U_2 \overline{u_{2,H}^{(0)}} \right) dy, \tag{4.34}$$

where H_1 is the upper-layer depth scale factor, U_1 the characteristic upper-layer velocity scale factor, $u_{1,H}^{(0)}$ is the x-component of $\mathbf{u}_{1,H}^{(0)}$, and all other quantities are as in (4.33). The term 'baroclinic' refers to the depth-dependent flows as a result of sloped isopycnals. There are alternative definitions for baroclinic and barotropic transport for a two-layer model (see, e.g., [11]), but we choose the definitions used in [33]. Units of transport are m^3s^{-1}; we express quantities in Sverdrups (Sv), where 1 Sv $= 10^6$ m^3s^{-1}.

We also define *upper-layer transport* as

$$T_{upper-layer} = \int_0^D L_H H_1 h_1 U_1 \overline{u_{1,H}^{(0)}} dy,$$

and *lower-layer transport* as

$$T_{lower-layer} = \int_0^D L_H (H - H_1 h_1) U_2 \overline{u_{2,H}^{(0)}} dy,$$

where all quantities are as in (4.33) and (4.34).

Figure 4.40 shows upper-layer transport for a range of Ekman pumping values. The graphs include data for the simple channel, the simple channel with topography, the channel with passage, and the passage and topography simulations. As we expect, upper-layer transport is largest in the simple channel, as there is no land or topographic effects to reduce the overall zonal flow via recirculating gyre flows and horizontal frictional dissipation. There is little difference in upper-layer transport for

Table 4.3: Scaling Exponents for Baroclinic Transport vs. τ_0

simulation	exponent
simple channel	0.21
channel with passage	0.31
channel with passage and topography	0.39
simple channel with topography	1.06

the cases of the passage and the passage with topography. We can reasonably conclude that in this case the land barriers are the primary determinant in the upper-layer transport, as the northward deflection seen in the simple channel with topography is blocked by the land barriers and thus there is little effect by the topographic ridge in the presence of land barriers.

The lower-layer transport is shown in Figure 4.41 for a range of τ_0 values for the 4 cases as listed above. The transport increases linearly with τ_0 for the two cases (the simple channel and the passage) that allow a lower-layer circumpolar flow. In the two cases with the topographic ridge (passage with topography, and simple channel with topography) the lower-layer circumpolar flow is blocked by the ridge, and circumpolar flow is 0. As in the upper layer, the total lower-layer transport is reduced by the presence of land barriers in the passage case, due to the recirculating gyre flows that occur as a result of the land barriers, and that do not contribute to circumpolar transport. Lower-layer transport is essentially the same as barotropic transport, except for a different scale factor.

Figure 4.42 shows baroclinic transport. Because this transport is a measure of the transport driven by the density gradient, it provides a good indicator of transport for our model. Johnson and Bryden [10] deduced that the baroclinic transport should scale with the square root of wind stress magnitude, whereas Visbeck et. al. [34] predict that the baroclinic transport scales with the cube root of wind stress. Table 4.3 shows the scaling exponent with wind-stress for baroclinic transport for each case. Values were obtained by the slope of the line of best fit through log-log data of transport vs τ_0.

In our simple channel runs, we found that

$$T_{baroclinic} \propto \tau_0^{0.21},$$

Figure 4.40: Upper-layer zonal transport vs. τ_0 for the simple channel (SC-1 – SC-4), the simple channel with topography (SC-13 – SC-16), the channel with passage (DP-1 – DP–4), and the channel with passage and topography (DP-5 – DP-8).

Figure 4.41: Lower-layer zonal transport vs. τ_0 for the simple channel (SC-1 – SC-4), the simple channel with topography (SC-13 – SC-16), the channel with passage (DP-1 – DP–4), and the channel with passage and topography (DP-5 – DP-8).
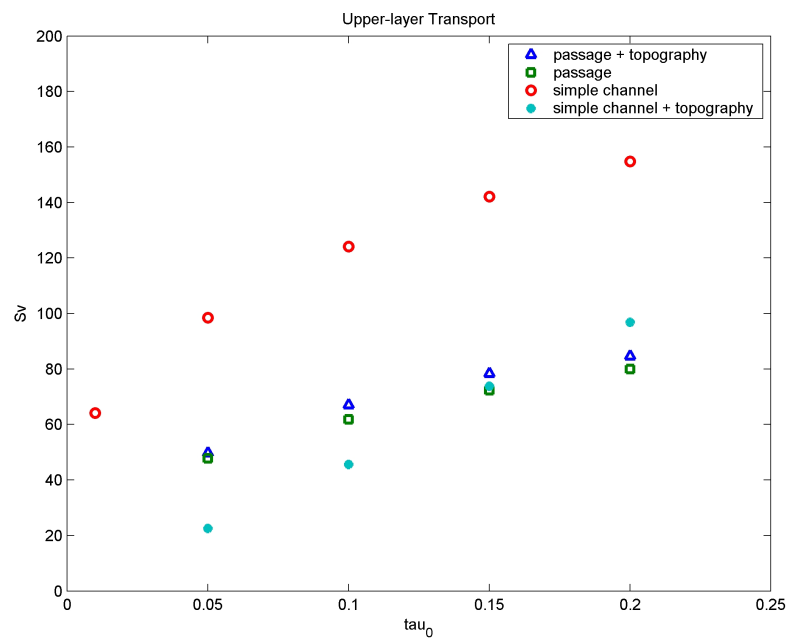
Figure 4.42: Baroclinic zonal transport vs. τ_0 for the simple channel (SC-1 – SC-4), the simple channel with topography (SC-13 – SC-16), the channel with passage (DP-1 – DP–4), and the channel with passage and topography (DP-5 – DP-8).
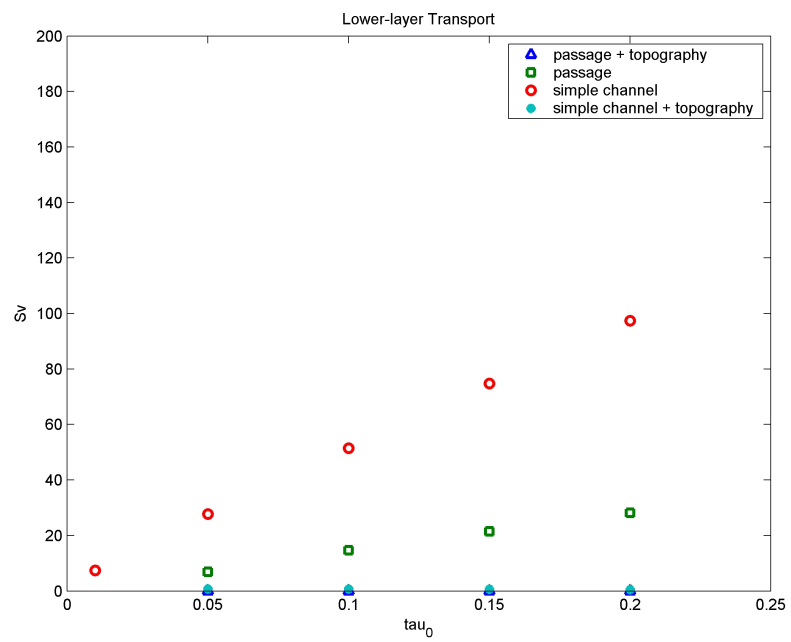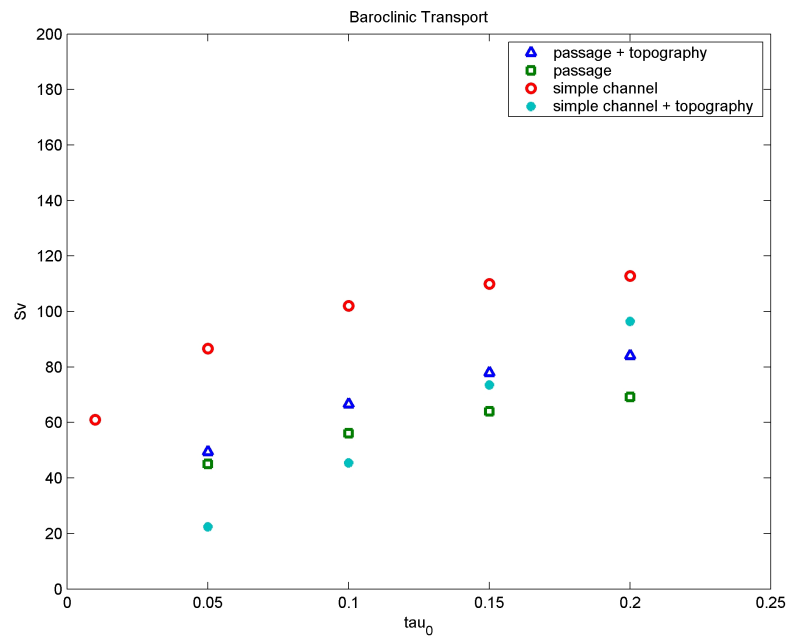
whereas in [33], baroclinic transport was proportional to approximately $\tau_0^{1/2}$. For the channel with passage and the passage and topography simulations, the scaling exponent is very close to that predicted by [34]. This contrasts with [33], who find that baroclinic transport in these cases is essentially independent of τ_0. In the case of the topographic ridge in the simple channel, there is an essentially linear growth in baroclinic transport as τ_0 is increased. This is in sharp contrast to [33], where it is reported that baroclinic transport increases approximately with $\tau_0^{1/13}$. In our simulations, we found the presence of recirculating gyre flow on both sides of the topographic ridge in the upper layer. As wind increases, this gyre flow reduces, increasing the overall transport, contributing to the large exponent.

To investigate the role of bottom Ekman friction, r_2 was reduced by a factor of 10 in both the simple channel (SC-2) and the passage and topography case (DP-6). In the simple channel, the reduction in r_2 by a factor of 10 increased barotropic transport by nearly a factor of 10, from 73.5 Sv to 656.1 Sv. A similar scaling was seen in [33]. The baroclinic transport decreased from 101.98 Sv to 14.96 Sv with the reduction of r_2 by a factor of 10 because the upper-layer transport scaled more weakly (124.09 Sv to 212.41 Sv) than the lower-layer transport (51.43 Sv to 458.67 Sv). In the case of the passage and topography, a much different response to varying bottom friction occurs. Barotropic transport is unchanged at 0 Sv, as lower-layer transport is blocked by the topographic ridge. Upper-layer transport (which is equal to baroclinic transport in the absence of lower-layer transport) increased by only a small amount from 66.9 Sv to 71.21 Sv in the presence of a decrease in r_2 by a factor of 10.

4.7 Resolution Analysis

In a finite element discretization, the resolution is determined by the number of nodes in the domain. In FEMLAB, this is controlled by setting a maximum element size. A valid resolution choice should satisfy a number of requirements. First, the resultant mesh should resolve eddies; that is, it should have a sufficiently dense spacing of nodes such that an eddy is represented by n solution points, where n is chosen based on mean eddy size and some measure of clarity of resolution. Second, refinement of the mesh should not result in finer-scale turbulence, only smoothing of the

observed turbulence. Finally, the mesh should lie in a reasonable region of convergence for quantities associated with the model, with these quantities depending on the particular use of the model.

Figure 4.43 shows a typical upper layer turbulence field given by $h(x, y, t)$ for three resolutions; a very coarse mesh of 2516 elements, the mesh used for the model runs (e.g., SC-1 – SC-12) containing 12228 elements, and a fine mesh of 60124 elements. Clearly, the coarse mesh does not properly resolve the turbulence field, whereas there is little qualitative difference in the turbulence between our chosen resolution and the high resolution.

Figure 4.44 shows a comparison of some basic quantities associated with the model under three resolutions. The coarse 2516-element mesh yields quantities that are certainly on the same order as higher-resolution quantities, although the error is large enough to warrant a finer resolution. The resolution chosen for our runs (e.g., SC-1 – SC-12) is 12288 elements, so as to correspond to the 192×64 finite difference mesh used in [33]. The relatively small difference in the 12288-element and 60124-element cases implies that the resolution chosen for our model runs is valid. In Figure 4.44.a, the upper-layer depth has a somewhat sharper gradient for the coarse resolution. There is little change in the 12288-element and 60124-element cases. In Figure 4.44.b, the zonal-mean profile of p shows a considerable difference in coarse resolution, whereas the difference is negligible in the 12288-element and 60124-element cases. In Figure 4.44.c, the upper-layer zonal-mean velocity structure is not well-resolved with the coarse resolution. The structure and magnitude are similar in the 12288-element and 60124-element cases, although mesh refinement from 12288 to 60124 seems to slightly translate the zonal jets. In Figure 4.44.d, the lower-layer zonal-mean velocity is noticeably weaker with a coarse resolution, whereas the profile is similar in the 12288-element and 60124-element cases, although again there is a slight translation of zonal jets under mesh refinement from 12288 to 60124. We note that varying the mesh invariably leads to small differences in the final state of the model.

Figure 4.45 shows a comparison of upper-layer and lower-layer transport for a series of resolutions. For coarse resolutions, lower-layer transport is widely variant;
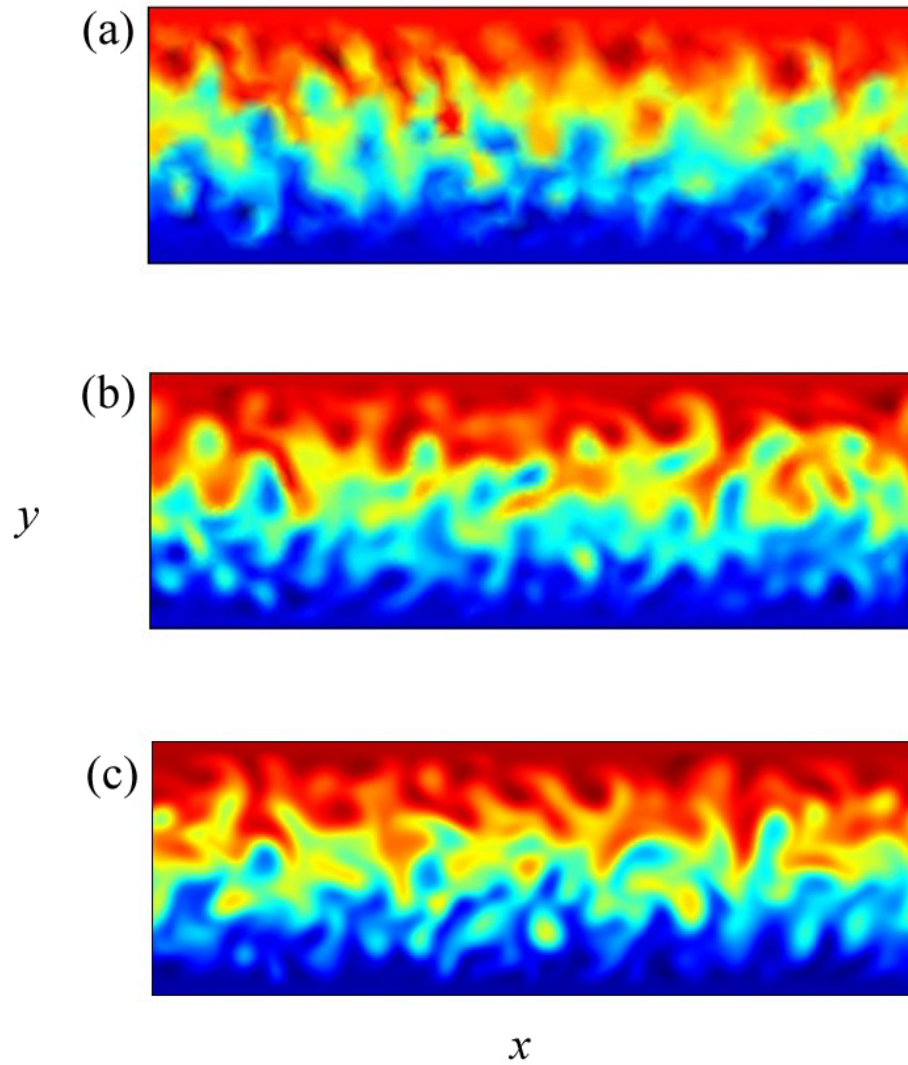
Figure 4.43: A mesh comparison for solutions with meshes containing [a] 2516 elements, [b] 12288 elements, and [c] 60124 elements. Each picture shows upper-layer depth, $h(x, y, t)$, at $t = 30000$. (SC-4)
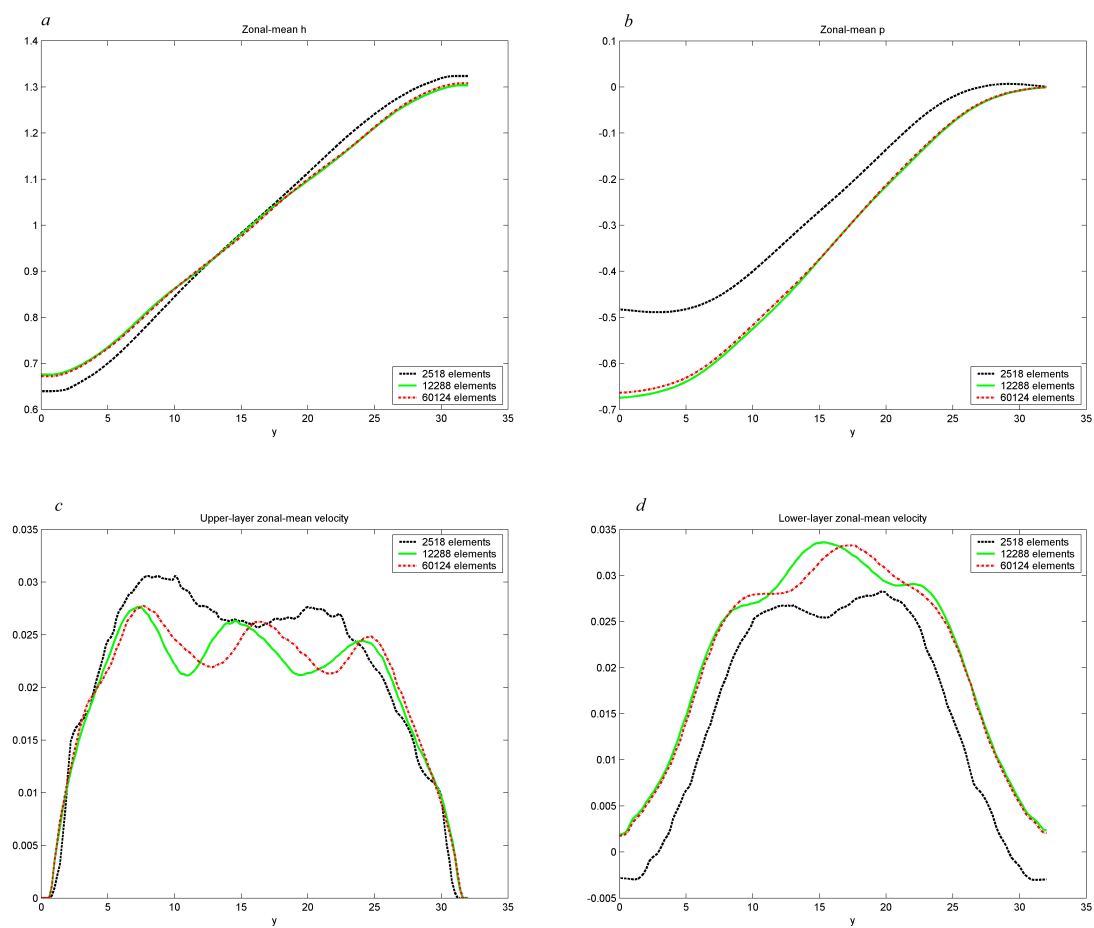
Figure 4.44: A comparison of quantities for 2516, 12288, and 60124 elements. (SC-4)
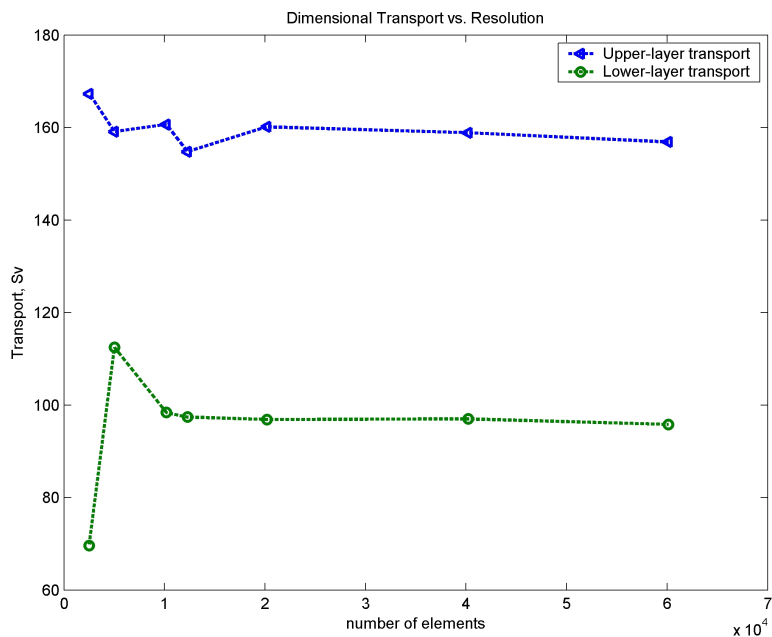
Figure 4.45: A comparison of upper-layer and lower-layer transports for a series of mesh resolutions. (SC-4)

at the 10174-element resolution, a clear convergence prevails. In the upper-layer, there is little change in transport after the 20128-element resolution, although the overall difference in upper-layer transport for all meshes is small.

4.8 Time-stepping

FEMLAB has a built-in time-stepping algorithm, FLDASPK for differential-algebraic equations (DAE) up to index-2. This is a modification of DASPK [5] for the FEMLAB environment. DASPK is itself an extension of DASSL [27]. DASPK expanded the linear system solution options to include Krylov iterative methods, whereas DASSL was limited to direct methods. FLDASPK is a variable-order, variable-step backward differentiation formula (BDF) method. The BDF class of methods is a linear multi-step method, which we describe here applied to a scalar ODE for notational ease.

Consider the first-order scalar ODE

$$y' = f(t, y).$$

A BDF method is derived by differentiating the polynomial that interpolates past values of y, and setting the derivative at t_n to $f(t_n, y_n)$ [3]. The result is a *k-step BDF* of order $p = k$, defined by

$$\sum_{i=1}^{k} \frac{1}{i} \nabla^i y_n = h f(t_n, y_n),$$

where h is the step size, and ∇ is the backward difference operator given by

$$\begin{aligned} \nabla^0 f_l &= f_l, \\ \nabla^i f_l &= \nabla^{i-1} f_l - \nabla^i f_{l-1}. \end{aligned}$$

We note that BDF methods are stable only for $k < 7$; $k = 6$ is also typically avoided because of a lack of robustness. BDF methods are implicit and require the solution of a nonlinear system at each time-step. FLDASPK uses a modified Newton iteration to solve the nonlinear algebraic equations at each time step. This is a variant of Newton's method, defined by

$$y_n = y_{n-1} - c \left(\alpha \frac{\partial F}{\partial y'} + \frac{\partial F}{\partial y} \right)^{-1} G\left(t, y_{n-1}, \alpha y_{n-1} + \beta \right),$$

where $F(t, y, \alpha y + \beta)$ is the nonlinear equation to be solved at each time step, α is a constant that depends on step size, β is a vector that depends on the solution at past times, and G is a function of known values [2]. In a system of equations, the iteration matrix, $\alpha \partial \mathbf{F} / \partial \mathbf{y}' + \partial \mathbf{F} / \partial \mathbf{y}$ is rewritten via an LU decomposition and then solved. FLDASPK offers a number of solvers at this stage; we choose a direct method called UMFPACK [7] which we find to be the most efficient of the available methods. UMFPACK is an un-symmetric multi-frontal method for direct LU factorization. This software is able to take advantage of the sparse matrices that prevail in the finite element method. Despite being somewhat more memory intensive than iterative methods (e.g., GMRES [30]), the high efficiency of the method coupled with its inherent stability as a direct method makes it the optimal choice. In the finite element discretization, a test function at a node is a function of only its neighboring nodes; hence the finite element discretization results in a sparse matrix to be solved [1]. As we increase the resolution, the number of nodes, and thus the number of test functions, increases. However, the number of non-zero matrix entries introduced with each new

equation is constant, depending only on the order of the element. Therefore, using a highly efficient solver like UMFPACK allows for an almost-linear scaling in the time requirement as resolution is increased.

In addition to choosing the linear solver, FEMLAB allows the user a number of time-stepping options. The user may enter a list of times for which the solution is stored. Then, the user chooses between a free, intermediate, or strict time step. With a strict step, the solver is forced to take a time step at each user-defined time, and may take time steps in between as needed. With an intermediate step, the solver is forced to take at least one step in each interval between the user-defined times. With a free step, there is no user restriction on the timestepping; the time-stepping is determined by local error restrictions in the solver. The user can also enter a maximum time-step value as an alternative to modifying output times via the strict setting. DASPK starts with an initial time step (which the user can set). Typically the time step is successively increased (but at most doubled each step) until a local error calculation exceeds the user-defined tolerance [2]. In our FEMLAB model, before the onset of turbulence the solution is very simple and as a result, the successive time-step increases resulted in very large steps ($O(1000$ units$)$). This large step is unable to properly resolve the onset of turbulence. Figure 4.46 shows a comparison of some exact and approximate model invariants under a free time-step setting and with a maximum time-step of 5 time units. The free time-step setting results in a marked delay of the onset of turbulence. When the solution does become turbulent, there is a jump in upper-layer mass causing the failure of mass conservation, as well as unphysical 'spikes' in lower-layer momentum and kinetic energy. These spikes occur as a result of noisy data that create large spatial derivatives of model variables. Using a maximum time-step setting prevents the spikes and the mass jump, while having little effect on the overall time, as the typical turbulent time step is less than 5 units. As is shown in Figure 4.47, there is no advantage in greatly restricting the time-step, whereas there is a clear disadvantage in solution time as a result of the added unnecessary time steps. Interestingly, from Figure 4.46 we note that the energy and momentum quantities from the free time-step setting approximately converge through time to the restricted time-step setting, whereas the upper-layer mass is conserved
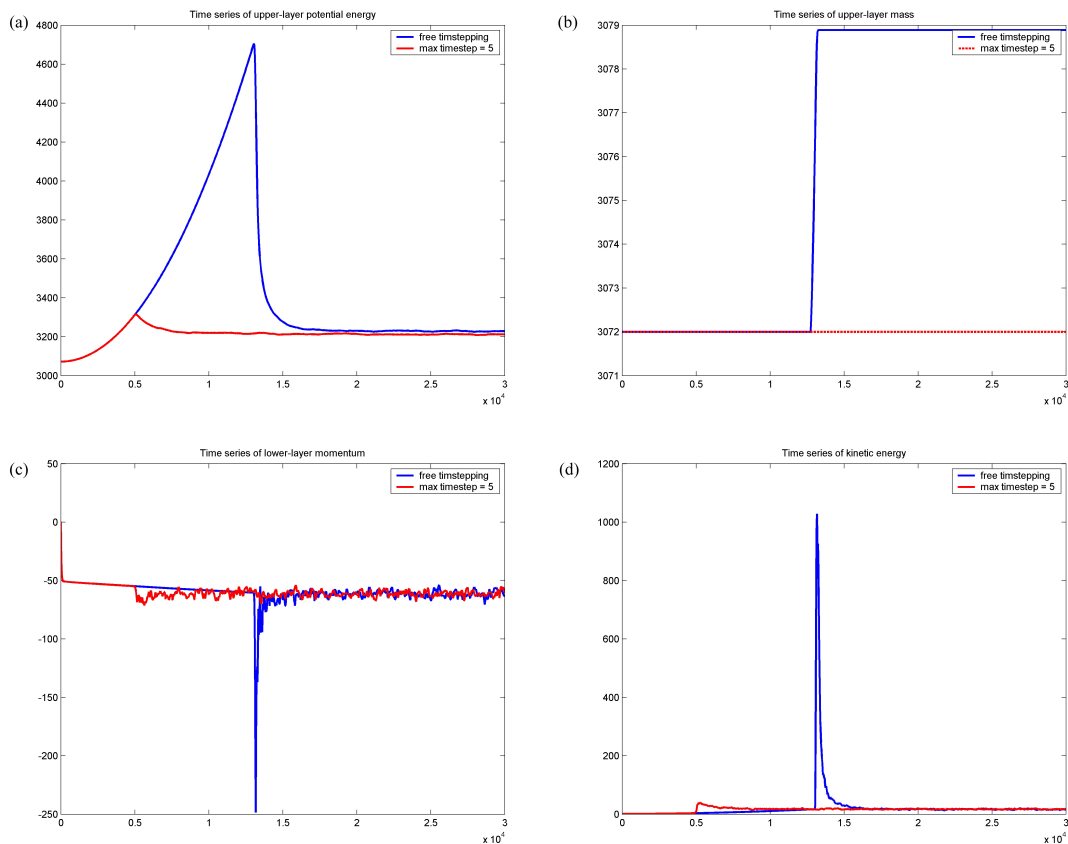
Figure 4.46: Exact and approximate model invariants compared against a free time step and a time step restricted by a maximum of 5 time units. [a] Potential energy, [b] mass, [c] lower-layer momentum, [d] kinetic energy. (SC-4)

following the jump at the onset of turbulence.

As mentioned earlier in this section, the computational time required to solve the finite-element implementation of the FG model can ideally scale almost linearly with the number of nodes in the spatial discretization. In Table 4.4, we show the performance of our model for the test case SC-4 run to $t = 30000$, using a maximum time step of 5 time units. We also show performances for two shallow-water equation models, HIM [9] and MITgcm [23], and the finite-difference implementation of the FG model. Computational times for HIM, MITgcm and the finite-difference FG model were provided in [12] and were run on a single AMD64 Opteron 250 processor. The finite-element FG model was run on a combination of Intel Xeon 3.06 Ghz and Opteron 250 processors. We note that the MITgcm is a six-layer model, whereas the
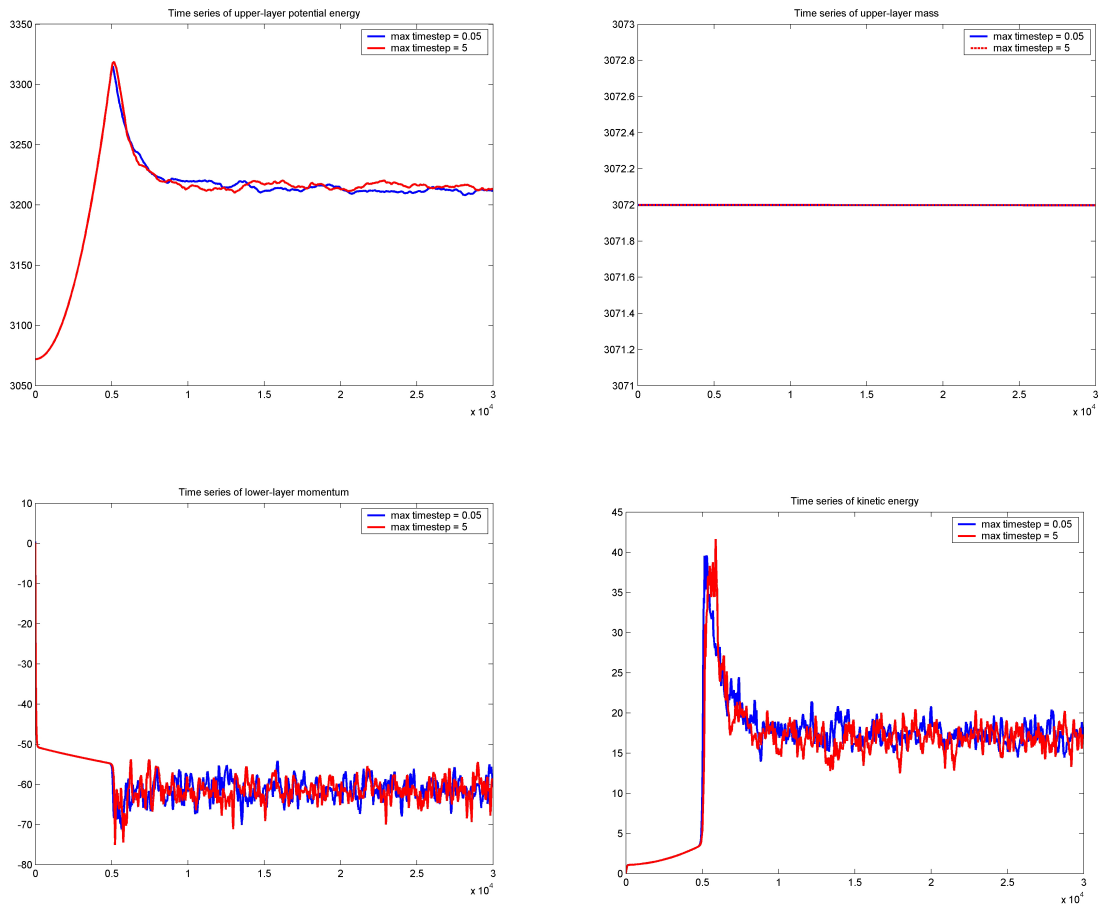
Figure 4.47: Exact and approximate model invariants compared against maximum time-step settings of 0.05 and 5 time units. [a] Potential energy, [b] mass, [c] lower-layer momentum, [d] kinetic energy. (SC-4)

Table 4.4: Performance of ocean models for SC-4

model	resolution	computational time
finite element FG model		
	2516 nodes	4140.48 s = 1.15 hrs
	5016 nodes	9143.76 s = 2.54 hrs
	10174 nodes	20990.342 s = 5.83 hrs
	20228 nodes	45576.33 s = 12.66 hrs
	40220 nodes	100543.13 s = 27.92 hrs
	60124 nodes	213812.45 s = 59.39 hrs
finite diff. FG model		
	$192 \times 64 = 12288$ pts	2.2 hrs
	$384 \times 128 = 49152$ pts	52.9 hrs
	$768 \times 256 = 196608$ pts	approx. 1700 hrs = 71 days
HIM		
	$192 \times 64 = 12288$ pts	19.9 hrs
	$384 \times 128 = 49152$ pts	201 hrs = 8.37 days
	$768 \times 256 = 196608$ pts	1620 hrs = 67.5 days
MITgcm		
	$192 \times 64 = 12288$ pts	36 hrs

others are two-layer models.

Although the finite difference implementation of the FG model is roughly twice as fast as our finite element model for a 192×64 resolution, performance drops off quickly, and after doubling the resolution (i.e., increasing the number of nodes by a factor of 4), the finite element implementation outperforms the finite difference implementation, almost by a factor of 2. This exponential growth in computational time is due to the explicit nature of the timestepping in the finite difference code. As resolution is increased, a stability restriction requires a corresponding decrease in the time step, increasing the computational requirement. However, the finite element implementation is implicit, and thus no spatially dependent stability restriction exists for this method. Regardless of resolution, FEMLAB maintains essentially the same time step (from 2516 nodes to 60124 nodes, there was only a 0.3% change in the time step size). The HIM model also exhibits a reduction in time step with increased resolution (proportional to the change in Δx). The MITgcm data were included to emphasize the relative computational time scales for our reduced model versus the more complex primitive-equation MITgcm model.

Chapter 5

Conclusion

In this thesis, a two-layer frontal geostrophic model for wind-driven flow was simulated with the finite element method via the software package FEMLAB. The use of the finite element method facilitated the extension of the model to irregular domains. This implementation is most notably efficient for higher resolutions, due to the favorable, almost-linear scaling of computation time with resolution. The implementation is also stable, improving on the finite-difference implementation that failed under negative values of $h(x, y, t)$ or relatively large values of $h(x, y, t)$ (e.g., $h(x, y, t) = 1.5$) [12]. However, the boundary conditions in this implementation were fairly problematic; the decision to use a sponge layer around boundaries very likely strongly affects model results and makes comparisons with similar models more difficult. As the geometry is extended to irregular domains, these boundary issues become more important, and the specification of the sponge layer becomes difficult. The natural extension of this model into realistic domains (see Figure 5.1) is possible, although the specification of sponge layers becomes difficult in FEMLAB. Our efforts to extend the model to realistic domains was limited to using Boundary Method I, which loses the fundamental conservation of mass property of the model. This implementation was designed for studying an idealization of the Antarctic Circumpolar Current.

This implementation does develop a verifiable quasi-steady state in a host of domain and parameter regimes, allowing for an investigation into the meridional balance suggested by the model results. In the simple channel, the model results support the theory of momentum balance wherein momentum imparted by wind stress at the surface is transferred from the upper layer to the lower layer via interfacial form stress, and then dissipated in the lower layer by bottom friction. In the presence of bottom topography, this lower-layer dissipation is achieved jointly by bottom friction and bottom form stress, and as the lower-layer friction is reduced, primarily by bottom form
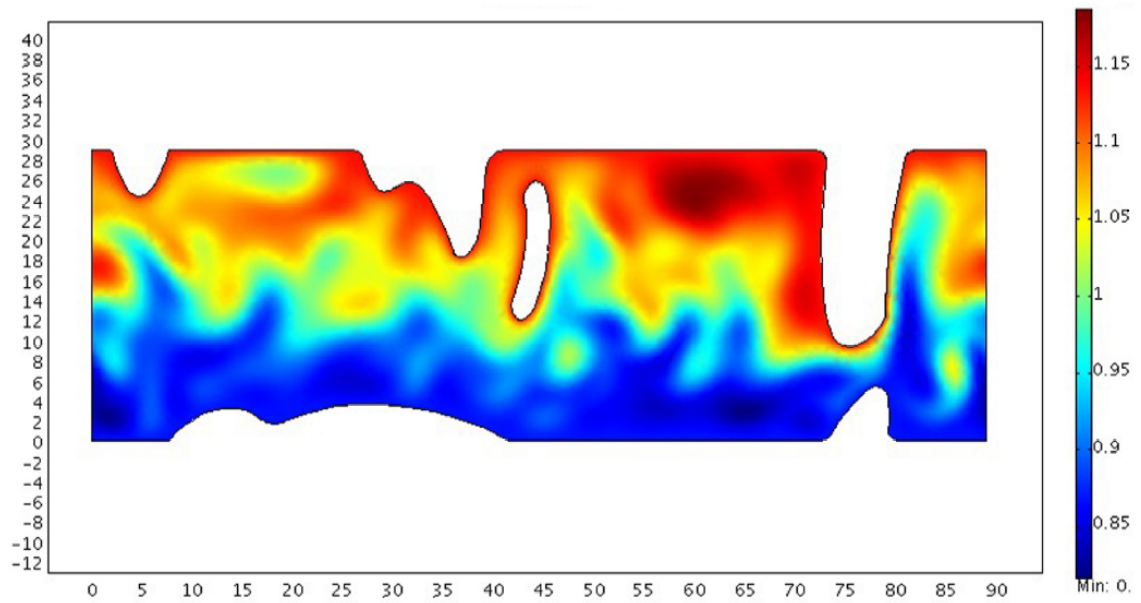
Figure 5.1: Solution of model equations using FEMLAB in a more realistic domain, using idealized land masses in the Southern Ocean. Valid boundary conditions are the main concern in this extension.

stress. The implementation allows for outcroppings, both transient (disappearing at quasi-steady state) and permanent (prevailing at quasi-steady state). The onset of outcropping establishes a larger gradient in both $h(x, y, t)$ and $p(x, y, t)$ at quasi-steady state, which implies stronger upper- and lower-layer leading-order velocities. We also found that in the presence of outcropping (both transient and permanent), the mass of the system at quasi-steady state is independent of initial upper-layer depth; instead it is determined by the balance struck between winds and frictional dissipation.

When the geometry is altered to include land barriers representative of the Drake Passage, the highly viscous region around the barriers dissipates momentum in concert with the eddy interfacial form stress transferring momentum to the lower layer. Thus, our choice and implementation of boundary conditions in this geometry have a strong impact on the prevailing momentum balance at quasi-steady state. When a topographic ridge is added to the passage geometry, upper-layer transport is not strongly affected, suggesting that the land barriers essentially determine the upper-layer transport through the passage. The topographic ridge does essentially eliminate lower-layer transport, however.

Baroclinic transport was calculated for the four domain/topography regimes. In the simple channel, our results indicate a relatively weak growth in transport in relation to wind strength. This contrasts with results in [33], although that model uses different boundary conditions, a very low bottom friction, and a slightly different set of model equations. We found the passage domain transport results to agree strongly with [34], both in the presence of a topographic ridge and with no bottom topography. In the case of bottom topography in the simple channel, we found a very strong growth in baroclinic transport with wind strength, in sharp contrast with [33]. These results again are likely due to the viscous boundary region. Low wind strengths create a larger northward deflection of flow, thus increasing dissipation of velocity as more streamlines enter the viscous region. As wind strength increases, there is less northward deflection, and this viscous layer dissipation is reduced.

When bottom friction is reduced by a factor of 10 in the simple channel, barotropic transport increases approximately by a factor of 10. However, in the case of the

passage with topography, barotropic transport remains unchanged (because lower-layer transport is blocked by the ridge), and baroclinic transport changes only slightly with a similar reduction in bottom friction.

The resolution chosen for our simulations sufficiently resolves the turbulence in the solution of $h(x, y, t)$ and $p(x, y, t)$. The resolution also lies in a reasonable region of convergence for the model variables $h(x, y, t)$ and $p(x, y, t)$, and for various quantities associated with the model (velocities, transport). The solution validity was dependent upon time step restriction. With no user-defined restriction (i.e., allowing the time-stepping algorithm determine the time step-size), the onset of turbulence is delayed, the solution is very noisy at the onset of turbulence leading to spikes in energy and momentum quantities, and mass conservation is lost. This effect can be eliminated by limiting the maximum step-size to 5 units, while having little effect on the overall computational requirements.

There are several aspects of this work that remain to be explored. The investigation of other domains is possible with this finite element implementation of the model, provided that boundary conditions can be imposed for arbitrary domain shapes. The solution of the model in a more realistic domain as discussed above provides an example of this possible work, as well as the difficulties that must be overcome. In addition, the numerical integration of the model equations could be investigated with a variety of different integrators. Structure-preserving integrators (e.g., symplectic methods) hold interest for the ability to conserve certain model invariants. Also, using this implementation, a more detailed exploration of parameters (e.g., bottom topography, sponge layer properties, friction) may yield more information about the dynamical balance that occurs in the ACC.

Bibliography

[1] Comsol AB, *Femlab 3.1 User's Guide*, 2004.

[2] S. Li amd L. R. Petzold, *Design of New DASPK for Sensitivity Analysis*, software documentation, 1999.

[3] U. M. Ascher and L. R. Petzold, *Computer methods for ordinary differential equations and differential-algebraic equations*, 1998.

[4] D. Borowksi, R. Gerdes, and D. Olbers, *Thermohaline and wind forcing of a circumpolar channel with blocked geostrophic contours*, J. Phys. Oceanogr. **32** (2002), 2520–2540.

[5] P. N. Brown, A. C. Hindmarsh, and L. R. Petzold, *Using Krylov methods in the solution of large-scale differential-algebraic systems*, SIAM J. Sci. Comp. **15** (1994), 1467–1488.

[6] B. Cushman-Roisin, G.G. Sutyrin, and B. Tang, *Two-layer geostrophic dynamics, part I: Governing equations*, J. Phys. Oceanogr. **22** (1992), 117–127.

[7] T. A. Davis and I. S. Duff, *An unsymmetric-pattern multifrontal method for sparse LU factorization*, SIAM J. Matrix Anal. Appl. **18, No. 1** (1997), 140–158.

[8] D. Karl et. al., *The Drake Passage Transect*, http://hahana.soest.hawaii.edu/santacls/viil.html.

[9] R. Hallberg, *HIM: The Hallberg Isopycnal Coordinate Primitive Equation Model*, technical note, 1997.

[10] G. C. Johnson and H Bryden, *On the strength of the circumpolar current*, Deep-Sea Res. **36** (1989), 39–53.

[11] R. H. Karsten, *Nonlinear effects in two-layer frontal-geostrophic models of surface ocean fronts*, Ph.D. thesis, University of Alberta.

[12] _____, *Two-layer frontal geostrophic model description*, private communications, 2004.

[13] R.H. Karsten, H. Jones, and J. Marshall, *The role of eddy transfer in setting the stratification and transport of a circumpolar current*, J. Phys. Oceanogr. **32** (2002), 39–54.

[14] R.H. Karsten and G. Swaters, *A note on the stability theory of buoyancy-driven ocean currents over a sloping bottom*, J. Appl. Math. Physics (ZAMP) **47** (1996), 28–38.

[15] _____, *A unified asymptotic derivation of two-layer, frontal geostrophic models, including planet sphericity and variable topography*, Phys. Fluids **11** (1999), 2583–2597.

[16] _____, *Nonlinear effects in two-layer large-amplitude geostrophic dynamics. Part 2. The weak-beta case*, J. Fluid Mech. **412** (2000), 161–196.

[17] D. Kelley, *Introductory Physical Oceanography*, Lecture Notes, Dalhousie University, Department of Oceanography, 2003.

[18] J. Kim, *A Two-layer Frontal Geostrophic Model of Eddy Fluxes in a Wind-driven Current*, Honors Thesis, Department of Mathematics and Statistics, Acadia University (2002).

[19] P. K. Kundu, *Fluid Mechanics*, Academic Press, San Diego, 1990.

[20] R. Williams L. Jackson and C. Hughes, *The role of bottom pressure torques and friction in basin and channel flows*, submitted to J. Phys. Oceanogr., July 21, 2004.

[21] P. Malanotte-Rizzoli M. Jochum, *Influence of the meridional overturning circulation on tropical-subtropical pathways*, J. Phys. Oceanogr. **31** (2001), 1313–1323.

[22] P. Madl, *The El-Nino Phenomenon*, http://www.sbg.ac.at/ipk/avstudio/pierofun/atmo/elnino.htm, 2000.

[23] J. Marshall, A. Adcroft, C. Hill, L. Perelman, and C. Heisey, *A finite-volume, incompressible Navier Stokes model for studies of the ocean on parallel computers*, J. Geophysical Res. **102 (C3)** (1997), 5753–5766.

[24] B. Murphy and D. Nance, *Earth Science Today*, Thomson Learning, Florence, KY, 1999.

[25] D. Olbers, D. Borowski, C. Voölker, and J. O. Wolff, *The dynamical balance, transport and circulation of the Antarctic Circumpolar Current*, Special Issue of Antarctic Science (2004).

[26] J. Pedlosky, *Geophysical Fluid Dynamics*, Springer-Verlag, New York, 1979.

[27] L. R. Petzold, *A description of DASSL: a differential-algebraic systems solver*, IMACS Trans. on Scientific Computation, R.S. Stepleman Ed. **1** (1982).

[28] M. K. Reszka and G. E. Swaters, *Eddy formation and interaction in a baroclinic frontal geostrophic model*, J. Phys. Oceanogr. **29** (1999), 3025–3042.

[29] _____, *Numerical investigation of baroclinic instability in the Gaspé Current using a frontal geostrophic model*, J. Geophys. Res. **104, No. C11** (1999), 25685–25696.

[30] Y. Saad and M. Schultz, *GMRES: A general minimal residual algorithm for solving nonsymmetric linear systems*, SIAM J. Sci. Statist. Comput. **7** (1986), 856–869.

[31] G. Swaters, *On the baroclinic dynamics, Hamiltonian formulation and general stability characteristics of density-driven surface currents and fronts over a sloping continental shelf*, Phil. Trans. R. Soc. Lond. **345** (1993), 295–325.

[32] C. Tansley and D. Marshall, *On the influence of bottom topography and the Deep Western Boundary Current on Gulf Stream separation*, J. Mar. Res. **58** (2000), 297–325.

[33] _____, *On the dynamics of wind-driven circumpolar currents*, J. Phys. Oceanogr. **31** (2001), 3258–3273.

[34] M. Visbeck, J. Marshall, T. Haine, and M. Spall, *Specification of eddy transfer coefficients in coarse-resolution ocean circulation models*, J. Phys. Oceanogr. **27** (1997), 381–402.

[35] D. J. Webb, B. A. de Cuevas, and A. C. Coward, *The first main run of the OCCAM global ocean model*, Internal Document 34, Southampton Oceanography Centre, 1997.

[36] J.-O. Wolff and E. Maier-Reimer, *The Hamburg Ocean Primitive Equation Model*, DKRZ Technical Report, 1993.

[37] J.-O. Wolff, E. Maier-Reimer, and D. J. Olbers, *Wind-driven flow over topography in a zonal beta-plane channel: A quasigeostrophic model of the Antarctic Circumpolar Current*, J. Phys. Oceanogr. **21** (1991), 236–264.